Design and Analysis of the Medium-β Elliptical Cavities for the European Spallation Source Accelerator

Costanza, Gabriele

2017

Document Version:
Publisher's PDF, also known as Version of record

Link to publication

Citation for published version (APA):
Costanza, G. (2017). *Design and Analysis of the Medium-β Elliptical Cavities for the European Spallation Source Accelerator*. [Doctoral Thesis (compilation), Department of Electrical and Information Technology]. The Department of Electrical and Information Technology.

Total number of authors:
1

LUND UNIVERSITY

PO Box 117
221 00 Lund
+46 46-222 00 00

Design and Analysis of the Medium-β Elliptical Cavities for the European Spallation Source Accelerator

Gabriele Costanza

Doctoral Dissertation
Electromagnetic Theory

Lund University
Lund, Sweden
2017

Doctoral dissertation publicly defended the 3$^{\text{rd}}$ of February, 2017, at 10.15 a.m. in lecture hall E:1406, John Erikssons väg 4, Lund, for the degree of Doctor of Philosophy in Electromagnetic Theory.

Department of Electrical and Information Technology
Lund University
Box 118, SE-221 00 LUND
SWEDEN

This thesis is set in Computer Modern 10pt
with the LaTeX Documentation System

Series of licentiate and doctoral theses
No. 95
ISSN 1654-790X
ISBN 978-91-7753-097-8 (digital)
ISBN 978-91-7753-096-1 (print)

Printed in Sweden by *Tryckeriet i E-huset*, Lund.
2017.

Populärvetenskaplig Sammanfattning

The European Spallation Source (ESS) is the next generation neutron source and it's the fruit of the ongoing effort involving around 60 partner laboratories around the world. The facility is being built in Lund and has the ambition of being a sustainable research facility with net zero release of carbon dioxide. The ESS will produce the most intense neutron beam in the world. The neutrons produced by the machine will be used for a wide range of scientific applications that influence everyday life and they span physics, chemistry, material science, biology, geology and medicine. Neutrons can be used to analyze and engineer, new materials by studying their structure over a wide range of length and time scales.

Curing Diseases. Materials have characterized the development of humanity for ages. Nowadays biologists and chemists are developing molecules that can tackle cancer growth by delivering a specific drug in the right place, helping in curing diseases with minimal impact on the subject. The neutrons produced at the ESS can help investigate how molecules react and function.

Energy Efficiency. Another important application concerns energy conservation. Batteries are ubiquitous nowadays, consider for example laptops and mobile phones. Neutrons can help investigate more complex materials and also monitor the charge and the discharge of batteries in order to improve their efficiency. The same can be said about fuel cells. Fuel cells promise to be able to produce energy in a sustainable way. Research in this sector is devoted to finding better performing and less expensive materials for the membrane used to activate the chemical process happening withing the cell. Neutron scattering in this case can be used to study the dynamics of the hydrogen in the fuel cell as well as its interaction with the electrodes.

How it works. The machine that produces the neutrons is a linear particle accelerator. The linear accelerator is a 300 meter long sequence of devices used to produce, shape and accelerate protons towards a target.

Smashing a small rock. The acceleration process happens in devices called *cavities*, and it can be compared to a surfer on the crest of a wave. Cavities are shaped so as to form and sustain electromagnetic waves that are used for acceleration. The particles gain velocity by staying on the crest of the wave just like a surfer would do on a surfboard. Once the particles leave the linear accelerator, they strike on a rotating helium cooled target that expels neutrons. It is at the target station that the accelerated particles produce the neutrons by a process called spallation. The process is similar to a hammer smashing a small rock. The atoms of the bombarded target break up and expel neutrons that are then channelled towards the experiments and are used for the investigation of matter at an atomic scale.

Superconductivity. Particle acceleration is accomplished by both room-temperature and *superconducting cavities*. Superconducting cavities (see fig. 1) are made of Niobium, a rather rare and expensive metal, and are cooled down to a temperature of -271 degrees Celsius, where they reach a particular state, the superconducting state. When the metal becomes superconducting an electric current can flow through it without resistance, thus no energy is wasted in heat. It is as if an old incandescent light bulb would emit light without warming up, quite an important save of energy. The first part of the accelerator, is dominated by room-temperature cavities, made of copper. These are used to give energy to the beam when extracted from the source and also to shape it, so that it can be accepted by the following stage of the accelerator, dominated by superconducting cavities.

This thesis is dedicated to the design and analysis of superconducting elliptical cavities. Elliptical cavities play a central role in modern particle accelerators due to their high efficiency. After an introduction to the European Spallation Source project, the thesis goes through the design of the medium-β cavity. The RF design of the inner cell and end cell are presented in sequence in paper I . The design is completed by the chapter on the mechanical performances of the cavity (paper II).

Papers III, IV and V are instead dedicated to the analysis of the cavity. The necessary mathematical tools for the analysis are presented in paper III which, after stating fundamental results on hollow cavities, presents a spectral decomposition used in the following papers. In paper IV, a time-domain model for the power dissipation induced by the excited higher-order-modes is presented. Such modes are excited by the particle beam that passes through the cavity and are detrimental to the performances of the accelerator. Paper V presents a time-domain model of the cavity coupled to an externa circuit to a coupler. The model is functional to the design of the cavity control system.

Figure 1: Elliptical Superconducting Cavities.

Preface

This thesis summarizes the research efforts conducted during my doctoral studies aimed at the design of the medium-β elliptical cavity for the European Spallation Source (ESS). The research has been carried out at the Department of Electrical and Information Technology at Lund University. The first part of the thesis is an introduction on accelerators and the European Spallation Source project. The second part of the thesis includes the papers that describe the design and analysis of the medium-β elliptical cavity. Here follows a summary of the structure of the thesis where I summarize the contents of the chapters of the thesis. The summary is followed by the list of included papers with a clarification on my contribution to those works. Additional papers participated in by the author of the thesis, are listed thereafter.

Structure Of the Thesis

The thesis is divided in two parts.

- **Part I**
    - The first part of the thesis is an introduction to accelerators and cavities. The first chapter starts with the description of the ESS accelerator followed by a brief historical survey on accelerators. The second chapters describes some fundamental aspects of cavities and general considerations on cavity design.
- **Part II**
    - **Paper I.** This paper describes the RF design of the elliptical cavity. After introducing the RF parameters necessary to quantify the performances of the cavity and a list of specifications for the cavity itself, the design of the cavity is carried out starting from the inner cell. The RF design is concluded by the design of the end cell.

- **Paper II.** This paper describes the mechanical design of the cavity. The main aspects of the mechanical design are first reviewed and they are followed by the simulation results. The paper is concluded by a table that summarizes the mechanical performances of the cavity.
- **Paper III.** This paper reports a mathematical description of the hollow cavity problem. The main result concerns the existence of an orthonormal basis of eigenfields which can be used to express an arbitrary field in a hollow cavity. This result is at the basis of papers IV and V and it is thus fundamental.
- **Paper IV.** Starting from the results of paper III, this paper presents the estimation of higher-order-modes (HOMs) induced power dissipation in cavities. The excitation of HOMs can be detrimental to the beam quality and efficiency of the cavity. The problem is solved entirely in the time domain to include transient effects.
- **Paper V.** This paper presents the model of the cavity coupled to an external circuit. The model is useful in the contex of the design of the control system of the cavity.

List of Included Papers

1. **Paper I**. The RF design of the cavity has been carried out by the author of the thesis in its entirety. The program used to organize and automatize the design process has been written by the author of the thesis.

2. **Paper II.** The mechanical design of the cavity has been carried out by the author of the thesis in its entirety.

3. **Paper III.** G. Costanza, A. D. Ioannidis,
   “Remarks on the Mathematical Solution of the Hollow Cavity Eigenvalue Problem”,
   Progress In Electromagnetics Research Symposium Proceedings, Stockholm, Sweden, 2013.
   Contribution. The author of the thesis contributed in giving a description of the electromagnetic problem and in the general production of the paper.

4. **Paper IV.** G. Costanza, A. Karlsson
   “Time Domain Analysis of Higher Order Modes Induced Power Dissipation in Accelerating Cavities”,

Submitted to the *Journal of Electromagnetic Waves and Applications.*
Contribution. The paper has been written by the author of the thesis except the appendix. All the simulations and the main results have been derived by the author of the thesis. The program used to perform the simulations has been written by the author of the thesis.

5. **Paper V.** G. Costanza
"The Coupled Cavity in the Time Domain".
Contribution. The paper has been written by the author of the thesis in its entirety.

Other Publications

- G. Devanz, N. Bazin, M. Desmons, P. Bosland, P. Hardy, F. Leseigneur, M. Luong, F. Peauger, J. Plouin, D. Roudier, G. Olivier, G. Costanza
"ESS Elliptical Cavities and Cryomodules"

- G. Costanza
"On the Optimal Design of Elliptical Superconducting Cavities"
Proceedings of IPAC2014, Dresden, Germany.

- E. Cenni, C. Arcambal, P. Bosland, G. Devanz, X. Hanus, P. Hardy, V. M. Hennion, F. Leseigneur, F. Peauger, J. Plouin, D. Roudier, C. Darve, G. Costanza
"ESS Medium Beta Cavity Prototypes Manufacturing"
Proceedings of SRF2015, Whistler, BC, Canada, 2015.

Achnowledgments

THis thesis would have not been possible without the support of many. I wish to express my deep gratitude first and foremost to my supervisor Prof. Anders Karlsson for giving me the opportunity of being here, for his guidance and support. His presence has always been inspiring and motivating. I also extend my gratitute to the ESS for allowing me to work with them on a project of international relevance. I wish to thank all the professors of the group of electromagnetic theory for creating a positive and intresting environment. In particular I extend my gratitute to Prof. Mats Gustafsson, Prof. Gerhard Kristensson and Prof. Daniel Sjöberg for the useful discussions and especially for their inspiring presence which has been a key motivating factor in driving my research.

Furthermore I would like to thank my family for believing in me and for their support.

Lund, December 2016.

Gabriele Costanza

Contents

Part I

Introduction

The first part of the thesis is an introduction to accelerators and cavity design. The first chapter starts with an overview of the ESS project and its main features. The second section is a brief historical survey on accelerators (section 1.2). The second chapter is an introduction to cavity design (section 2.2) which is followed by a comment on accelerator efficiency (section 2.3).

Overview of the ESS project

The European Spallation Source is an international collaborative effort whose goal is the design and operation of a neutron source of unparalleled power and performance. The project itself has been conceived in the late 90's and will see the light in 2019, when the first neutrons will be produced. Sweden is the main contributor to the project but the ESS is the result of an international collaboration that sees Sweden and Denmark as co-hosts.

1.1 Main Features of the ESS

The accelerator can be divided in two parts, the warm section and the cold section, see figure 1.1. The warm section is the normal-conducting section of the accelerator and is in charge of generating and accelerating the proton beam with room-temperature devices. Moreover the accelerator is composed

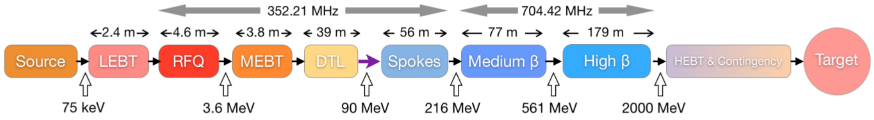

Figure 1.1: Layout of the ESS. Warm colors indicate the normal-conducting section of the accelerator, cold colors indicate the superconducting section.

of a series of interconnected subsystems that are explored in the following.

Normal-Conducting Section. The warm section is composed of several devices:

- The Microwave Discharge Ion Source, it is where the acceleration begins. It is a plasma based source designed not only to generate protons but also to accelerate them to an energy of 75 KeV.
- The Low Energy Beam Transport (LEBT) line is a section designed to shape and prepare the beam for the next stage, the RFQ. It is necessary because accelerating structures require a particle beam with well-defined characteristics in order to operate.
- The Radio-Frequency Quadrupole, it is the first RF accelerating structure, designed to accelerate particles from 75 KeV to 3.62 MeV. Moreover the particular geometry of the RFQ helps in confining and shaping the beam into bunches of particles.
- The Medium Energy Beam Transport (MEBT) line is another matching section made of focusing magnets and cavities, designed to prepare the beam for the Drift Tube Linac.
- The Drift Tube Linac (DTL), is a cavity type accelerating structure, designed to accelerate the beam from 3.62 MeV to 90 MeV.

Superconducting Section. After the warm section, the beam enters the cold section of the accelerator, which contains superconducting devices. Superconducting technology is becoming the dominant technology in high power particle accelerators, due to its efficiency. Most of the RF energy injected into the cavities is transfered to the beam rather than being wasted in heating. This section is composed of:

- Spoke Cavities. These cavities are located in the first stage of the superconducting (SC) section which takes the beam from 90 MeV to 216 MeV.

Spoke cavities are SC resonators equipped with spokes that deliver an accelerating gradient of 9 MV/m. In the ESS accelerator, double-spoke cavities with an accelerating mode resonating at 352.21 MHz are used. The cavity is covered by a Helium vessel and the space between the cavity and the vessel is filled with liquid Helium.

- Elliptical Cavities. The elliptical cavity section of the accelerator is composed of two different cavities, the medium-β and the high-β. This section is designed to bring the energy of the particle to the final energy of 2 GeV. There are 36, six-cell medium-β cavities and 84 five-cell high-β cavities which operate at gradients of 16.7 and 19.9 MV/m respectively. Also elliptical cavities are covered by the Helium vessel and cooled down to approximately 2 K.

RF System. All the accelerating devices of the accelerator require a great amount of RF power. The RF system is in charge of converting the AC line power to RF power, at either 352 or 704 MHz. The main components of the RF system are:

- Modulator. The modulator delivers high voltage DC power in pulses to the power amplifier.
- RF Power Amplifiers. Klystrons will be used to convert the pulsed power into RF power. Each elliptical cavity receives a peak power of 1 MW from the Klystron.
- RF Distribution. An RF system based of waveguides, circulators and directional couplers delivers the power to the accelerating devices.
- Low Level RF Control. This is the system that controls the interaction between the power amplifiers and the cavities. Each cavity has a pickup that picks up a signal that contains the information about phase and amplitude of the accelerating mode.

Beam Instrumentation. Once the accelerator is turned on and the cavities are filled with energy, the beam is ready to be accelerated towards the target. In order to monitor the performance of the accelerator a set of diagnostic tools is put in operation. Beam Instrumentation entails the design, production and operation of instruments needed to measure the beam characteristics and allows for a reliable operation of the accelerator within its performance requirements. The main instruments used are:

- Beam Loss Monitors. They protect the machine from damage, trigger the beam dump system and to assess the performance of the accelerator.

- Beam Current Monitors. They measure the current, for example by measuring the magnetic field generated by the beam with transformers or by intercepting the beam with a Faraday cup.
- Beam Position Monitors. They measure the beam position along the accelerator. These devices are often in form of pickups that measure the charges induced by the electric field of the beam. With four pickups it is possible to determine transverse position of the bunch. With multiple sets of position monitors the time of flight is measured.
- Emittance Measurement Unit. The emittance describes the quality of a beam and it is obtained by measuring its profile. For example, slit-grid scanners can be used. The beam passes through a narrow slit and the emerging particles are detected by a wire grid that measures the intensity of the bunch charge. The slit is scanned and a profile of the bunch is obtained.
- Longitudinal Bunch Profile Monitor. Longitudinal parameters are important as well. The longitudinal spread of the bunch is measured in terms of length, time or phase relative to the rf signal. The second measurement is the momentum spread, that is the deviation of the momentum relative to the reference particle.

Cryogenics. Another important subsystem is the cryogenic system that is required to cool down different parts of the accelerator such as the spoke and elliptical cavities, the target and some scientific instruments. The cryomodules that host the superconducting cavities use liquid Helium at 2 K, 4.5 K and 40 K while the target will use liquid Helium at 16 K.

1.2 Overview on the History of Accelerators

Nowadays accelerators feature futuristic technologies and are based on complex calculations, but the history of these machines started with simple ideas. The first device that was intended to use a potential difference to accelerate charged particle, is the Cockroft-Walton accelerator. It was build in England at the Cavendish Laboratory in Cambridge by John D. Cockroft and Ernest Walton. The accelerator operated thanks to a voltage multiplier that allowed to generate a potential of 800 kV. It was sufficient to accelerate protons in an evacuated tube and disintegrate a Lithium nucleus into two $\alpha-$particles.

The second step in the history of accelerators was done by Robert Van de Graaf [1]. The machine consisted in two insulated, hollow spheres of aluminum. A belt of insulating material is spun by a motor, depositing an electrical charge on the spheres. One sphere was charged positively, while the other, negatively. The potential difference between the spheres was of about 1.5 MV.

The history of modern RF accelerators starts in the 1930's with the idea of Rolf Wideröe. The only technology available at that time was based on charged conductors, that is, on steady voltages. Such machines were limited by the breakdown of vacuum, that is, an electric discharge would occur between two points at high potential difference. Inspired by the work of Gustaf Ising, Wideröe built the first linear accelerator, consisting of several gaps between plates, charged by an RF generator. He could accelerate potassium ions to 50 kV at 1 MHz.

Due to the lack of high frequency power sources, the development of linear accelerators slowed down in the 30's and 40's to leave space to the successful Cyclotron of Ernest Lawrence. The Cyclotron is a device made of two "D" shaped electrodes (see fig. 1.2). The electrodes are shaped like flat and hollow half cylinders and an alternating potential is applied between them. The particles are accelerated first towards one electrode and then towards the other. Magnets placed at the top and bottom of the electrodes provide the bending force to make the particle follow a spiral. As the particles spiral out towards the edge of the electrodes, they travel a longer and longer distance, acquiring more and more energy. During the 30's a number of improvements were made on the original design, the source was optimized to increse the yield of protons while the magnetic poles where shaped for a better confinement of the particles.

Cyclotrons are limited by the fact that the particles are no longer in synchronism with the RF generator, once they have acquired a high energy. A major advance in accelerator technology was obtained in the mid 40's, when the first electron synchrotron was built by E. M. McMillan. It is a circular machine made of curved magnets and accelerating gaps. As in the case of the Cyclotron, It also makes use of the idea of using the same accelerating "gap" (or cavity), to repeatedly accelerate particles while using a magnetic field to confine particles into a circular trajectory. As the particle energy increases, the strength of the magnets is increased to mantain constant the radius of the trajectory.

As the electrons move around the orbit they lose energy by emitting radiation, thus slowing down. The energy lost is given back to the electrons when they are accelerated by the fields in the cavities or "gaps". The higher the energy of the circulating electrons is, the higher the energy loss is. When the energy lost approaches 10 GeV it becomes progressively impractical to replace that energy with cavities. After the war, thanks to the invention of the magnetron and klystron, the research on linear accelerator was picked up again. Before the war the RF linear accelerator was still fundamentally similar to the Wideröe prototype. After the war instead a new type of accelerating structure

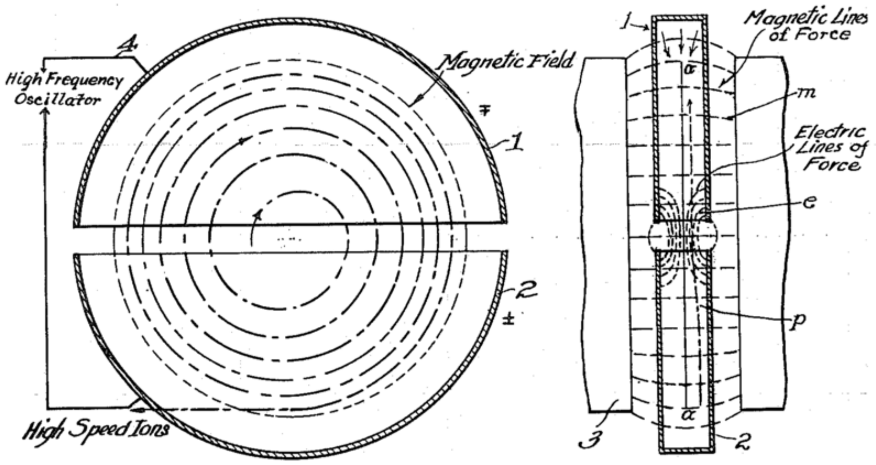

Figure 1.2: Schematic of the Cyclotron from Lawrence's Patent [2].

was proposed by L. Alvarez. It consisted on a sequence of drift tubes enclosed by a cylindrical cavity. The first drift-tube-linac was born. The idea was to excite a cavity mode with an RF amplifier, generating a uniform accelerating field between the gaps. The particle experiences an accelerating field between the gaps and is is shielded by the fields when passing through the small drift tubes. The final step into the world of modern accelerators was made at Stanford where the first iris-loaded waveguide was operated in the late 40's. Devices such as the Alvarez type drift-tube and the iris-loaded waveguides are still used today.

We have to wait until the mid 60's to find the first applicaiton of RF superconductivity. It was W. Fairbank, A. Schwettman and P. Wilson, that, for the first time, accelerated an electron beam with a superconducting cavity coated with lead. A few years later, in 1970, J. P. Turneaure and N. T. Viet successfully tested several superconducting Niobium cavities at 8.6 GHz demostrating a peak surface electric field of 70 MV/m [4].

Design Aspects of Elliptical Superconducting Cavities

2.1 Particle Acceleration in a Cavity

In modern particle accelerators, cavities are the devices that are used to accelerate the particle beam. There are many different types of cavities, each of which has its range of operation determined by the range of energies for which the cavity accelerates particles efficiently (see *energy acceptance* in 2.2.2). In all cases, cavities use an electric field, directed along the trajectory of the particles, to increase the energy of the particles. Figures 2.3 and 2.4 show the accelerating field in an elliptical cavities. The field oscillates at a frequency such that the particles passing through the center of the cavity always experience an accelerating field in the direction of the particle motion.

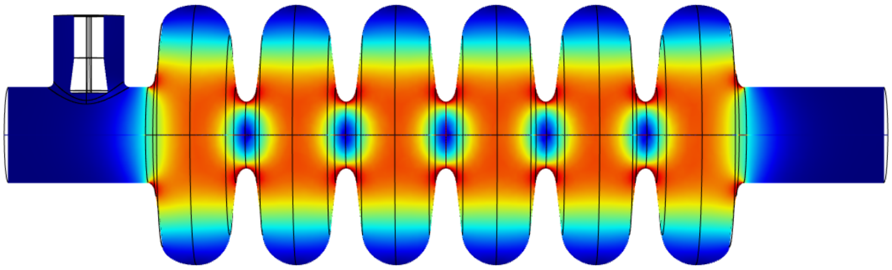

Figure 2.3: Electric Field amplitude of the accelerating mode of an elliptical cavity

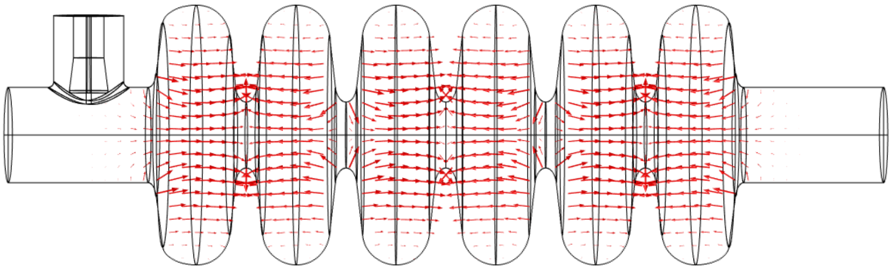

Figure 2.4: Electric Vector Field of the accelerating mode of an elliptical cavity

2.2 RF Design

A particle accelerator is made of many components such as the particle source, magnets, control and measurement systems, cryomodules, cavities and many others. Due to their efficiency and performance the devices used to impart the energy to the particles in modern accelerators are the resonant cavities. We can divide cavities into two groups, normal-conducting and superconducting. RF superconductivity applied to accelerator technology has advanced over the last decades, making superconducting cavities the technology of choice in many modern accelerators. The key advantages of this technology compared to the normal-conducting case, are the high accelerating gradient in both continuous wave and long pulse regimes and the high quality factors achieved thanks to the very low operating temperatures and the use of special materials such as Niobium.

Achieving a high acceleration efficiency is not the only critical aspect of cavity design, in fact, other aspects have to be taken into account at an early design stage, such as the electric and magnetic peak fields and the cell-to-cell coupling factor. Other aspects, such as the impact of the higher order modes (HOMs), the mechanical performances and the external quailty factor of the cavity, cannot be accounted for at the beginning of the design, because they require the design of the complete cavity. All these aspects interfere with each other, making the design of the cavity a matter of compromise.

Complex projects such as the ESS require years of gestation in order to reach a finalized accelerator design. As the accelerator design evolves, also the specification of its components change (see table 2.1), it is then advisable to produce a design that can withstand those changes as much as possible in order to avoid a complete redesign.

2.2.1 Linac Parameters

The main design parameters of the superconducting elliptical section of the ESS accelerator are chosen in order to reach the required neutron flux necessary to run the experiments [5, 6]. In 2013 the final accelerator layout was developed in order to meet the cost objectives. The accelerator will provide a 2.0 GeV proton beam in pulses of 2.86 ms with an average current of 62.5 mA, giving a 5 MW beam with a 4% duty cycle. Table 2.1 summarizes the accelerator parameters and the difference between the 2012 and the 2013 baseline linac called *OptimusPlus*.

Table 2.1: The main parameters of the elliptical section and the evolution of the design

Accelerator Parameters	Nov. 2011 Baseline	OptimusPlus
Energy [GeV]	2.5	2
Beam Power [MW]	5	5
Repetition rate [Hz]	14	14
Beam current [mA]	50	62.5
Beam pulse [ms]	2.86	2.86
Duty cycle [%]	4	4
Cavity Parameters		
Frequency [MHz]	704.42	704.42
Cells per Medium-β Cavity	5	6
Cells per High-β Cavity	5	5
Medium-β Cavities per Cryomodule	5	4
High-β Cavities per Cryomodule	8	4
Geometric-β, Medium-β Cavities	0.7	0.67
Geometric-β, High-β Cavities	0.86	0.92
Gradient, Medium-β Cavities [MV/m]	15	16.7
Gradient, High-β Cavities [MV/m]	18	19.9

2.2.2 Elliptical Cavities

Designing a cavity means finding and optimizing a geometry in order to fulfill the specifications. The design procedure starts by dividing the cavity in two fundamental elements, the inner cell and the outer cell. Due to the fact that the outer cells are attached to the beam pipes and couplers, such as the fundamental power coupler, HOM couplers and pickups, the end cells are usually different from the inner cells and are thus designed separately. Moreover, the inner cells have a more significant impact on the performances of the cavity since there are more inner cells than end cells.

Among all the cavity parameters, the *geometric* β, β_g, the *frequency* of the accelerating mode and the number of cells per cavity are usually chosen first. The choice of the frequency is not an issue related to the cavity technology only, but it is influenced by all the systems of the accelerator and their cost. In fact a considerable part of the total cost of the accelerator is given by the RF power amplifiers such as tubes and klystrons.

A particle with a normalized velocity $\beta = v/c$[1] $\approx \beta_g$, crosses a single cavity cell in half an RF period, thus seeing an accelerating field while passing through the cavity. The *geometric* β is in fact linked to the cell length L, by the relation, $\mathrm{L} = \beta_g \lambda/2$, where λ is the wavelength of the accelerating mode.

Both β_g and the number of cells have an impact on the acceleration efficiency. In order to be accelerated with maximum efficiency, a particle should have a speed within the energy acceptance interval where $\beta \approx \beta_g$. The energy acceptance is the range of energies (or velocities) a particle should have in order to experience approximately the maximum of the accelerating field. The boundary of the energy acceptance can be set for example at ±80% of the maximum accelerating field. From figure 2.5 we see that

- the more the particle velocity β is different from β_g, the lower the acceleration efficiency. This is also the reason why different types of cavities are necessary along the accelerator in order to cover a broad range of particle energies.
- The higher the geometric β of the cavity is, the higher is the energy acceptance, and the efficiency of the cavity.

The number of cells has also an influence on the energy acceptance of the cavity, in fact, the lower the number of cells, the wider the energy acceptance. An example of this behavior is in fig. 2.6. The number of cells is not determined only considering energy constraints but also considering the size of the cryostats and costs. It is necessary to find an acceptable compromise between the energy acceptance and the number of cells:

---

[1] c is the speed of light in vacuum

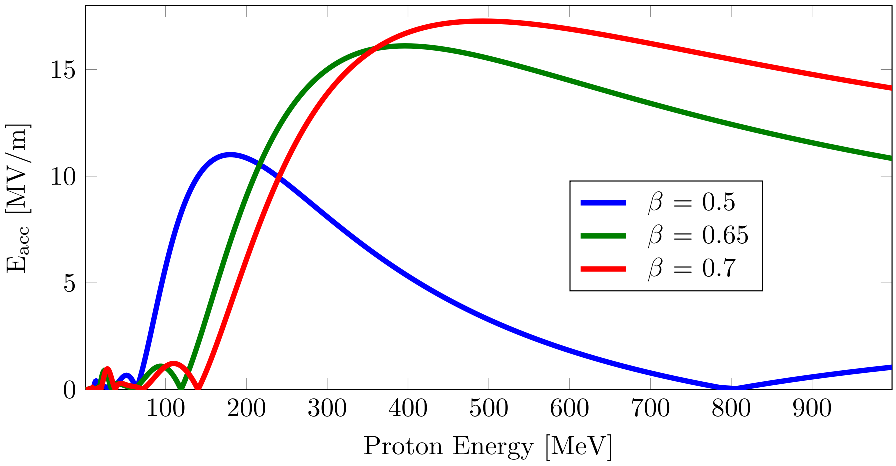

Figure 2.5: Accelerating field as function of the proton energy for three 5-cell cavities of different β_g.

- since every cavity is equipped with a power coupler and beam pipes which take space and do not contribute to the acceleration, it is desirable to increase the number of cells. On the other hand increasing the number of cells leads to a narrow energy acceptance. Consider also that in order to limit the number of sections of the accelerator the energy acceptance cannot be too small.
- The maximum of the accelerating field is obtained for the *optimum* β which is higher than β_g.

2.3 A Comment on the Limits of Particle Acceleration

In this section we want to analyze the efficiency of acceleration comparing different scenarios. Our point of view is to measure acceleration efficiency as the ratio between a real case and an ideal one, that is, considering ratios of the type

$$\frac{\text{realistic case}}{\text{ideal case}}. \tag{2.1}$$

Consider the acceleration of a point bunch of charged particles in a single cell cavity resonator. The longitudinal accelerating field experienced by the bunch

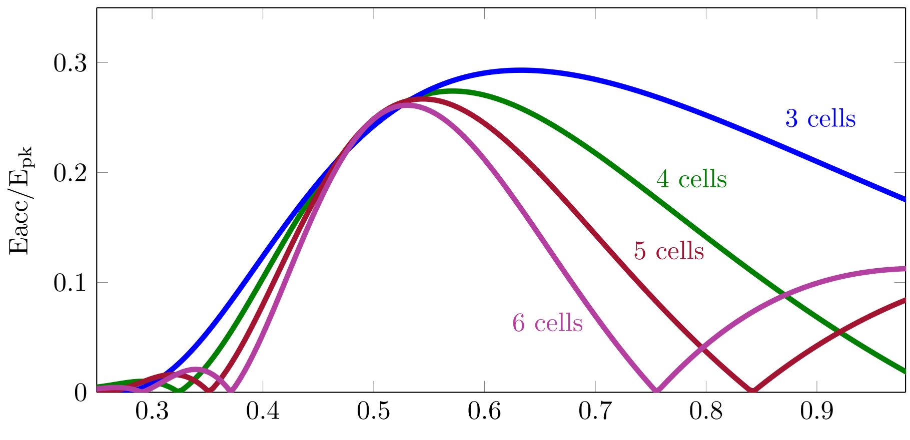

(a)

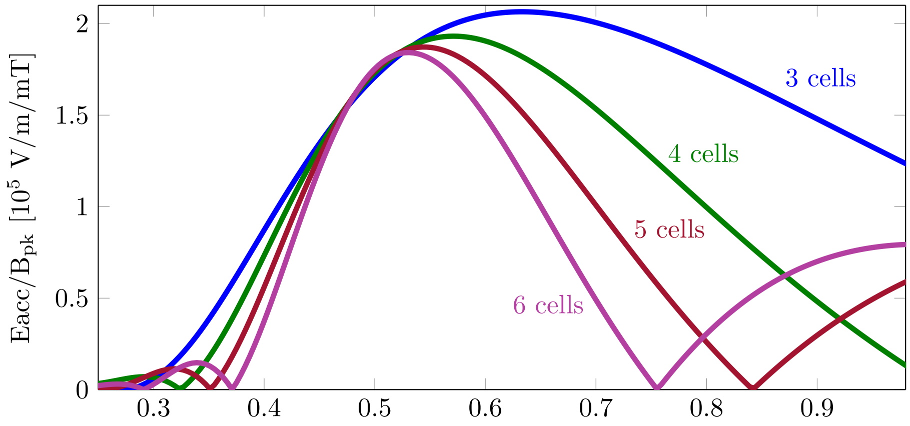

(b)

Figure 2.6: Accelerating field normalized with respect to the peak surface electric (a) and magnetic (b) field as function of the proton energy for a $\beta_g = 0.5$ cavity with different number of cells.

while passing along the axis of the cavity can be written as

$$E_z(r = 0, z, t) = E(0, z) \cos \left(\omega \frac{z(t)}{\beta(t)c} + \phi \right) \tag{2.2}$$

where ω is the resonant frequency of the accelerating mode, $\beta(t) = v(t)/c$ is the normalized particle velocity v at time t, and

$$z(t) = \int_0^t \beta(t')c\,dt'. \tag{2.3}$$

As a realistic model of an accelerating cavity we consider a cylindrical cavity resonator, also called pillbox. In this case, the field $\boldsymbol{E}(0, z)$ of the accelerating mode is longitudinal, that is, it is directed along the axis, and it is independent of z, that is $\boldsymbol{E}(0, z) = E(0, z)\hat{\boldsymbol{z}}$. The particle takes half an RF period to pass through the cavity, so that it experiences $E = 0$ at $z = \pm L/2$ and E_0 at $z = 0$. We choose $\phi = 0$, so that when the point bunch is at the center of the cavity, that is when $z = 0$, the field experienced by the bunch is its maximum value, which we denote with E_0 (see fig. 2.7). Since the RF field is oscillating in time, the particle does not always experience the value E_0, but all the values between 0 and E_0, as in the blue curve in fig, 2.7. This inefficiency is an *inherent limitation* of RF accelerators, that is, it stems from the fact that the fields are oscillating in the resonator. The energy gain of a point bunch passing on the axis of such a cavity is

$$\Delta W_{RF} = q \int_{-L/2}^{L/2} E(0, z) \cos\left(\omega \frac{z}{\beta c}\right) dz = 2qE_0 \frac{L}{\pi}. \tag{2.4}$$

This is the energy gain in the case of an RF pillbox cavity. Even in the case of a point bunch of infinite velocity, the field seen by the bunch during is passage along the axis of the cavity, would still not be equal to its maximum and the efficiency of acceleration would still not be the highest possible.

In a DC accelerator instead, the particle would experience a field of constant amplitude. We can think of substituting the pillbox with two large parallel plates, positioned at a distance L one from the other. We put a fixed potential difference between such that the field between them is constant and equal to E_0 and we obtain

$$\Delta W_{DC} = q \int_{-L/2}^{L/2} E_0\,dz = qE_0L. \tag{2.5}$$

We can consider the DC acceleration method, an ideal method of acceleration because then define the efficiency of the pillbox as the ratio

$$\frac{\Delta W_{RF}}{\Delta W_{DC}} = \frac{2}{\pi} = 0.637, \tag{2.6}$$

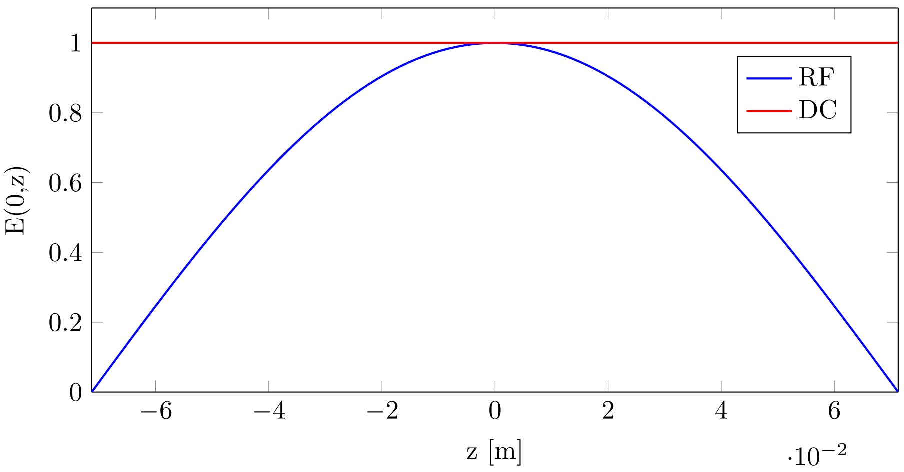

Figure 2.7: Electric field experienced by a particle passing on the axis of a cavity of length L=0.1426 m (blue) and the field experienced if the cavity was substituted by a parallel plate gap with a fixed potential difference equal to the maximum of the RF case (red). The value $E_0 = 1$ has been chosen.

that is, the acceleration efficiency between a realistic RF acceleration method and a DC acceleration method, is 63.7%.

In the literature it is customary to introduce the concept of *transit time effect*, which is another type of inefficiency. As mentioned, the particles passing through a cavity do not experience the maximum of the field at all times. If the particles could travel at an infinite velocity though, it would be possible for them to experience the same field along their trajectory. A new efficiency can be defined comparing the acceleration of bunches with finite and infinite velocity in an RF cavity [3]. The efficiency would then be 78.5%. It is impossible for the bunches to travel at an infinite velocity though. The conclusion is that the conventional RF acceleration methods have an inherent physical limitation which comes from the fact that RF fields are used.

References

[1] Andrew R. Steere, “A Timeline of Major Particle Accelerators”, Master Thesis, Michigan State University, 2005.

[2] https://en.wikipedia.org/wiki/Ernest_Lawrence.

[3] T. P. Wangler, “RF Linear Accelerators”, John Wiley & Sons, 1998.

[4] J. P. Turneaure and N. T. Viet, “Superconducting Nb TM010 Mode Electron-Beam Welded Cavities”, Appl. Phys. Letters,16, 333 (1970)

[5] S. Peggs editor, “Conceptual Design Report, ESS-2012-01.

[6] C. Darve, M. Eshraqi, D. Mcginnis, S. Molloy, E. Tanke, “Requirements for ESS Superconducting Radio Frequency LINAC”, Proceedings of IPAC2014, Dresden, Germay.

Part II

Design and Analysis of Elliptical Cavities

Paper I

RF Design

Gabriele Costanza.

Abstract

In this paper the RF design of the medium-β cavity for the ESS is presented. The final result is the complete design of a six-cell elliptical cavity. The tests retults, presented in the last section, show that the cavity satisfies the requirements of the ESS accelerator. The inner cell design is carried out first and is followed by the end cell design. The design method is based on a matlab script that organizes the simulations, tunes the cells to the design frequency and presents the results in form of plots and tables in order to facilitate the design.

RF Design

1 Introduction

In this paper the design of the medium-β cavity for the ESS is presented [1]. First a description of the geometry is given in section 2 followed by the description of the quality factors that are necessary to assess the quality of the cavity design in section 3. In section section 5 the design method is presented along with the results of the simulations. The design is divided in two parts. The first part of the design concerns the inner cell (section 5.1), while the second part is about the end cell (section 5.2). Every cell is made with two cups (see fig. 1) which are welded together with an electron beam. An infinite number of modes exist in the cavity, but the design aims at optimizing the RF performances of the accelerating mode. The fundamental mode, also called the π mode, is axially symmetric and has a phase shift of π between adjacent cells (see fig. 2.4). This is the accelerating mode. The RF-system excites this mode through a coupler that is attached to cavity. In the first stage of the design of the cavity the coupler is neglected.

The design method is based on a MATLAB script that organizes the simulations, tunes the cells to the design frequency and presents the results in form of plots and tables in order to facilitate the design. After the RF design, the mechanical design is presented. The design is not only complicated by the stringent specifications but also by the fact that the cavity is symmetric and only two cups are used.

2 Geometrical Parameters

Elliptical cavities consist in a series of so called elliptical cells. The name comes from the fact that the profile of each cell is derived from two ellipses and a tangent between them (see. fig. 1). The initial design of the accelerator featured medium-β cavities with 5 cells, a number that was later increased to 6. The geometry of an elliptical cell is decomposed in simple geometrical objects, such as ellipses, a tangent between them and straight lines. The outline of an elliptical half cell is in figure 1.

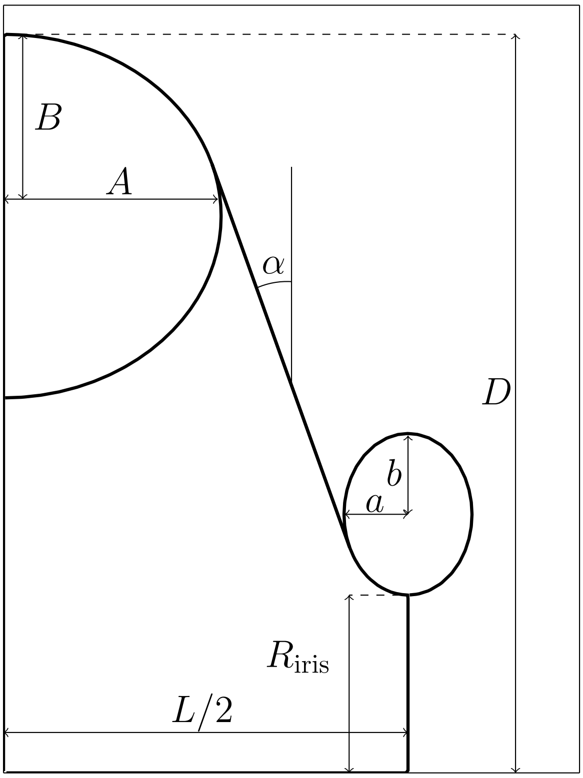

Figure 1: Geometry and parameters of an elliptical half cell.

The geometrical parameters that characterize the ellipses are

- A, a: width of the ellipses,
- B, b: height of the ellipses.

Other geometrical parameters are

- L: length of the cell,
- R_{iris}: radius of the iris aperture,
- D: radius of the cell,
- α: inclination of the side wall of the cell.

3 Quality Factors and Performance

In this section we give the parameters that are necessary to measure the performance of a cavity. Let us consider a cavity of volume Ω enclosed by a surface S. The first quantity to be defined is the *accelerating field*:

$$E_{acc} = \frac{1}{L_{acc}} \left| \int_0^{L_{tot}} E_z(0,0,z)\, e^{\mathrm{i}\omega_0 z/\beta c}\, dz \right| = \frac{|V|}{L_{acc}}, \tag{1}$$

where L_{acc} is the active length of the cavity, that is, the length of the cavity excluding the beam pipes, while L_{tot} is the total length of the cavity, including the beam pipes. $E_z(0,0,z)$ is the component of the complex electric field along the axis of the cavity, ω_0 is the angular frequency of the mode considered. Notice that

- We have assumed that the change in velocity of the particles is negligible, so that $t = z/(\beta c)$.
- The accelerating field depends on the normalized velocity β.
- The phase of the field with respect to the position of the particle is not taken into account. E_{acc} is the maximum of the accelerating field that can be obtained.

The intrinsic quality factor quantifies the performances of the cavity with respect to the power dissipation and it is defined as

$$Q = \frac{\omega_n U}{P_d}, \tag{2}$$

where U is the average electromagnetic energy stored in the cavity, defined as

$$U = \frac{\epsilon_0}{2} \int_\Omega |\boldsymbol{E}|^2\, d\Omega = \frac{\mu_0}{2} \int_\Omega |\boldsymbol{H}|^2\, d\Omega, \tag{3}$$

and where P_d is the average power dissipated in the cavity walls:

$$P_d = \frac{1}{2} \int_S R_s |\boldsymbol{H}|^2\, dS. \tag{4}$$

R_s being the surface resistance of the cavity. If R_s is constant along S we can define the *geometric factor* G

$$G = R_S\, Q = \frac{\omega_0 U}{\int_S |\boldsymbol{H}|^2\, dS} = \omega_0 \mu_0 \frac{\int_\Omega |\boldsymbol{H}|^2\, d\Omega}{\int_S |\boldsymbol{H}|^2\, dS}, \tag{5}$$

which is dependent only on the geometry of the cavity. Another important quantity dependent only on the cavity geometry is the ratio R/Q:

$$\frac{R}{Q} = \frac{\omega_0 |V|^2}{U} = \omega_0 \frac{(E_{acc} L_{acc})^2}{U}. \tag{6}$$

A high quality cavity is able to produce a high accelerating gradient E_{acc} without *quenching* [2] or excessive electron emission [3]. Quenching is the transition of the cavity from the superconducting state to the normal-conducting state. Typically this transition is initiated in a small area of the surface. If the local dissipation is too strong, an avalanche effect is triggered and the normal conducting zone spreads to the whole cavity with a corresponding sharp increase in power dissipation. Electron emission is another problem that limits the cavity performance. When the surface electric field is high, electron emission occurs, especially if the surface roughness of the cavity is high and if there are inclusion or impurities on the metal surface. Electrons emitted by the surface find themselves in the oscillating RF field and, if the electrons are symcronzed with the field, they can be accelerated towards the surface multiple times. If the energy of the electrons impinging on the cavity surface is sufficient, more electrons are emitted and an avalanche effect may occur leading to an electric discharge in the cavity. This effect is called *multipacting*.

In terms of cavity design, it is necessary to keep both the surface peak electric field and the surface peak magnetic field as low as possible to avoid quenching and electron emission. The peak fields are usually normalized with respect to the accelerating gradient of the cavity, giving the quantities

$$\eta_E = \frac{E_{pk}}{E_{acc}}, \qquad \eta_H = \frac{H_{pk}}{E_{acc}} \left[\frac{mT}{MV/m} \right]. \tag{7}$$

By reducing these normalized peak fields one can increase the accelerating field without risking quenching or electron emission.

The next parameter to be introduced is the *field flatness*, ff, as a measure of the equalization of the field distribution of the accelerating mode in the different cells. If the field flatness is small, it means that most of the energy of the accelerating mode is concentrated in one cell of the cavity, thus, not only the particles will experience a non-even acceleration passing through the cells, but the cell which stores most of the energy will also have the highest peak fields, which is dangerous for quenching and multipacting and will ultimately limit the performance of the cavity. The field flattness is also expressed in percent as

$$ff = \frac{100(E_{max} - E_{min})}{\frac{1}{N} \sum_{i=1}^{N} E_{c,i}} \tag{8}$$

where E_{max} and E_{min} are the maximum and minimum value of the electric field on the cavity axis while $E_{c,i}$ is the maximum of the axial field in cell i.

4 Multi-Cell Cavities and Passband Order Modes

Elliptical cavities can be modeled as a periodic sequence of electrically coupled single cell resonators, where each period consists of one cell. Each cell is connected to the next through an aperture called "iris", as shown in figure 2. The gray area representing two cups joined together at the iris, is also called "dumbbell".

A periodic arrangement of cells, gives rise to a set of *normal modes* [4], each of which is characterized by a specific field distribution and frequency. In general, each cavity mode has a set of normal modes associated to it, spanning a frequency band, called the *passband*. For example, the fundamental (or lowest frequency) mode of an elliptical cavity is the TM_{010} mode which, in an N-cell cavity, is characterized by N normal modes. The normal modes differ from each other not only in frequency and for the field distribution, but also on the so called *phase advance* per cell. The phase advance per cell is the difference between the phase of the fields from one period to the next. Figure 3 shows the field profiles and phase advances for the normal modes of the fundamental passband of a six-cell elliptical cavity. We can make some remarks:

- at the top left of the figure we see the field profile of the accelerating π mode. Its field is characterized by a phase shift of 180° degrees from one period to the next. Moreover, the longitudinal electric field is evenly distributed along the cavity in the sense that equal peaks in the electric field are formed at the center of every cell.
- All the other normal modes are characterized by an uneven distribution of the field along the cells, moreover the phase of the field from one cell to the next does not change continuously. For example, the field of the $5\pi/6$ mode, has the same phase in the two innermost cells, while the field is stronger in the outermost cells, as seen in figures 3 and 4.

During the inner cell desing phase, it is customary to use the dumbbell as a geometry prototype (see fig. 5), since it is possible to find both its normal modes, the *zero* and the π (or accelerating) mode, with a single simulation, using the *perfect electric conductor* boundary condition. The zero mode is not present in the full cavity equipped with beam tubes, but the frequency of the zero mode is useful later in the calculatiion of the *cell-to-cell coupling*.

The cell-to-cell coupling, $\mathrm{K_{cc}}$, quantifies the coupling between the cells of

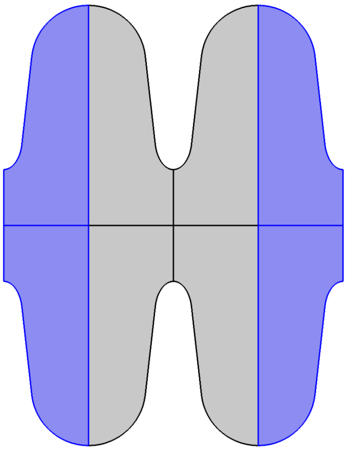

Figure 2: Two cells joined together at the iris. The gray area, representing two cups joined together, is also called “dumbbell”.

the cavity. For an N cell cavity, it can be shown [4] that the frequencies of the normal modes are distributed according to the formula

$$f_{q\pi/N} = f_0\sqrt{1 + K_{cc}(1 - \cos(q\pi/N))}, \qquad \phi = 1, 2, \dots, N, \tag{9}$$

with

$$K_{cc} = 2\frac{f_\pi - f_0}{f_\pi + f_0}. \tag{10}$$

where $q = 0, 1, \dots, N$, is the normal mode index and f_0 and f_π are the frequencies of the zero mode and of the π mode respectively. The cell-to-cell coupling factor is often expressed in percent which amounts to multiplying the last equation by 100.

5 Cavity Design

Designing the cavity means finding and optimizing its geometry in order to fulfill the specifications. It is advisable to design the inner and the outer cells separately since the outer cells are attached to the beam pipes and will then have a different geometry. Moreover the full cavity has too many geometrical parameters to optimize and that would make the design process impractical. It is convenient to use a program that automatizes the design of the cavity, for example by exploring the parameter space, tuning the cells, executing the

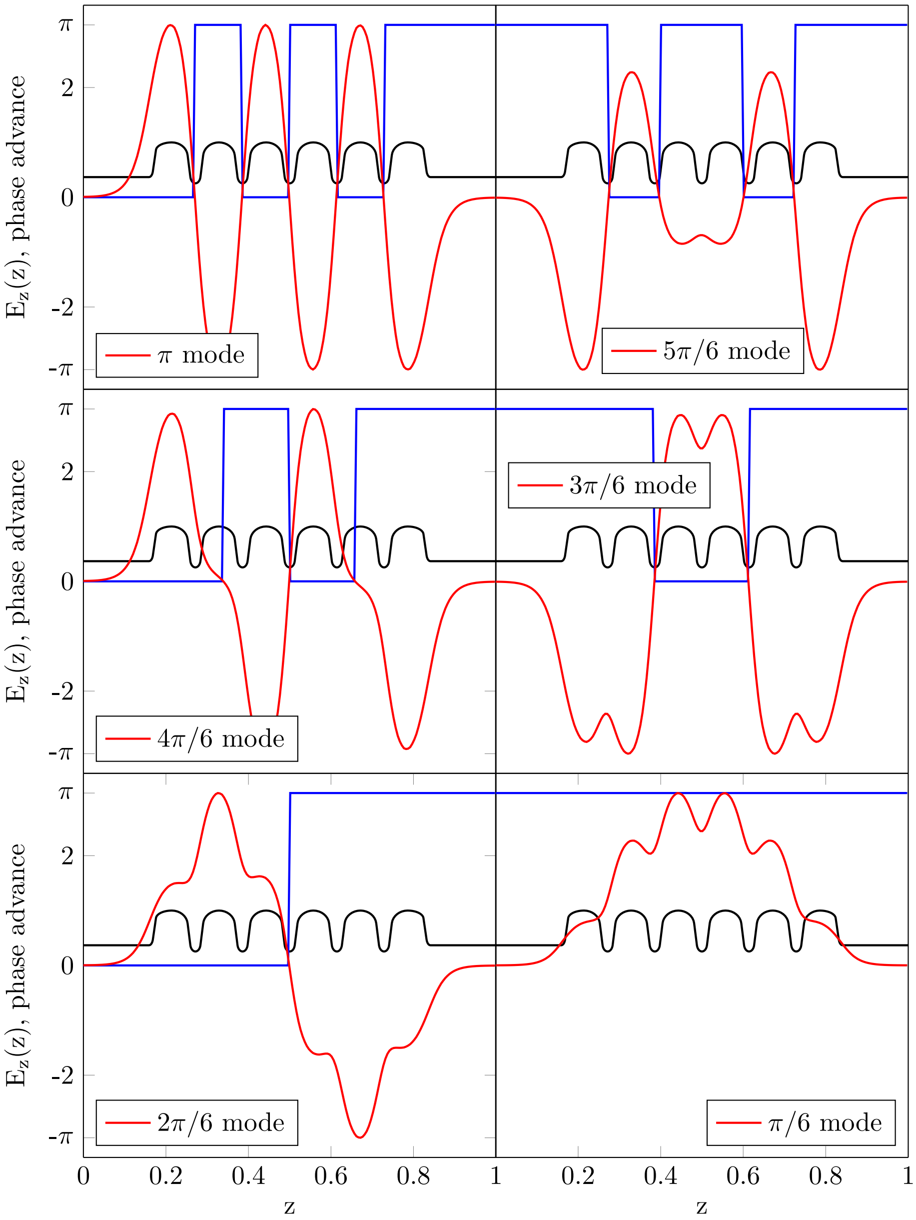

Figure 3: Longitudinal field distributions (red) and phase advance per cell (blue) of the normal modes of the first passband corresponding to the TM_{101} mode. A six-cell cavity (black) has been used.

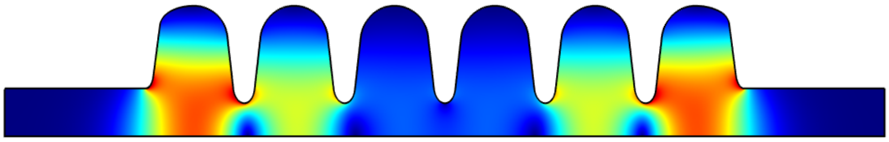

Figure 4: Amplitude of the electric field of the $5\pi/6$ mode in a six-cell elliptical cavity. Most of the electromagnetic energy is stored in the external cells.

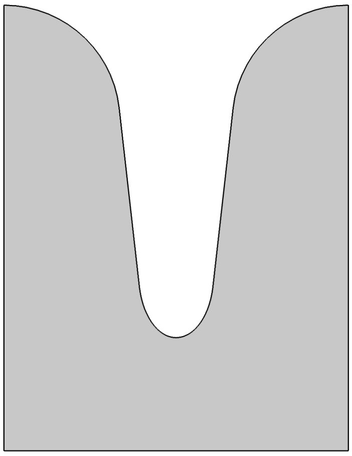

Figure 5: Axisimmetric version of the “dumbbell”. It is customary to use this geometry in the simulations.

simulations and calculating the quality factors. In the design process, the commercial software COMSOL MULTIPHYSICS was used. It is possible to link the simulator to MATLAB, through the COMSOL WITH MATLAB interface.

Much effort was spent in developing a MATLAB script that organizes the simulations and tunes the cells through COMSOL by varying the parameter D. The input to the script are the boundaries of the parameter space, that is the maximum and minimum values for the parameters A, a, B and b, while R_{iris} is fixed. R_{iris} has the strongest influence on the RF parameters, that is why it can be kept fixed while varying all the other geometric parameters.

Concerning the inner cell design, it is convenient to simulate the dumbbell made of two inner cells connected at the iris, in order to obtain the fields and frequencies of both the zero and the π mode necessary to calculate the cell-to-cell coupling.

The specifications of the cavity are listed in table 1 [1]. At the time of the design of the cavity the electric peak field was defined to be 40 MV/m but was later increased to 45 MV/m. Also the nominal accelerating gradient was increased from 15 MV/m to 16.7 MV/m and the number of cells were increased from 5 to 6, following the refinement of the overall accelerator design.

Table 1: Techical requirements for the medium-β cavity

Parameter	Value
Freq. Acc. Mode [MHz]	704.42
Number of Cells	5
Geometric Beta	0.67
Acc. Gradient (Peak) [MV/m]	16.7
Acc. Gradient (Nominal) [MV/m]	15
Max. Surf. E field (Nominal) [MV/m]	≤ 40
Max. Surf. E field (Peak) [MV/m]	≤ 45
Max. Surf. H field (Nominal) [mT/MV/m]	≤ 80
Max. Surf. H field (Peak) [mT/MV/m]	≤ 90
External Q	$5.9e5 \leq Q_{ext} \leq 8e5$
Intrinsic Quality Factor	$Q \geq 5e9$

5.1 Inner Cell Design

The first parameter to choose is the cell length L, which is determined by $L = \beta_g \lambda/2$. In our case, since the frequency of the accelerating mode is 704.42 MHz and $\beta_g = 0.67$ (see table table 2.1) we have

$$L = \beta_g \frac{\lambda}{2} = 0.1426 \quad [m]. \tag{11}$$

The geometric parameter that most influences the performances of the cavity is the radius of the iris (R_{iris}), it is then important to chose this parameter first. One way to proceed is to make an initial guess and perform simulations that span a wide section of the parameter space in order to understand if the choice of R_{iris} is satisfactory. The initial guess can be driven by existing cavity designs with similar β_g and frequency.

A small radius of the iris, R_{iris}, leads to a higher accelerating field, which in turn leads to

- lower normalized surface peak fields $\mathrm{E_{pk}/E_{acc}}$ and $\mathrm{B_{pk}/E_{acc}}$,
- higher R/Q,
- lower cell-to-cell coupling, $\mathrm{k_{cc}}$.

After exploring the parameter space with a large number of simulations, a section of it has been selected for further analysis. The radius of the iris has been chosen to be $R_{\text{iris}} = 47$ mm. Moreover only the cells with a side wall inclination $\alpha \gtrsim 7°$ were considered. For smaller angles, the cleaning and drying of the cavity after the chemical treatment becomes progressively harder. To determine the other geometric parameters, a parametric sweep was done (see table 2).

Table 2: Parametric sweep for the inner cell design.

Geometric Parameter [mm]	start [mm]	stop [mm]	# steps
A	45	48	4
B	48	52	5
a	11.5	15.5	5
b	24	27	4

Figures 6 to 10 represent a typical scatter plot of the results. Every point

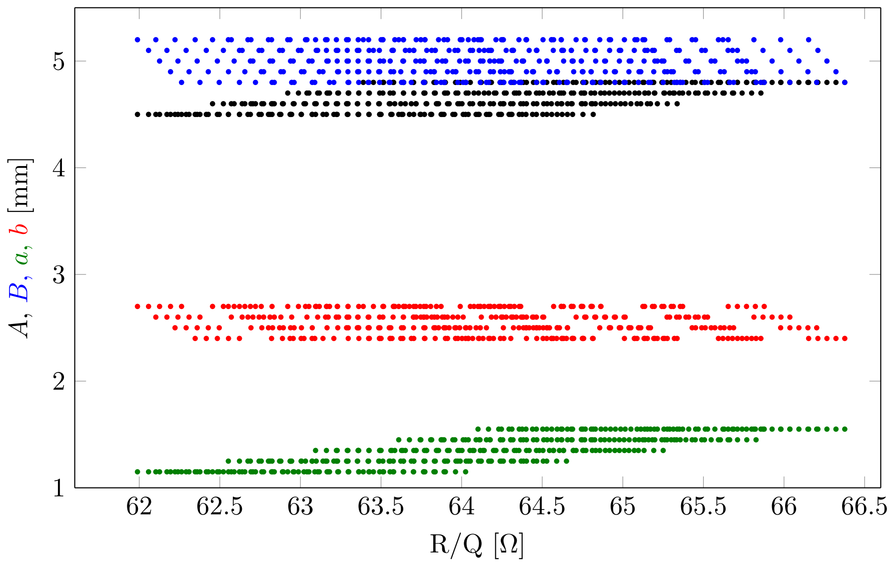

Figure 6: R/Q as function of the geometric parameters A, B, a and b.

in those plots represent a simulated inner cell. Figures 11 to 15 are *main effect plots*. These plots show the variation of a dependent variable averaging over its different levels obtained when the other independent variables are varied. These plots allow to draw general conclusions about each geometric parameter:

- the R/Q increases when the side wall angle α decreases, see fig. 11.
- The Normalized Surface Peak Electric Field is controlled almost entirely by the parameter a, and it varies non linearly, see fig. 13.
- The cell-to-cell coupling is also mainly determined by a. There is then a clear trade off between K_{cc} and the Surface Peak Electric Field.

Figures 16 to 20 are *interaction plots*. These plots explain the variation of the RF parameters in more detail since the different levels obtained for the RF parameters are not averaged. Among the ellipses paramers A, B, a and b, the width of the ellipses A and a, are the most sensitive parameters, while B is the least sensitive. Notice also that A and a control the inclination of the side wall of the cell, α. In particular we notice that

- Increasing A and a (small inclination α) leads to an increase of R/Q (see also the main effects plot 11) and a decrease of the electric peak field but

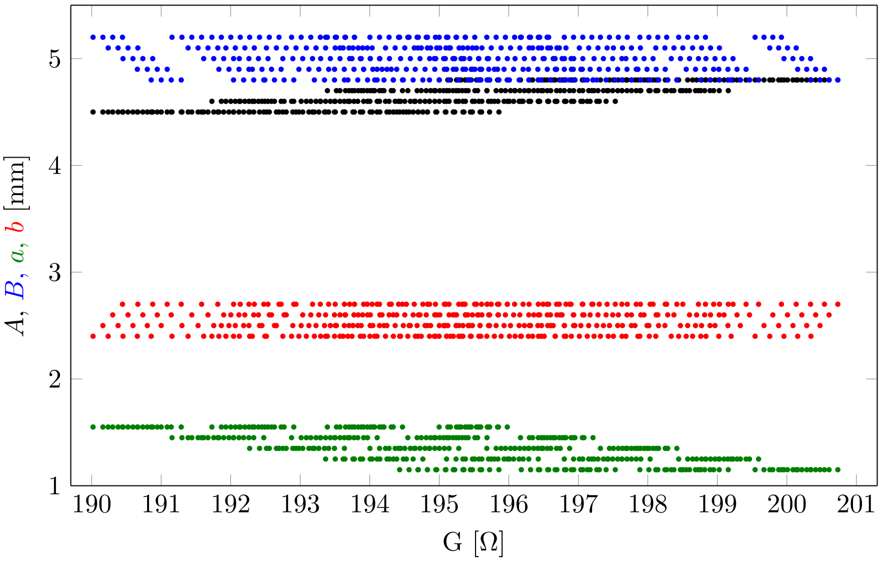

Figure 7: G as function of the geometric parameters A, B, a and b.

it has a detrimental effect on the cell-to-cell coupling (figures 13 and 15). The curves on top have a strong inclination, denoting that A and a have a strong influence on R/Q. The curves on the bottom instead, are almost horizontal, denoting that B and b have a small influence on R/Q.

- The geometric factor G is influenced mostly by A and a (see fig. 7 and fig. 12). A small side wall inclination α (or a large A and a small a) increases the geometric factor.

- The parameter a is important in determining the cell-to-cell coupling, $\mathrm{K_{cc}}$ while A has a small effect. This is evident in figure 10 but also in the main effects plot 15.

- Since the maximum of the peak electric field is at the intersection between the side wall and the small ellipse, the normalized peak electric field is mostly influenced by the dimensions of a and b of the small ellipse. See the main effects plot 13 and the interaction plot 18. Notice also the pronounced non linearity of $\mathrm{E_{pk}/E_{acc}}$ with respect to a.

- $\mathrm{B_{pk}/E_{acc}}$ is mostly determined by the parameter A, and to a second order by B and a, that is, the dome ellipse dimensions are relevant for the peak

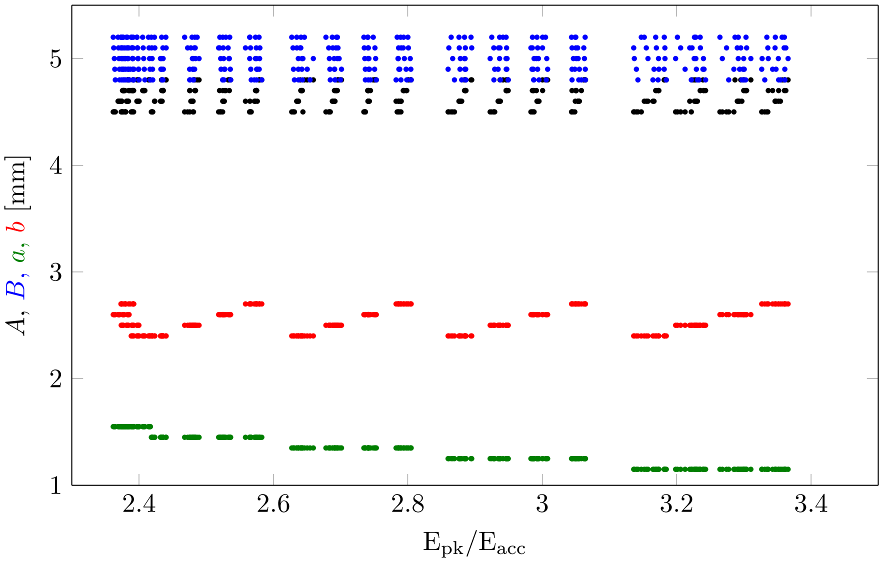

Figure 8: $\mathrm{E_{pk}/E_{acc}}$ as function of the geometric parameters A, B, a and b.

magnetic field (see fig. 9, 14, 19). This effect is expected since the peak surface magnetic field is at the intersection between the side wall and the dome ellipse. Increasing A and decreasing a, decreases $\mathrm{B_{pk}/E_{acc}}$. Notice also the nonlinear dependence of $\mathrm{B_{pk}}$ with respect to a.

The plots in figures 16 to 20 show the variation of the RF quality factors against the interaction between the geometric parameters and summarizes the simulation results. In particular the plots in figure 18 confirm that the different levels of a have a strong influence on the electric peak field, while the other parameters have little influence. Similarly in fig. 19, the parameter A has the strongest influence on the peak magnetic field. Observe also the tradeoff between $\mathrm{E_{pk}/E_{acc}}$ and $\mathrm{K_{cc}}$ in figures 18 and 20. A high value of a lowers the cell-to-cell coupling as well as the peak electric field almost irregardless of the value of A.

As we see from the plots of this section, a trade-off has to be made between the geometric parameters in order to obtain satisfying performances. The final dimensions of the inner cell as well as the RF performances are summarized in table 3. All the design goals are met with a slight concession regarding the side wall inclination α and considering the more stringent and safer requirement of 40 MV/m of electric peak field at the accelerating gradient of 16.7 MV/m.

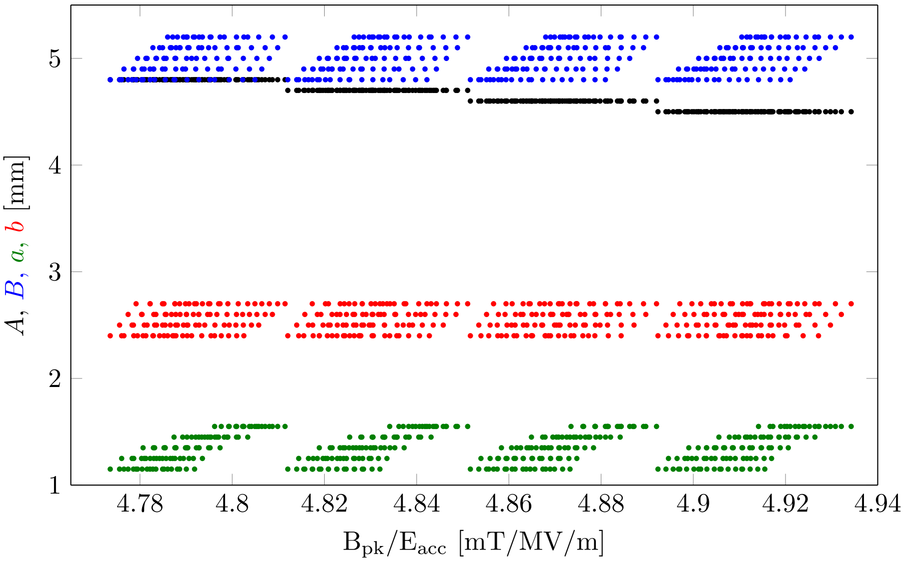

Figure 9: B_{pk}/E_{acc} as function of the geometric parameters A, B, a and b.

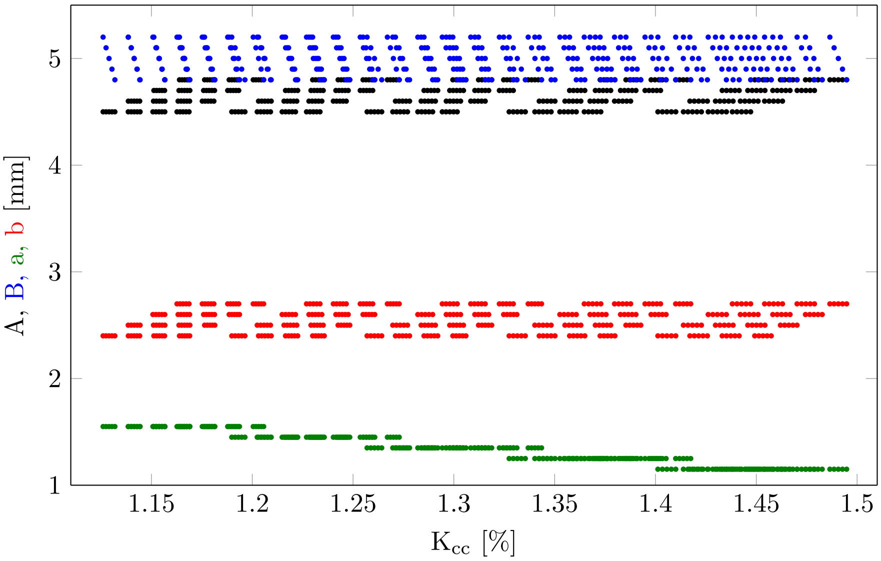

Figure 10: K_{cc} as function of the geometric parameters A, B, a and b.

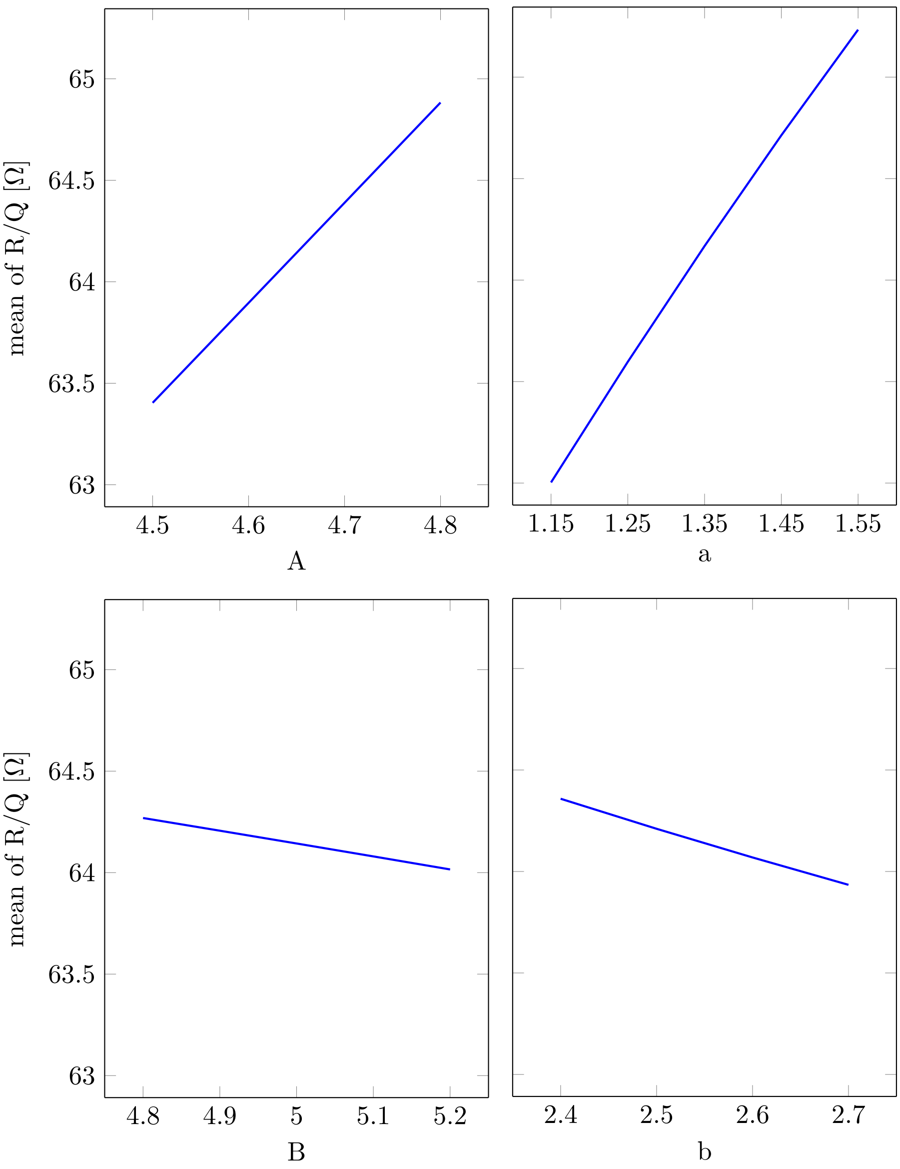

Figure 11: Main effects plot for R/Q

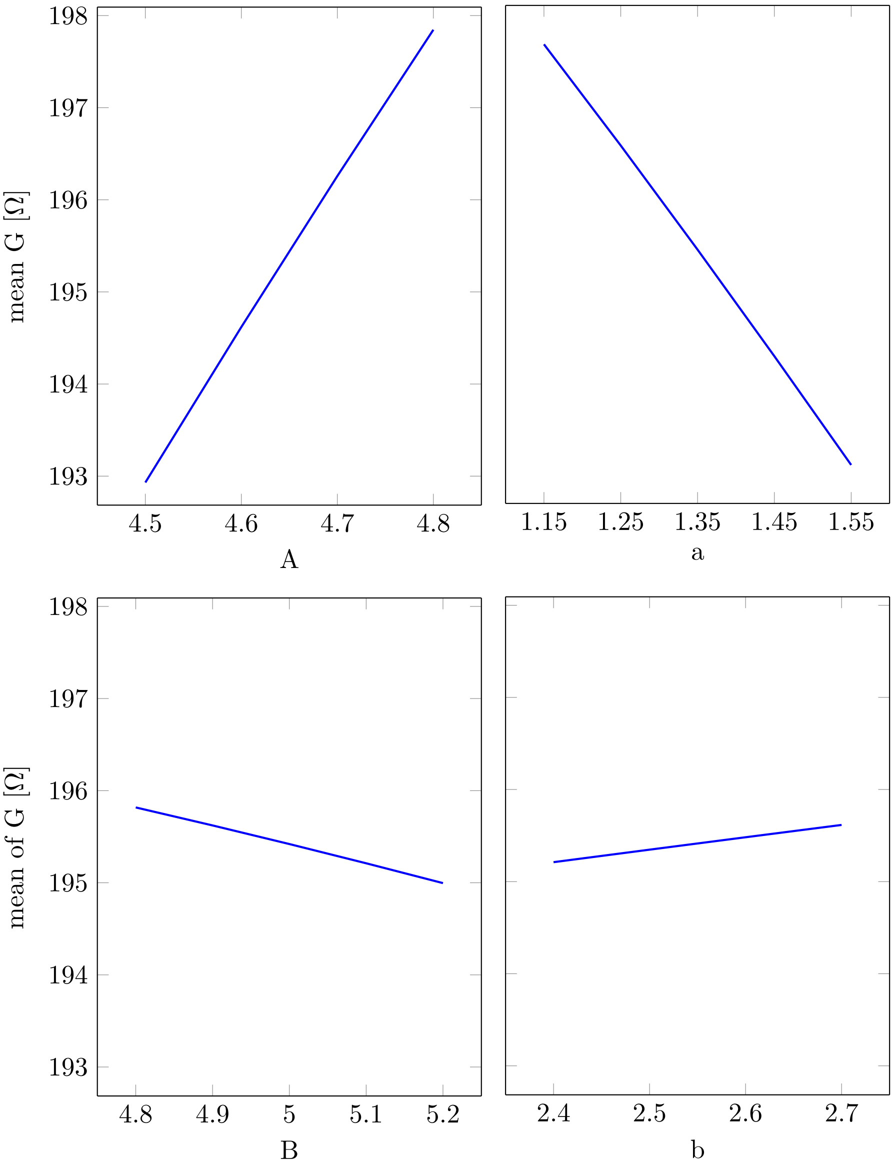

Figure 12: Main effects plot for G

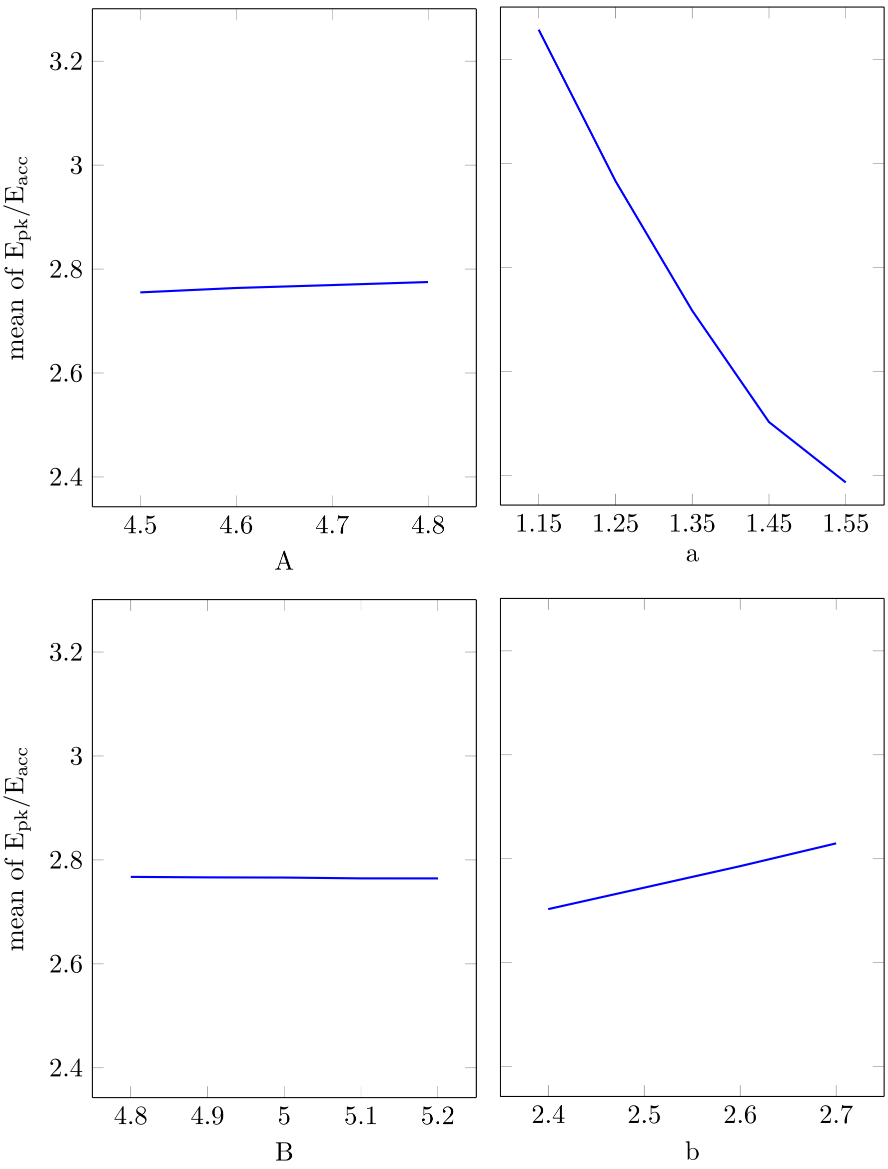

Figure 13: Main effects plot for E_{pk}/E_{acc}

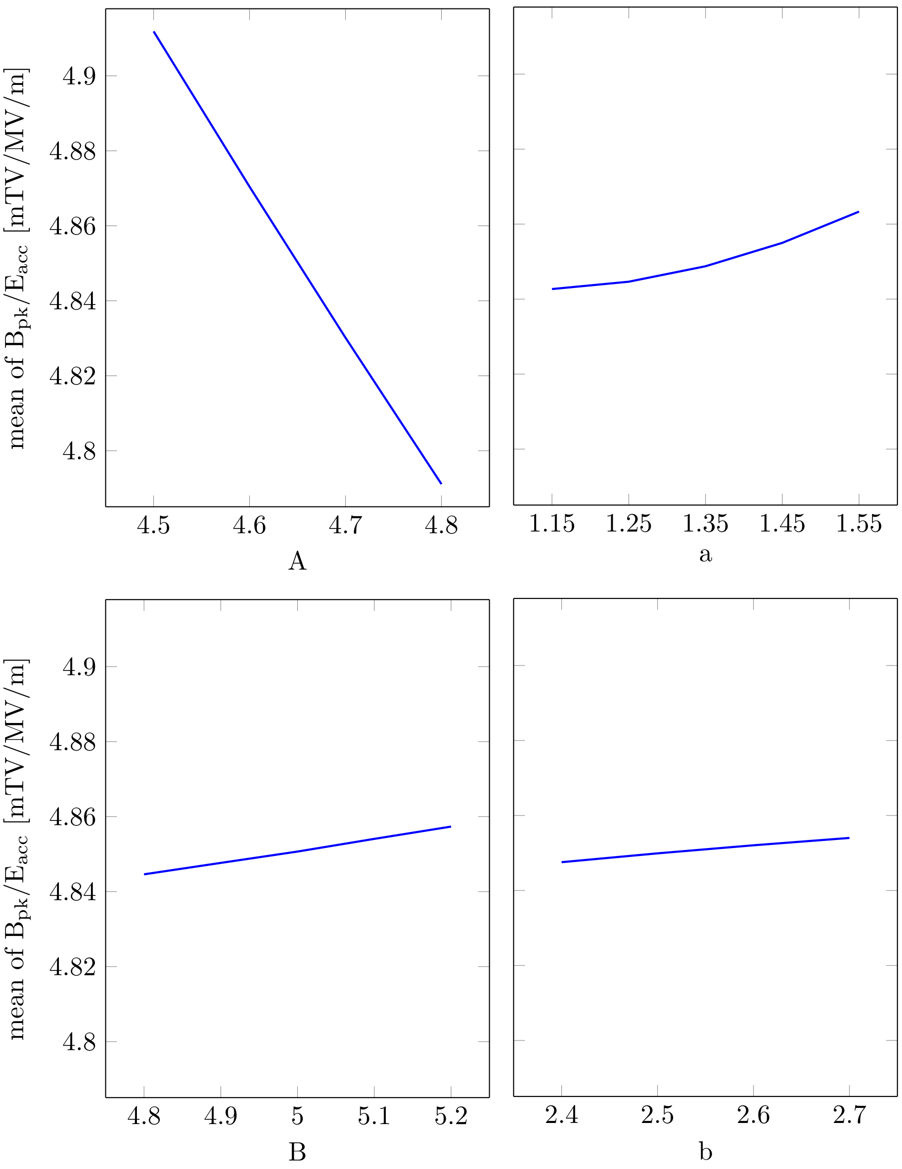

Figure 14: Main effects plot for B_{pk}/E_{acc}

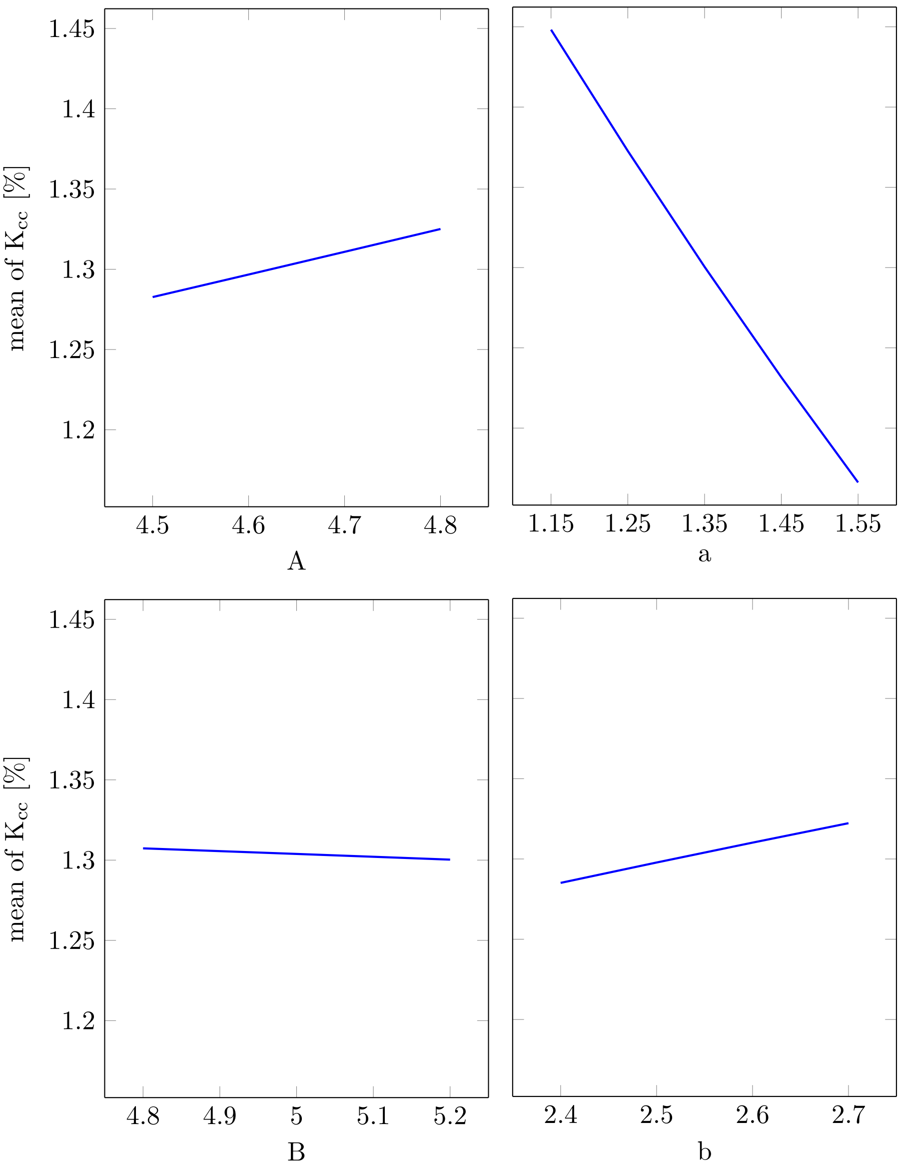

Figure 15: Main effects plot for K_{cc}

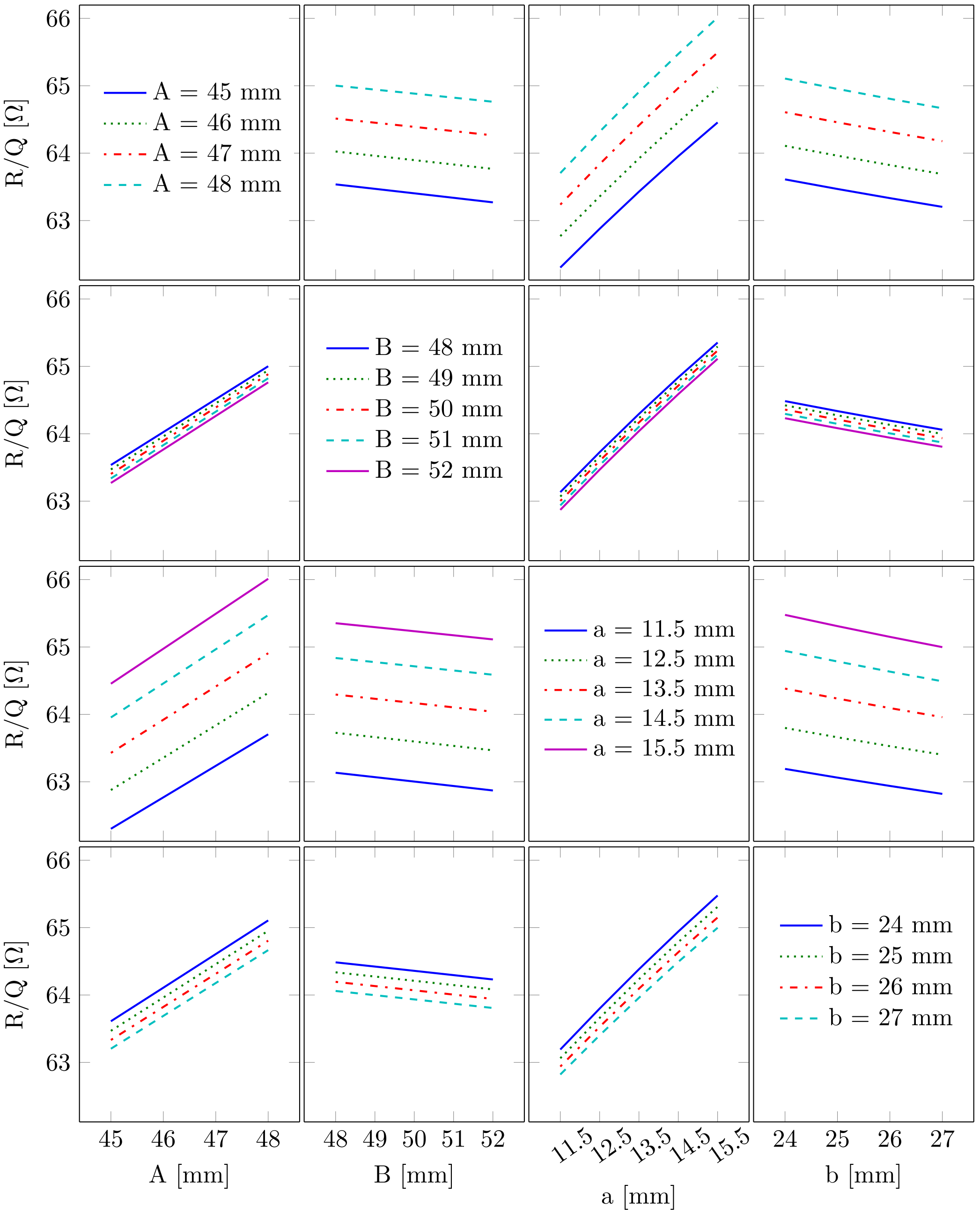

Figure 16: Interaction plot, R/Q over the geometric parameters for the inner cell design.

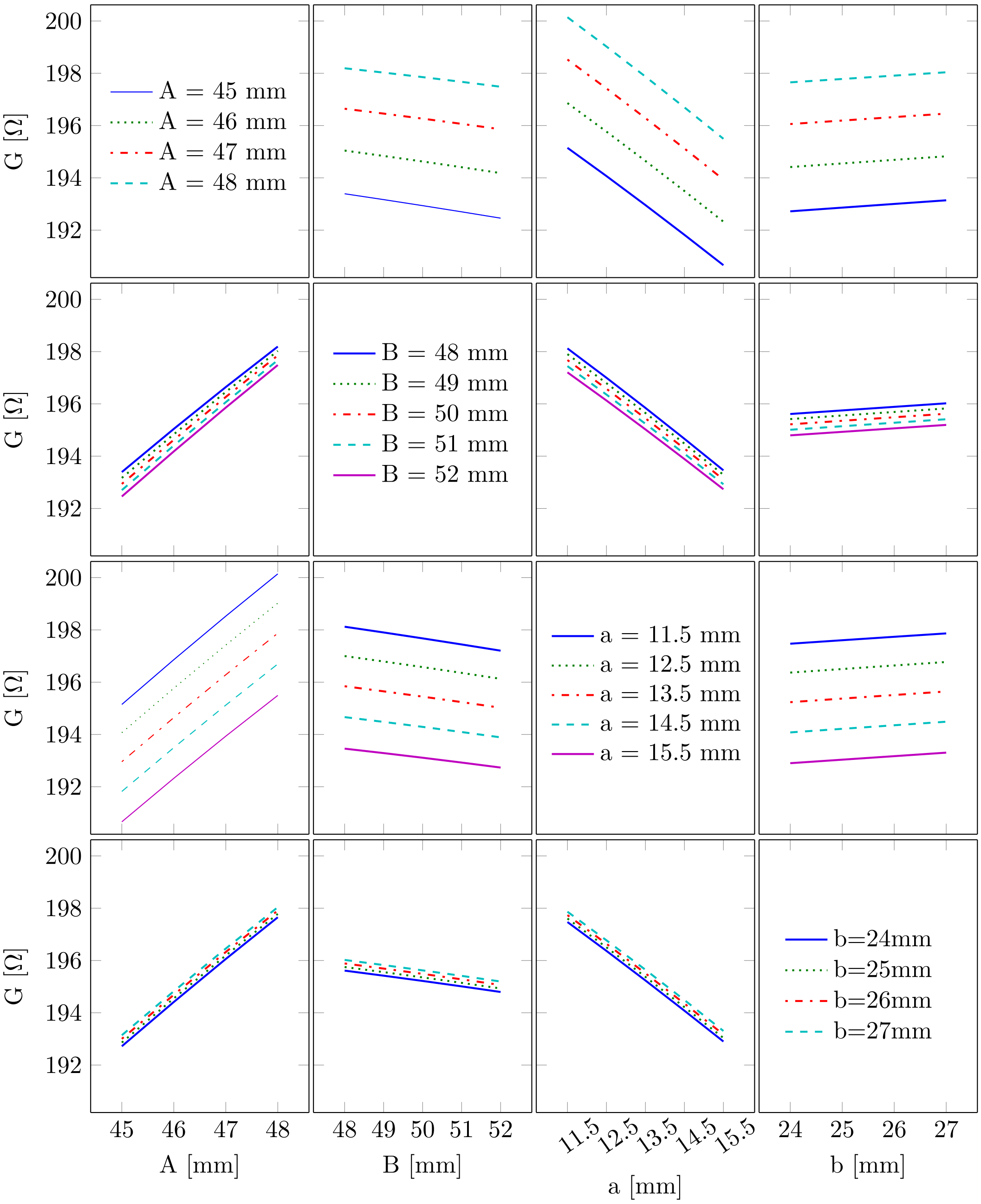

Figure 17: Interaction plot, G over the geometric parameters for the inner cell design.

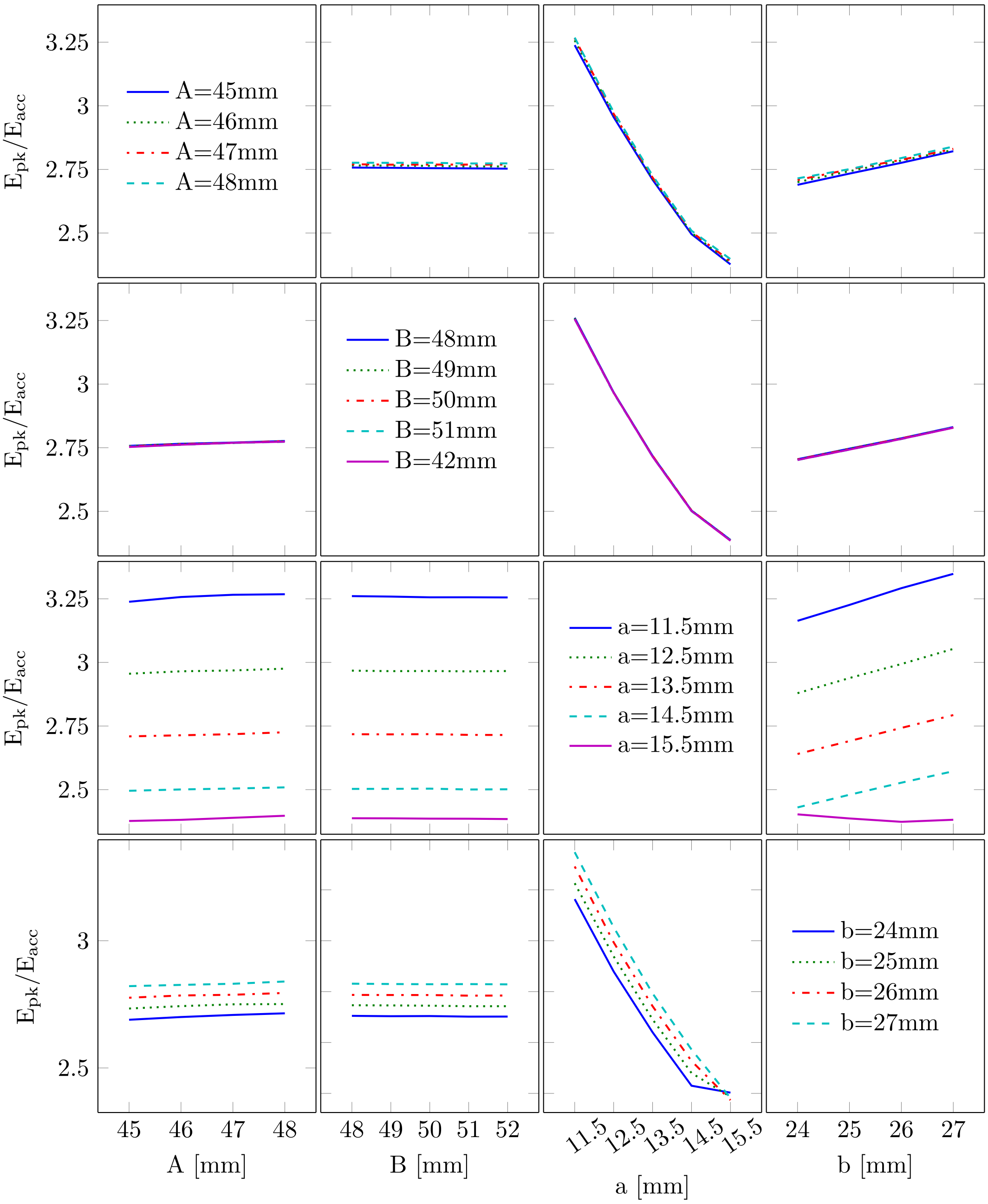

Figure 18: Interaction plot, E_{pk}/E_{acc} over the geometric parameters for the inner cell design.

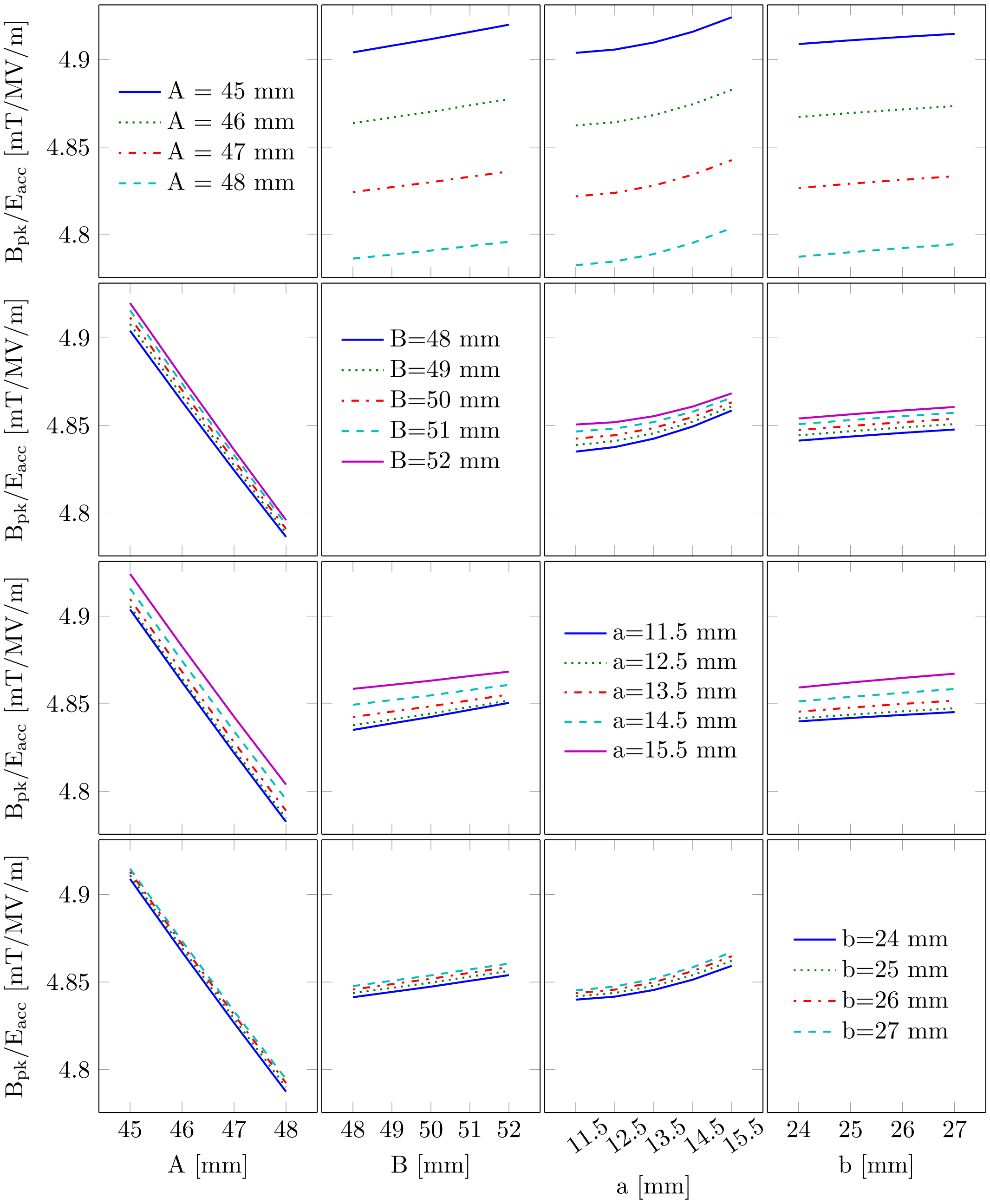

Figure 19: Interaction plot, B_{pk}/E_{acc} over the geometric parameters for the inner cell design.

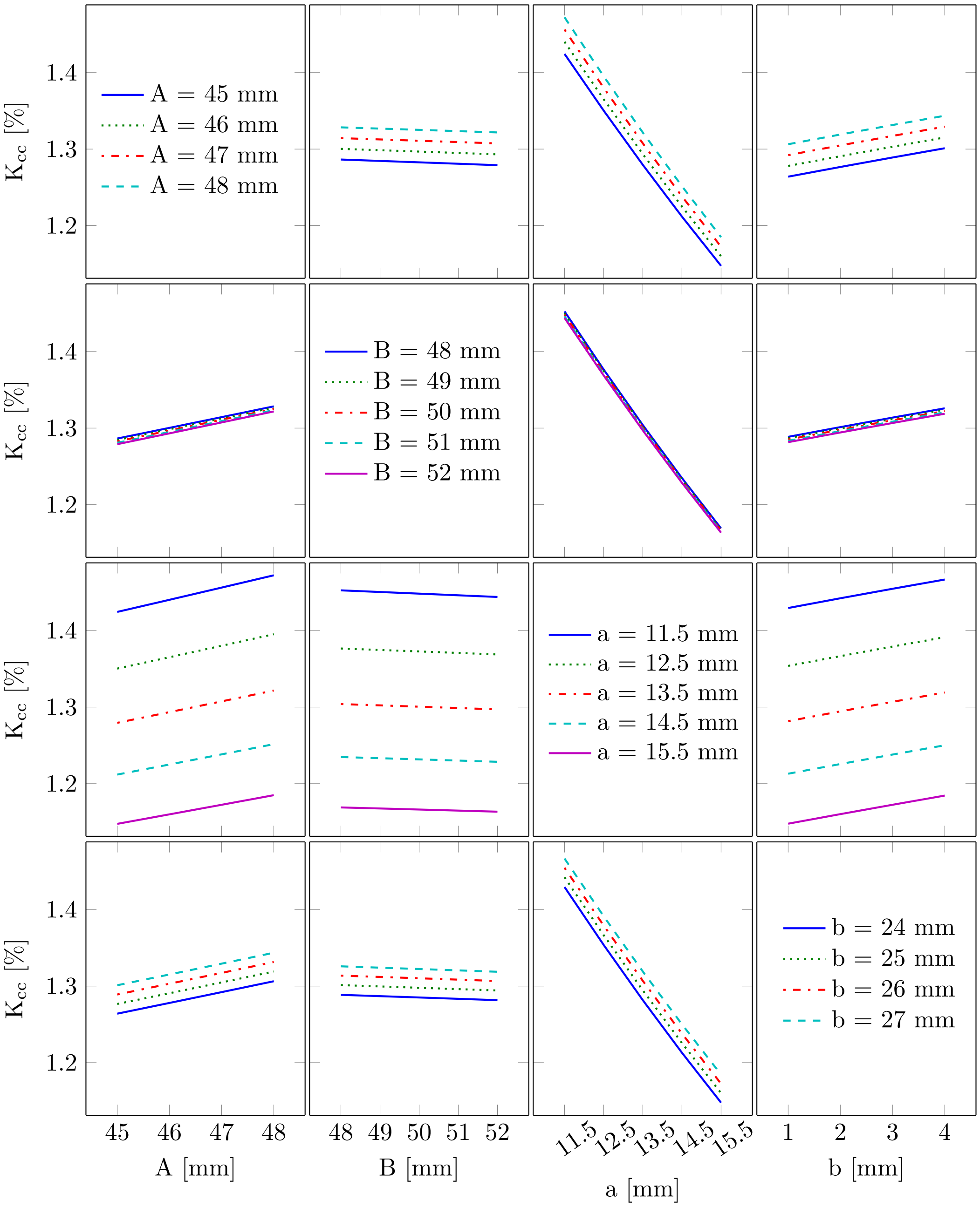

Figure 20: Interaction plot, K_{cc} over the geometric parameters for the inner cell design.

Table 3: Geometrical parameters and RF performances of the chosen inner cell

Parameter	Value
L [mm]	142.6
Riris [mm]	47
α [deg]	6.4
D [mm]	185.109
A [mm]	48
B [mm]	48
a [mm]	15.5
b [mm]	26
R/Q [Ω]	66.04
G [Ω]	195.9
E_{pk}/E_{acc}	2.385
B_{pk}/E_{acc} [mT/MV/m]	4.8
K_{acc} [%]	1.19

5.2 End Cell Design

In the end cell design phase, the end cells and the beam tube are designed, the end cell being made of half inner cell and half end cell (see figures 21 and 22). To simplify the overall design of the cavity, the cell radius D determined in the inner cell design phase is used also for the end cells. This makes it impossible to tune the cell by varying D. As an alternative, the parameter B has been chosen to tune the cells since it has the least influence on the RF performances.

The end cell is attached to the beam tube that has a radius of 68 mm which is substantially larger than the iris radius, R_{iris}. This is necessary in order to satisfy the requirement on the Q_{ext}. In fact, a large beam tube improves the coupling between the accelerating mode and the power coupler but decreases the accelerating field, the R/Q and thus the other RF performances of the end cells. The end cell can limit the performances of the whole cavity. The present design features two identical end cells, that is, both the end cells are the same despite the fact that the power coupler is only on one side of the cavity. It is often convenient to use different end cells in order to steer the frequencies of the higher-order-modes to a less dangerous part of the spectrum, far from the beam line harmonics. Moreover, to mitigate the effect of the lower performances of the end cells, one of them can be designed with a beam pipe that has, for example, the same size of the inner cell iris aperture, which tends to align the performances of the end cell with the inner cells.

To compensate for the lower end cell performances, a slight shortening of the end cup has been applied, in fact the end cup has a length of $L/2 = 137.6/2 = 68.8$ mm. This allows a slight decrease of the electric and magnetic peak fields, as shown in figure 23. As for the inner cell, after a broad exploration of the parameter space, the analysis is focused over a small section summarized in table 4.

As for the inner cell case, the parameters A and a are the most important. Notice the tradeoff between the electric and magnetic peak fields involving the parameter a (cfr figures 26 and 27). A high value of a leads to a lower electric peak field but a higher magnetic peak field.

Figures 28 to 31 are the interaciton plots of the end cells. We observe that

- contrary to the inner cell case a larger value of a leads to a lower R/Q, see fig 28.
- The nonlinear behavior of $\mathrm{E_{pk}/E_{acc}}$ versus a is present also in the end cell case, see fig. 30.

Table 5 summarizes the geometrical parameters of the chosen end cell and its RF perfomances.

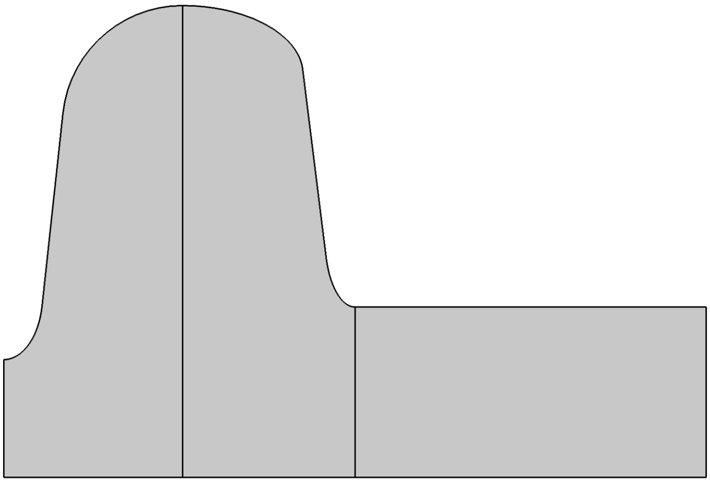

Figure 21: 2D model of the end cell made of half an inner cell cup and half an end cell cup.

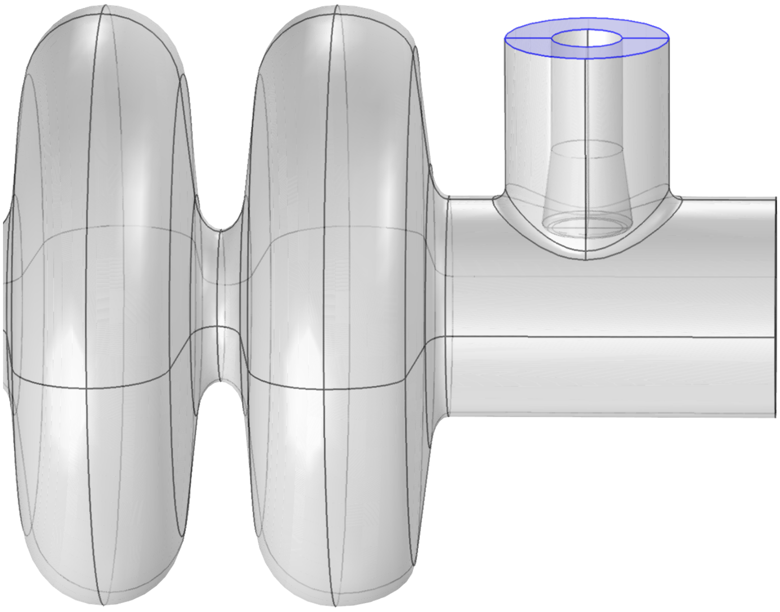

Figure 22: 3D model of the end cell with coaxial power coupler.

Table 4: Parametric sweep for the end cell design with $D = 185.109$ mm.

Geometric Parameter [mm]	start [mm]	stop [mm]	# steps
A	48	52	5
a	9	13	4
b	24	27	4

Table 5: Geometrical parameters and RF performances of the chosen end cell

Parameter	Value
L [mm]	137.2
Riris [mm]	68
α [deg]	7.4
D [mm]	185.109
A [mm]	48
B [mm]	27.29
a [mm]	12
b [mm]	27
R/Q [Ω]	57.89
G [Ω]	200.37
E_{pk}/E_{acc}	2.433
B_{pk}/E_{acc} [mT/MV/m]	4.97

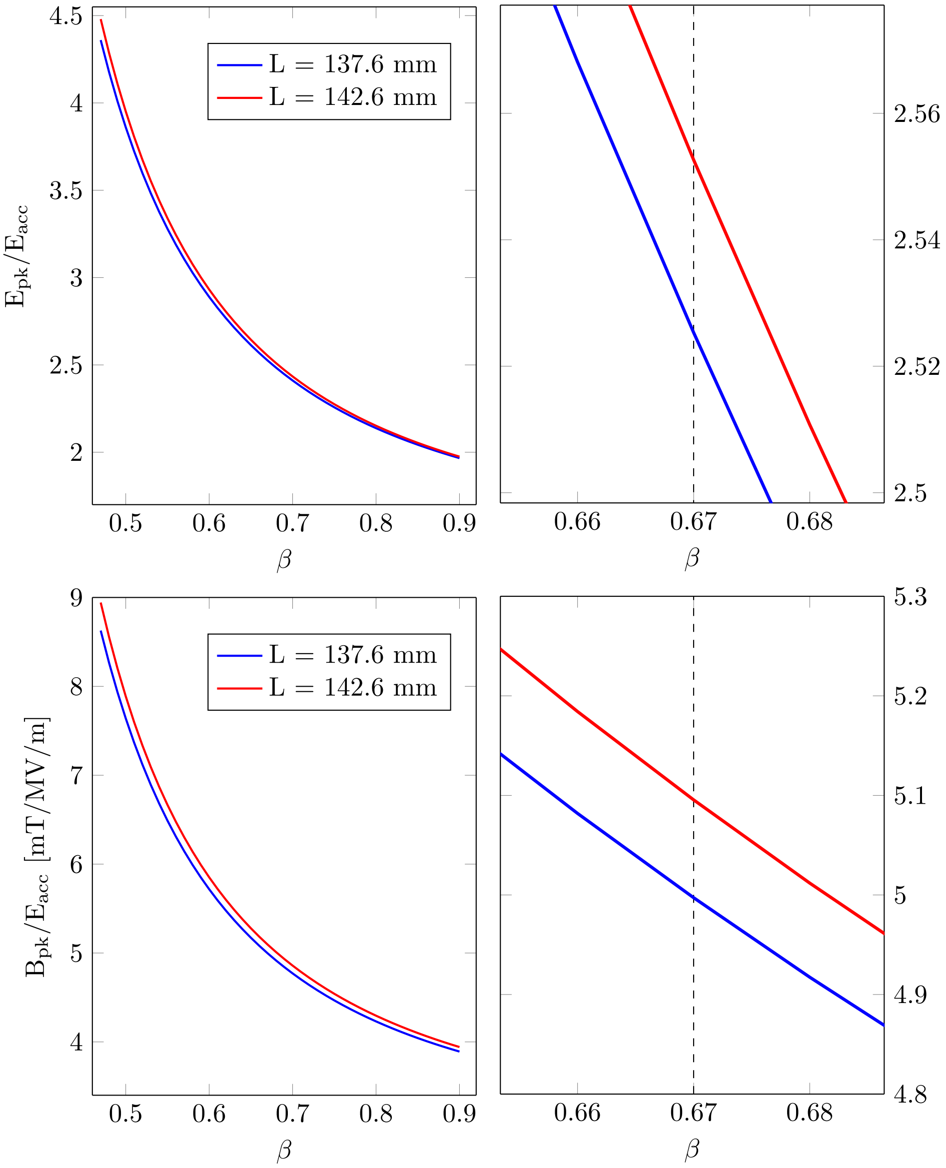

Figure 23: Normalized Peak Fields for the same end cell with different lengths of the end cup. On the right the zoomed in versions of the plots around $\beta = 0.67$ shows the slight improvement on the peak fields when the end cup is shortened.

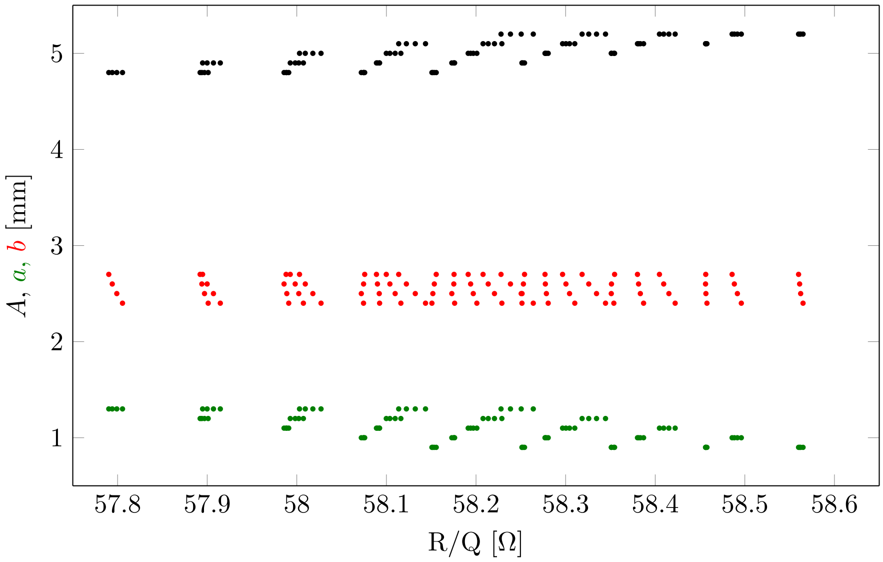

Figure 24: R/Q as function of the geometric parameters A, a and b.

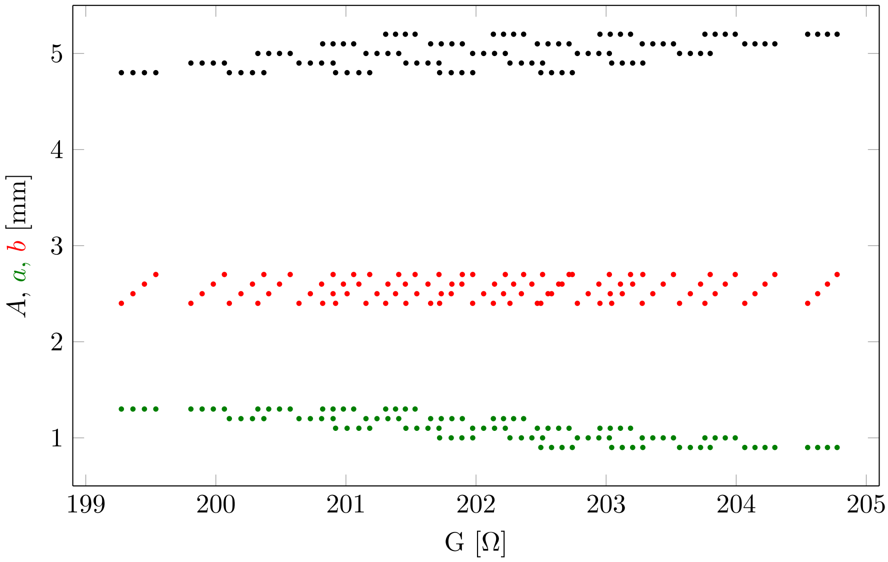

Figure 25: G as function of the geometric parameters A, a and b.

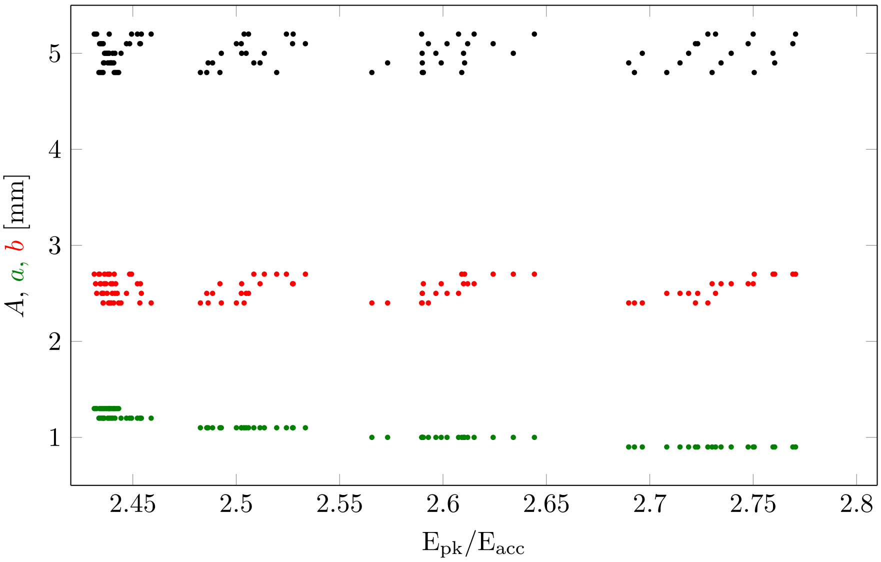

Figure 26: $\mathrm{E_{pk}/E_{acc}}$ as function of the geometric parameters A, a and b.

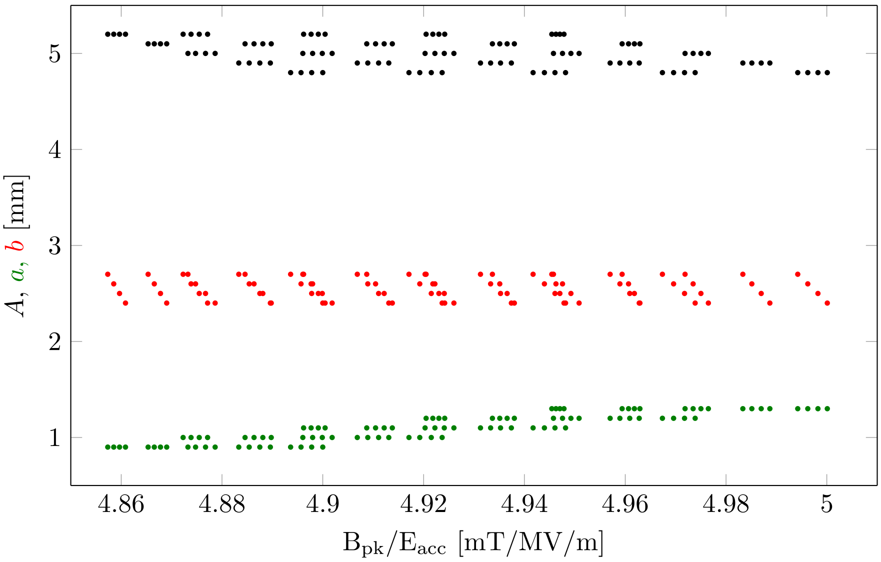

Figure 27: $\mathrm{B_{pk}/E_{acc}}$ as function of the geometric parameters A, a and b.

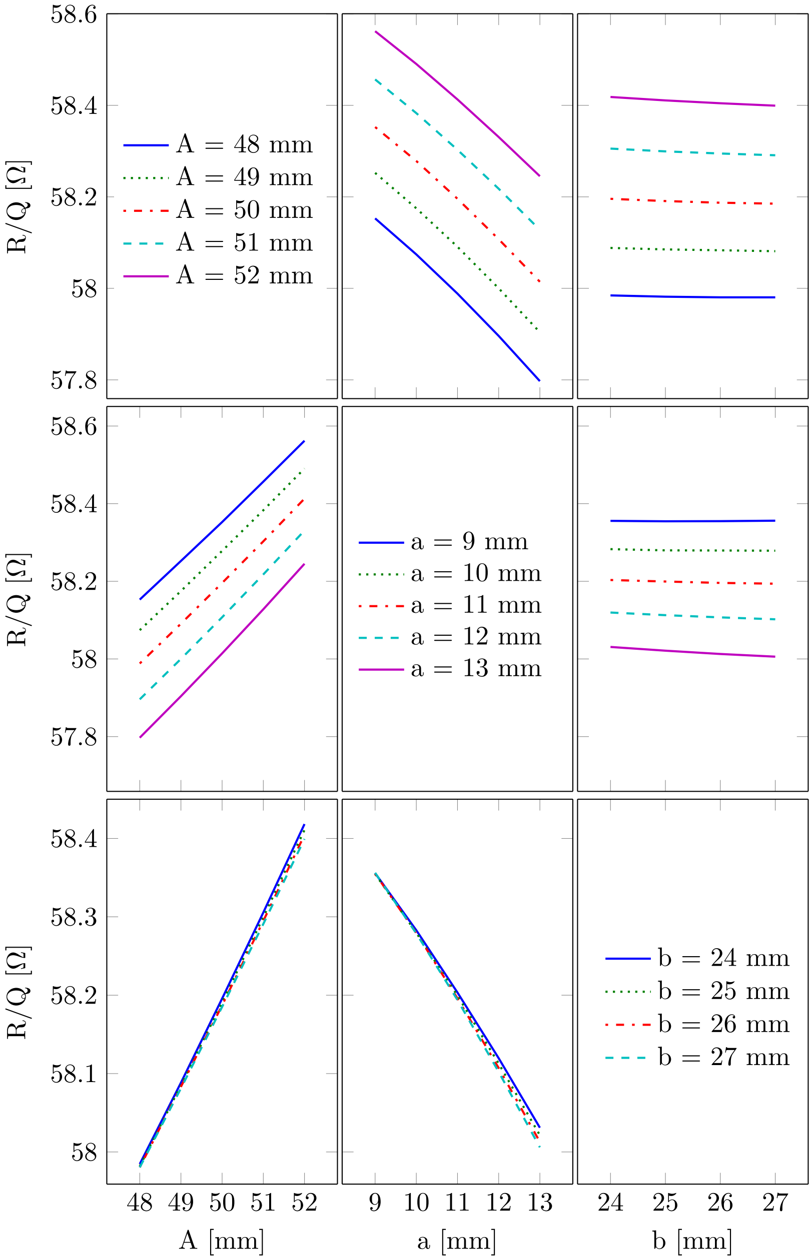

Figure 28: Interaction plot, R/Q over the geometric parameters for the end cell design.

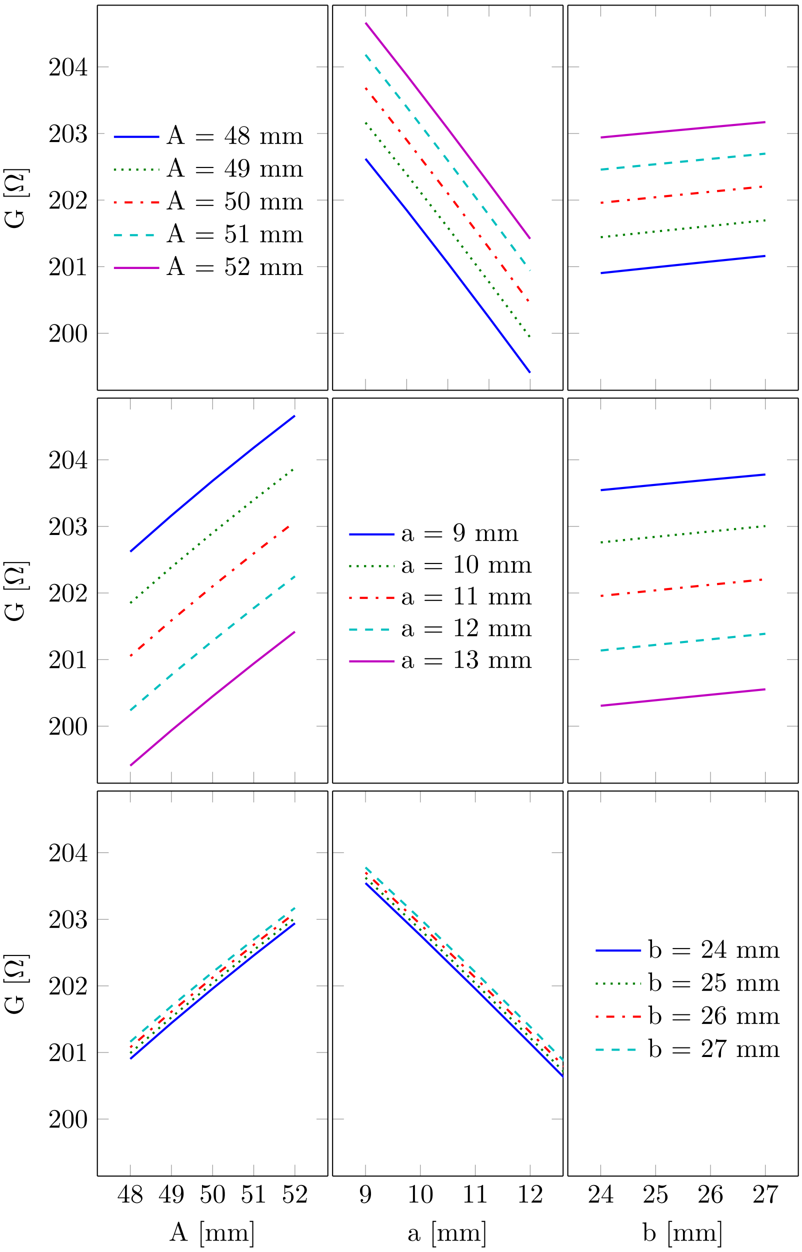

Figure 29: Interaction plot, G over the geometric parameters for the end cell design.

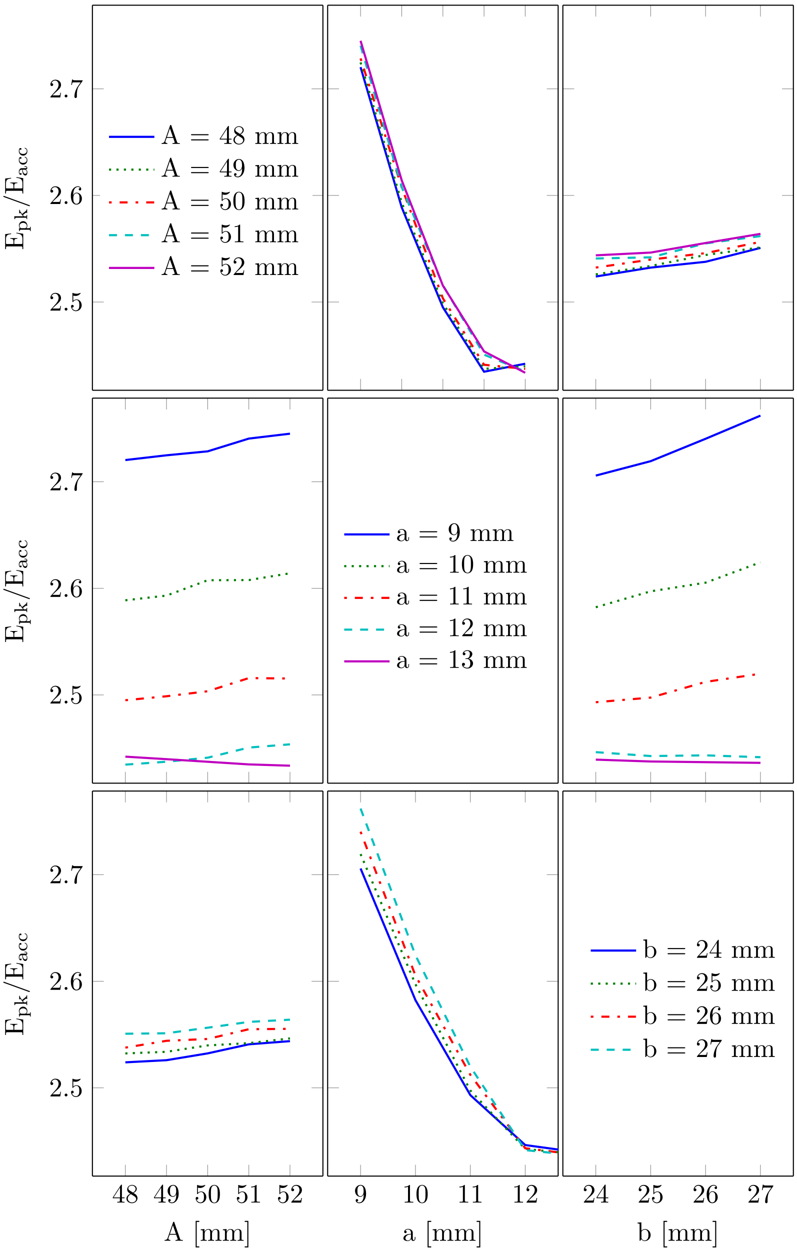

Figure 30: Interaction plot, E_{pk}/E_{acc} over the geometric parameters for the end cell design.

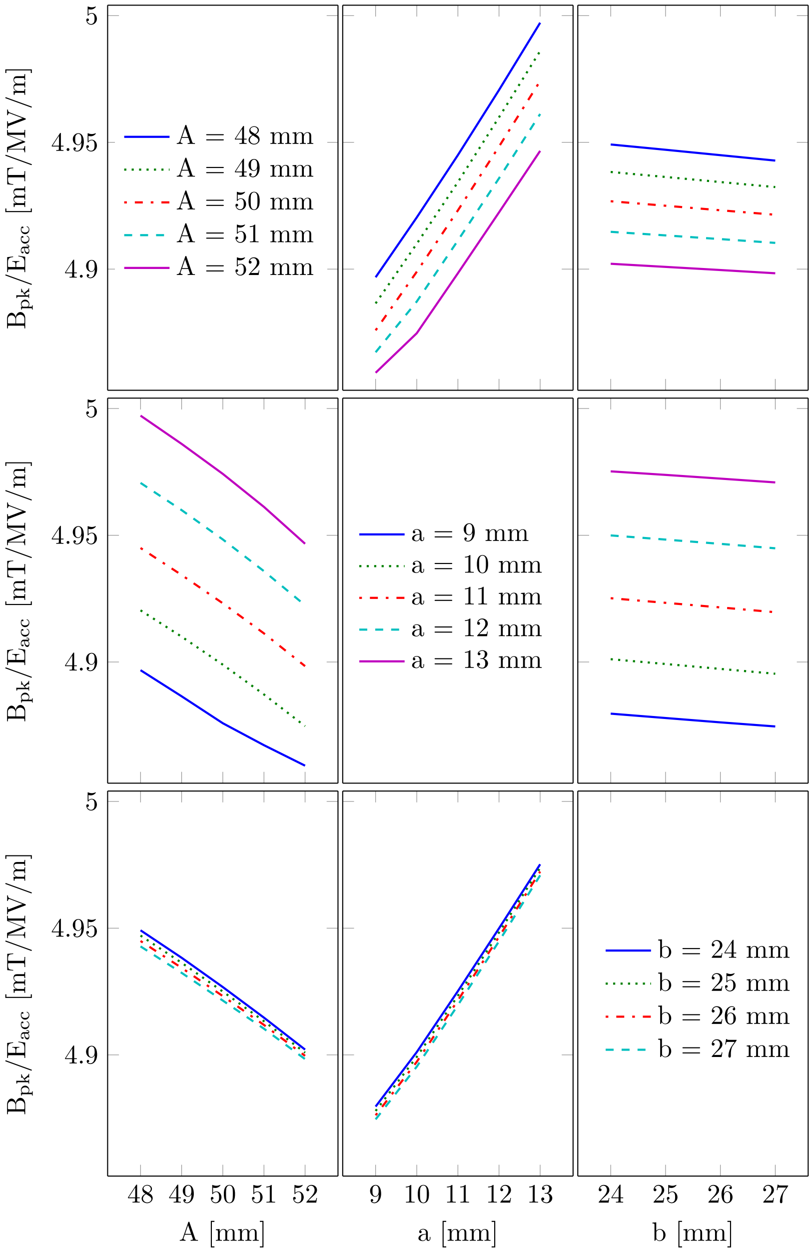

Figure 31: Interaction plot, B_{pk}/E_{acc} over the geometric parameters for the end cell design.

5.3 Coupler and External Quality Factor

In this section a preliminary study on the cavity coupling is presented. The main quantity used to quantify the coupling between an external circuit and the cavity is the *external quality factor*. The external quality factor is an important parameter since it determines how much of the power sent through the coupler is effectively used to generate an accelerating field. Its definition is the following:

$$Q_{ext} = \frac{\omega U}{P_{ext}} = \frac{\omega U}{\frac{1}{2}\int\limits_{\Sigma}(\boldsymbol{E} \times \boldsymbol{H}^*) \times \hat{\boldsymbol{n}}\, dS} \tag{12}$$

where, P_{ext} is the power flowing through the coupler port of cross section Σ and normal $\hat{\boldsymbol{n}}$ external to the cavity, ω is the mode considered and U its energy as defined in 3.

The geometry of the coupler is in figure 32 and it has been designed at the CEA laboratories, in Saclay, Paris. The quantity to be optimized is the antenna penetration p, while the parameter L_c is kept equal to 35 mm in order to have the best coupling possible leaving enough space for the helium vessel to be installed. When $p = 0$ the antenna does not protrude into the beam pipe and the antenna tip is at 68 mm from the symmetry axis. A plot of the results is in figure 33. In order to have an external quality factor that satisfies the specification, the antenna penetration p has to be set between 6mm to 10 mm.

5.4 The Complete Cavity

In this section the results concerning the complete six-cell cavity are summarized. All the main RF parameters are calculated for the accelerating mode, and are reported in table 6. Moreover figure 35 represents the R/Q of the fundamental passband modes as function of the normalized velocity β.

The beam passing through the cavity excites a large number of modes. The oscillations of such modes can grow strong enough to deteriorate the dynamics of the beam. To make sure that none of the higher-order-modes is a threat, it is necessary to verify that none of them resonates at a frequency close to one of the harmonics of the beam line frequency (352.21 MHz). Figure 34 and table 7 report the frequencies and R/Q's of the monopolar modes up to 3 GHz. None of the higher order modes is closer than 5 MHz to any of the harmonics of the beam line frequency. A more detailed study of the effect of the higher-order-modes and their power dissipation is deferred to paper III.

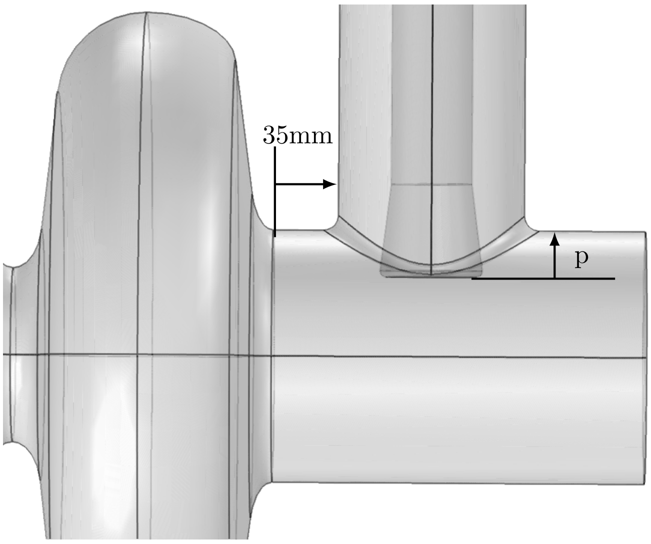

Figure 32: Coaxial coupler used in the simulations

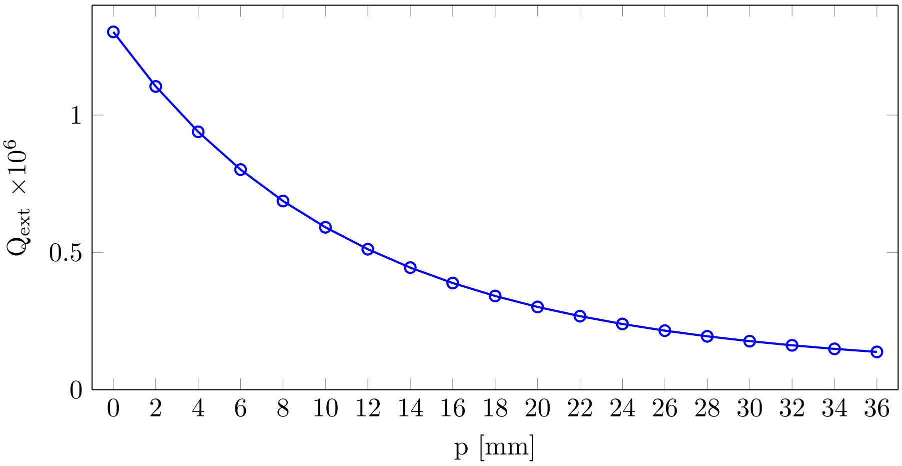

Figure 33: Variation of Q_{ext} against the antenna penetration.

Table 6: RF parameters of the six-cell cavity

Parameter	Value	
Frequency [MHz]	704.424	
G [Ω]	197.4	
Field Flattness [%]	99	
K_{cc} [%]	1.21	
	@ $\beta_{opt} = 0.705$	@$\beta_g = 0.67$
R/Q [Ω]	397.74	367.22
E_{pk}/E_{acc}	2.35	2.45
B_{pk}/E_{acc} [mT/MV/m]	4.78	4.98

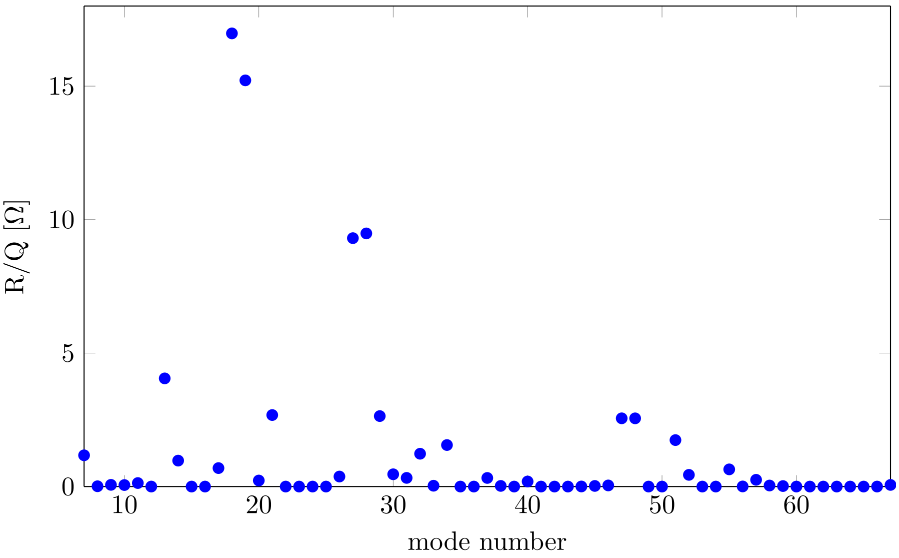

Figure 34: R/Q of the monopolar modes below 3 GHz.

Table 7: Frequencies and R/Q's of the monopolar modes below 3 GHz.

Frequency [MHz]	R/Q @β_g [Ω]	Frequency [MHz]	R/Q @β_g [Ω]
696.651	0.036	2271.087	$1.906\cdot10^{-15}$
698.232	0.364	2271.087	$1.097\cdot10^{-13}$
700.347	0.244	2281.829	0.323
702.411	1.211	2319.606	0.025
703.889	0.434	2326.480	$1.379\cdot10^{-12}$
704.423	3672210	2328.594	0.190
1515.651	1.171	2328.609	$1.509\cdot10^{-12}$
1517.186	0.012	2331.268	$7.329\cdot10^{-12}$
1524.349	0.065	2333.443	$1.004\cdot10^{-13}$
1534.232	0.057	2342.743	$3.59\cdot010^{-3}$
1544.856	0.132	2354.492	$2.357\cdot10^{-2}$
1553.281	$6.729\cdot10^{-4}$	2361.884	$4.22\cdot10^{-2}$
1681.031	4.052	2463.292	2.556
1681.050	0.972	2463.292	2.555
1695.762	$1.891\cdot10^{-13}$	2675.873	$4.302\cdot10^{-13}$
1695.761	$2.369\cdot10^{-12}$	2675.873	$4.899\cdot10^{-13}$
1727.305	0.692	2786.846	1.741
1731.288	16.975	2786.953	0.439
1732.029	15.215	2797.279	$2.903\cdot10^{-12}$
1736.092	0.226	2797.279	$5.510\cdot10^{-12}$
1743.905	2.679	2808.352	0.644
1744.021	$7.897\cdot10^{-13}$	2812.680	$4.674\cdot10^{-3}$
1744.705	$2.149\cdot10^{-14}$	2825.224	0.253
1745.545	$4.390\cdot10^{-14}$	2847.158	$3.910\cdot10^{-2}$
1746.222	$4.203\cdot10^{-12}$	2872.516	$1.917\cdot10^{-2}$
1749.588	0.375	2888.448	$1.025\cdot10^{-13}$
1949.356	9.305	2897.655	$2.618\cdot10^{-13}$
1949.356	9.482	2909.788	$7.238\cdot10^{-13}$
2183.424	2.640	2920.880	$8.751\cdot10^{-17}$
2183.537	0.460	2955.779	$1.411\cdot10^{-12}$
2218.565	0.325	2955.859	$2.273\cdot10^{-12}$
2235.026	1.230	2995.211	$5.385\cdot10^{-4}$
2253.930	0.031	3001.075	$6.185\cdot10^{-2}$
2269.807	1.555		

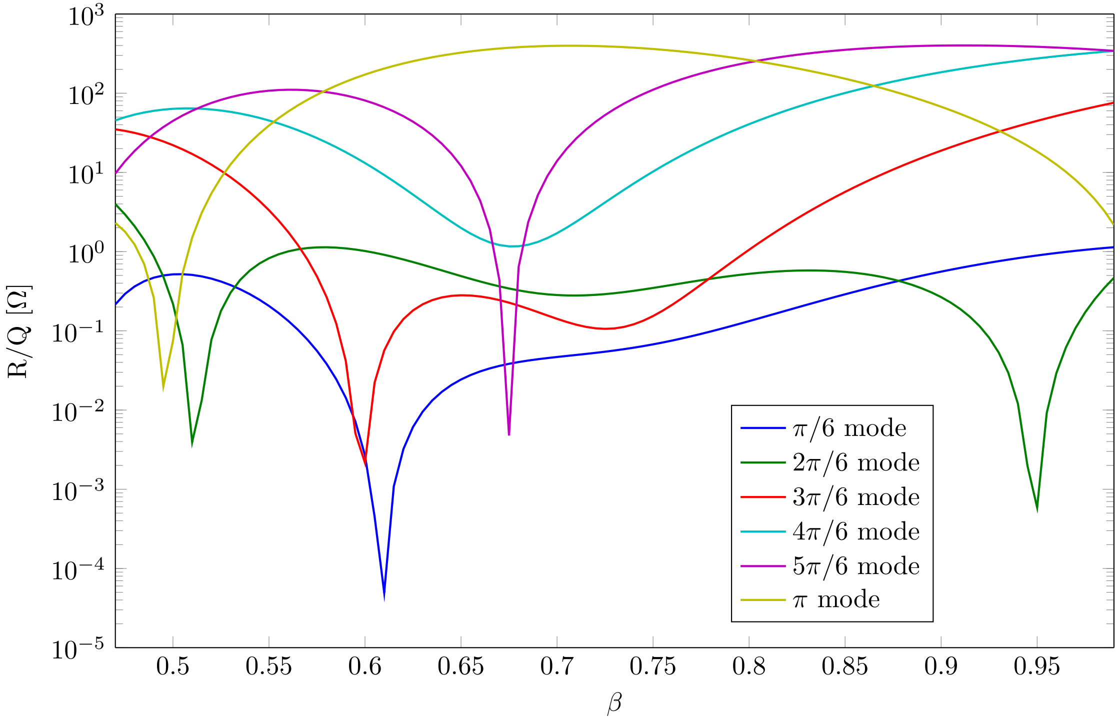

Figure 35: R/Q plotted agains the normalized velocity β for the normal modes of the fundamental passband.

6 Test Results

The cavity (see fig. 37) was tested at the CEA laboratories in Saclay, in July 2016. The measurement process involves cooling down the cavity at cryogenic temperatures ($\approx 2^\circ$ Kelvin) in a vertical cryostat. Two antennas are attached to the beam pipes of the cavity, the first antenna is used to send power into the cavity while the second is passive and it's used to measure the transmitted power. The difference between the measured incident, reflected and transmitted powers is the average power stored in the cavity. Using the factor R/Q calculated with the simulator it is then possible to calculate the accelerating gradient E_{acc}.

The cavity presented in this thesis has passed the test reaching an accelerating gradient of 17 MV/m with an intrinsic quality factor of $\approx$ 7.5e9, see fig. 36, both quantities are beyond the specifications. Tests on the second cavity prototype will be done in January 2017 on a cavity dressed with the helium vessel.

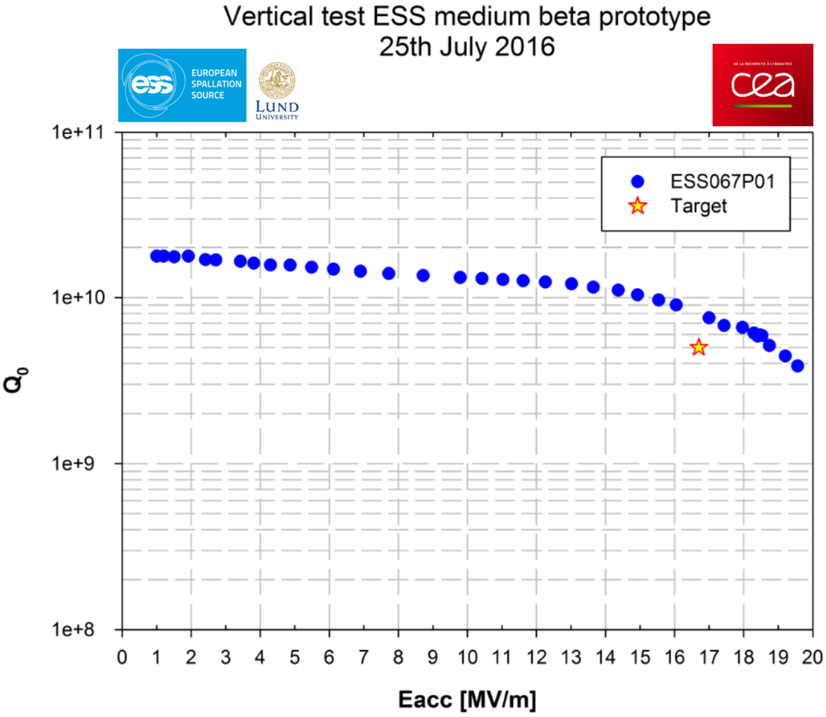

Figure 36: Test results for the first medium-β prototype obtained at the CEA research center in Saclay, Paris.

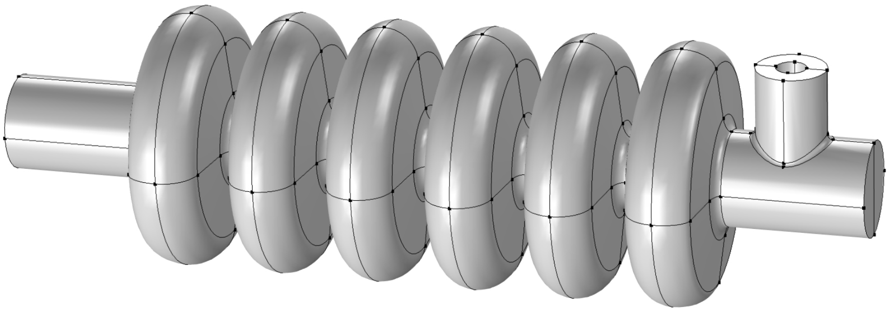

Figure 37: 3D model of the full cavity.

References

[1] S. Peggs editor, “Conceptual Design Report, ESS-2012-01.

[2] M. Checchin et al., “Quench-Induced Degradation of the Quality Factor in Superconducting Resonators”, Phys. Rev. Appl. 5, 044019 (2016).

[3] R. Parodi, “Multipacting”, arXiv:1112.2176, https://arxiv.org/ftp/arxiv/papers/1112/1112.2176.pdf

[4] T. P. Wangler, “RF Linear Accelerators”, John Wiley & Sons.

[5] M. Eshraqi, “Beam Physics Design of the Optimus+ SC Linac”, ESS AD Technical Note ESS/AD/0050, Nov 2013.

[6] M. Eshraqi and I. Bustinduy and L. Celona and M. Comunian and H. Danared and R. De Prisco and F. Grespan and M. Lindroos and D. McGinnis and R. Miyamoto and S. P. Møller and M. Munoz and A. Ponton and E. Sargsyan and H. D. Thomsen, “The ESS Linac”, IPAC2014 Proc., Dresden, Germany 2014.

[7] G. Devanz, J. Plouin, “Conceptual Design of the Beta = 0.86 Cavities for the Superconducting Linac of ESS”.

[8] S. Posen, M. Liepe, “Mechanical Optimization of Superconducting Cavities in Continuous Wave Operation”, Phys. Rev. ST, 15, 2012.

[9] B. Aune et al, “Superconducting TESLA Cavities”, Phys. Rev. ST, Acc. and Beams., Vol **3**, 092001 (2000).

[10] D. A. Edwards ed. “TESLA Test Facility Linac Design Report”, DESY, Ch. 4, 1995.

[11] A. Bosotti et al., “Characterization of an Elliptical Low Beta multicell Structure for Pulsed Operation”, Proc. of the 12th International Workshop on RF Superconductivity, Cornell University, Ithaca, NY, USA.

Paper II

Mechanical Design

Gabriele Costanza.

Abstract

In this paper the mechanical design and its influence on the electromagnetic properties of the medium-β cavity for the ESS is presented. First a description of the relevant mechanical parameters is given along with the description of the quality factors that are necessary to assess the quality of the cavity design. The simulations show that the thickness of the cavity walls is the main factor in determining the mechanical performances of the cavity while the stiffening rings contribute to a lower degree. In the end the results are presented.

Mechanical Design

1 Introduction

In this paper we focus on the mechanical study of the cavity. Before giving the main results an explaination is necessary regarding the quantities of interest and the simulations set up.

Elliptical cavities are made of thin Niobium sheets welded together and, for this reason, they are susceptible to geometric deformations. There are several causes of detuning, such as vibrations and radiation pressure. Considering that the intrinsic quality factor of the accelerating mode is in the range of $\approx 10^9$ even a small deformation can shift the frequency of the modes significantly. If the cavity is driven off resonance, more power would be needed to maintain the nominal accelerating gradient in the cavity and a considerable ammount of power would be refrlected back to the RF system. The mechanical parameters that we consider are:

- Lorentz Force Detuning.
- Tuning Sensitibity.
- Cavity Stiffness.
- Pressure Sensitivity.
- Maximum von Mises Stress.

We now give an explaination of the mentioned quantities.

1.1 Lorentz Force Detuning

The RF power injected in the cavity exerts a pressure on the cavity walls that leads to the so called *Lorentz Force Detuning* (LFD) [5]. Consider the magnetic field strength of the accelerating mode (fig. 1) and the surface currents (red arrows in 1). The magnetic field and the surface current are strongest in the dome region. The magnetic field is directed along the azimuthal direction while the surface currents are tangential to the cavity surface. An application of the Lorentz force formula produces a force on the cavity walls directed towards the outside of the cavity. Moreover, in the iris region, the electromagnetic field interacts with the induced surface charges, producing a force directed towards the inside of the cavity. The resulting force on the cavity surface is in figure 2.

Together the electric $\boldsymbol{E}$ and the magentic field $\boldsymbol{H}$ produce a *radiation pressure*, which is defined as

$$P_{rad} = \frac{1}{4}\left(\mu_0|\boldsymbol{H}|^2 - \epsilon_0|\boldsymbol{E}|^2\right), \tag{1}$$

where, $\boldsymbol{E}$ and $\boldsymbol{H}$ are the electric and magnetic field on the walls of the cavity. The cells are deformed by the radiation pressure producing a frequency shift which can be evaluated to a first approximation with Slater's formula [1]:

$$\frac{\delta f}{f} \approx \frac{1}{4U}\int\limits_{\Omega}\left(\mu_0|\boldsymbol{E}|^2 - \epsilon_0|\boldsymbol{H}|^2\right)\, d\Omega. \tag{2}$$

where, Ω is the difference in the volume between the deformed cavity, with the radiation pressure, and the unperturbed cavity, without radiation pressure. The quantity U is the time average of the electromagnetic energy stored in the unperturbed cavity. An increase of volume in a part of the cavity where the magnetic energy density of the accelerating mode is larger than the electric energy density leads to a decrease of the frequency of the accelerating mode.

If the deformation is small, it is possible to link the steady state frequency shift of the resonant frequency and the accelerating field with K_L, the *Lorentz Force Detuning Coefficient* (LFD), with the relation:

$$\Delta f = -K_L E_{acc}^2 \Rightarrow |K_L| = \frac{\Delta f}{E_{acc}^2} \qquad \left[\frac{Hz}{(MV/m)^2}\right]. \tag{3}$$

The LFD coefficient depends on the stiffness of the cavity, on its tuning sensitivity, on the accelerating field and on the external stiffening mechanism. In our case the accelerating field is calculated only at $\beta = \beta_g = 0.67$. With a coupled mechanical-EM simulation it is possible to evaluate the frequency of the accelerating mode before and after applying the radiation pressure, so that Δf can be evaluated. In order to stiffen the cavity, stiffening rings between the cells are added and the deformation of the cell can be partially compensated. Consider that

- the stiffening rings are placed close to the iris rather than close to the dome in order not to stiffen the cavity to the point where it would be too hard to tune.
- The effect of the rings is evident in the iris region and less important in the dome region. The thickness of the metal has a primary importance on the mechanical characteristics of the cavity.
- The LFD is strongly dependent on the external stiffness. It is necessary to consider a realistic scenario where the boundaries of the cavity are not

fixed but are connected to the Helium vessel and the tuner which have both ha finite stiffness and allow the cavity to shrink in the longitudinal direction.

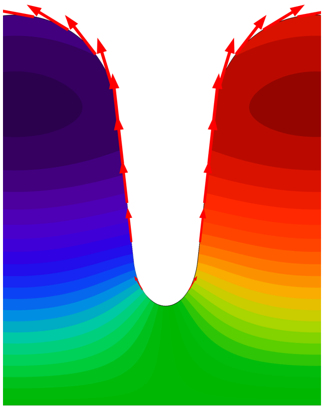

Figure 1: Contour plot of the magnetic field of the accelerating mode and arrow plot of the surface current density. Green represents zero intensity.

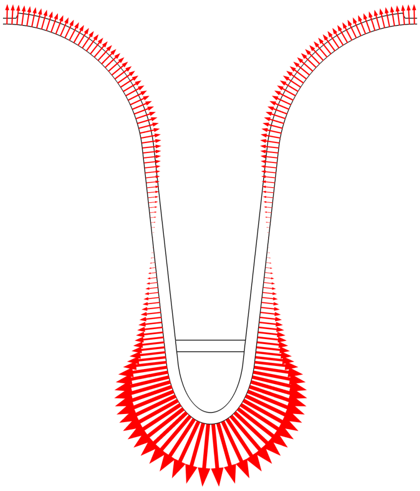

Figure 2: Stress on the cavity walls produced by the electromagnetic pressure.

1.2 Stiffness

The stiffness of the cavity is simulated by applying a total force of 1 KN on one end of the cavity, the other being fixed, and by measuring the displacement. In figure 3 we can see an example of such a simulation, where the displacement has been enhanced to ease its visualization. The stiffness is evaluated in kN/mm.

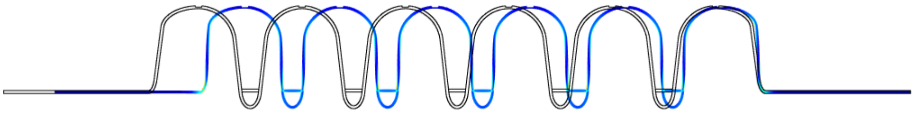

Figure 3: Von Mises Stress due to the application of 1 KN on the left flange of the cavity. The right flange is fixed.

1.3 Tuning Sensitivity

The tuning sensitivity, df/dz, is measured in KHz/mm and it is calculated by imposing a displacement of 1 mm and by measuring the frequency shift of the accelerating mode. The tuning sensitivity quantifies the frequency variation of the fundamental mode when an external force acts on one of its ends.

1.4 Pressure Sensitivity

One of the main sources of detuning is the variation of the Helium pressure surrounding the cavity [6]. It is then necessary to evaluate the pressure sensitivity, K_p [Hz/mbar]. In this simulation a uniform pressure of 1 mbar is applied to the external boundary. One of the cavity ends is connected to a mechanical ground while the other is left free. Otherwise both the cavity ends can be grounded.

1.5 Von Mises Stress

Another important quantity is the maximum *Von Mises Stress*. It allows to judge if the stress in the cavity walls are greater than the yield strength. If that happens, the cavity would deform plastically, and as a consequence, the frequency of the resonant modes would change. Moreover the cavity has to pass safety tests to be certified and used in an accelerator, in such tests a fixed pressure is applied to the cavity which does not have to reach its yield strength.

1.6 Cavity Detuning

It has been mentioned in the previous sections that the cavity is subject to deformations which produce a frequency shift of the resonant frequency of the modes. Frequency detuning is originated by different sources, such as, LFD, microphonic detuning, that is the effect of mechanical vibrations generated by devices surrounding the cavity, and pressure fluctuations of the Helium surrounding the cavity [7]. A detuned cavity requires more power to mantain the specified accelerating gradient, thus increasing the operating costs of the accelerator, and decreasing its efficiency.

For both the LFD and the pressure variation it is possible to devise a model that quantifies the frequency detuning considering the superposition of two effects [8, 9]:

1. the modification of the shape of the cavity when its ends are fixed, that is, when a fixed constraint boundary condition is imposed at the ends of the cavity. Under this constraint the shape of the cell changes, producing a frequency detuning, moreover, the cavity exerts a reaction force F_∞ on the constraint because it tends to contract.

2. The shortening of the cavity.

The resulting model allows the calculation of the frequency detuning of the accelerating mode in both the static LFD and Pressure variation cases, considering the stiffness of tank and the tuner ($\mathrm{K_{ext}}$) and the stiffness of the cavity ($\mathrm{K_{cav}}$):

$$\Delta f = \Delta f_\infty + \frac{df}{dz}\frac{F_{reac.\infty}}{K_{ext}+K_{cav}},$$

where the ∞ subscript refers to quantities calculated with fixed ends, F_{reac} is the reaction force which can be calculated with a simulator and df/dz is the tuning sensitivity. We then have for the LFD coefficient and the pressure sensitivity:

$$K_L(K_{ext}) = K_{L\infty} + \frac{df}{dz}\frac{F_{reac.L\infty}}{K_{ext}+K_{cav}}, \tag{4}$$

$$K_p(K_{ext}) = K_{p\infty} + \frac{df}{dz}\frac{F_{reac.p\infty}}{K_{ext}+K_{cav}}, \tag{5}$$

where $F_{reac.L\infty} \propto E_{acc}^2$. An example of the use of (4) and (5) is in figures 10 and 11 respectively.

1.7 Helium Vessel

The cavity has to pass pressure tests in order to verify that the cavity meets minimum safety criteria and to make sure that the cavity would not deform plastically. The Maximum Von Mises Stress has been simulated both with and without the Helium vessel. To be able to make the computations with an axially symmetric 2D geometry, a simplified vessel has been modeled (fig. 4). The 2D model is substantially simpler than the real Helium vessel but in absence of the real model it allows to estimate the mechanical performances of the dressed cavity. There are two diagonal elements connecting the flanges at the end of the beam pipes, to the top of the vessel. The left element at the tuner side, is assumed to be infinitely stiff, since during the pressure tests the tuner is removed and substituted with a fixed element. The stiffness of the right element is chosen in order to obtain a stiffness of 75 KN/mm between points A and B (see fig. 5), that is, point A is connected to a mechanical ground and 1 KN is applied to the flange at the point B. The stiffness of the cavity is calculated and the Young's modulus of the element is changed in order to obtain the specified stiffness. The Helium vessel is made of Titanium and has the following parameters:

- Young's modulus = 105 GPa,
- Poissons's ratio = 0.33,
- Density = 4940 Kg/m^3.

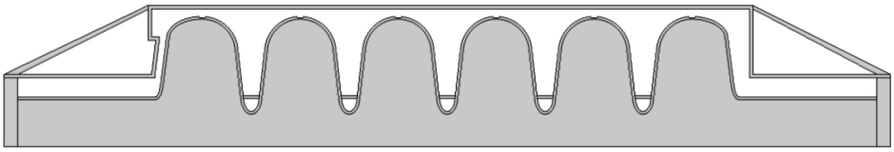

Figure 4: Cavity dressed with the Helium vessel.

Once the stiffness of the dressed cavity is set to 75 KN/mm, a pressure is applied to the external surface of the cavity (in blue in fig. 6) and the Maximum Von Mises stress is obtained with a simulator.

2 Results

The results of the mechanical simulations are summarized in table 1. Moreover the LFD coefficient and the pressure sensitivity as function of the external

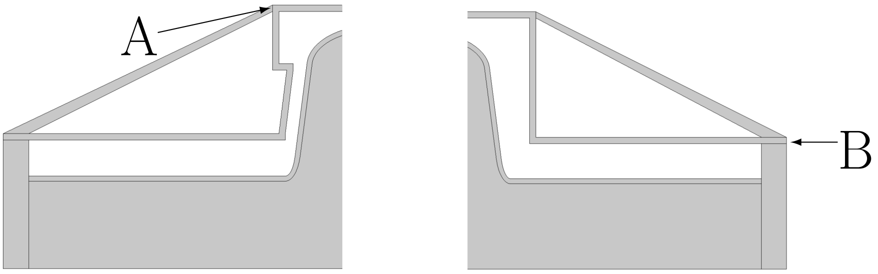

Figure 5: Cavity dressed with the Helium vessel.

stiffness are plotted in figures 10 and 11. The following quantities have been calculated:

- Tuning Sensitivity
- Cavity Stiffness
- Lorentz Force Detuning with fixed ends, free ends and with vessel and tuner
- Pressure Sensitivity with fixed and free ends
- Maximum Von Mises Stress with and without vessel and tuner

In the case of “free ends” simulations, one of the flanges is not constrained, while the other is connected to a mechanical ground. In the “fixed ends” case, both flanges are connected to a mechanical ground.

The thickness of the metal used for the cavity model is of 4 mm which is the thickness of choice, but also cavities 3.8 mm and 4.2 mm have been simulated. The simulations show that the thickness of the metal is of primary importance in determining the mechanical performances of the cavity, while the stiffening ring radius has a smaller influence. The Niobium used in the simulations has the following characteristics:

- Young’s modulus = 105E9 Pa,
- Poissons’s ratio = 0.4,
- Density = 8570 Kg/m^3.

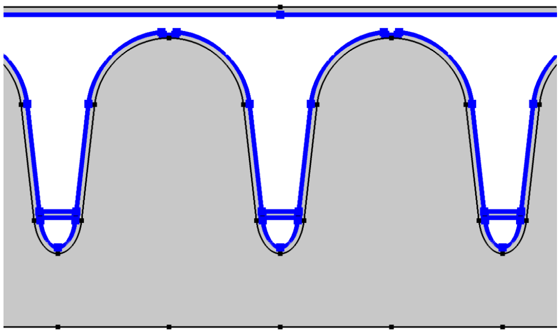

Figure 6: In the Maximum Von Mises Stress the pressure is applied on the surface marked in blue.

The Von Mises Stress is calculated both with a simplified model of the Helium vessel with stiffness equal to 75 KN/mm, and without vessel. Since the stiffness of the tuner is of about 30 KN/mm, the total stiffness of the tank plus the tuner is about 21 KN/mm. The results of the Maximum Von Mises Stress simulations (in table 1) are followed by a letter, *b*, *i* or *d* and they indicate where the maximum of the stress occurs.

- *b.* The maximum of the stress is on the external surface, between the beam tube and the last cell, fig. 7.
- *i.* The maximum of the stress is on the internal surface close to the stiffening rings, fig. 9.
- *d.* The maximum of the stress is on the internal surface at the dome, fig 9. A radius of the stiffening rings of 70 mm has been chosen to compromise between the LFD, which grows with by increasing the stiffening ring radius, and the cavity stiffness.

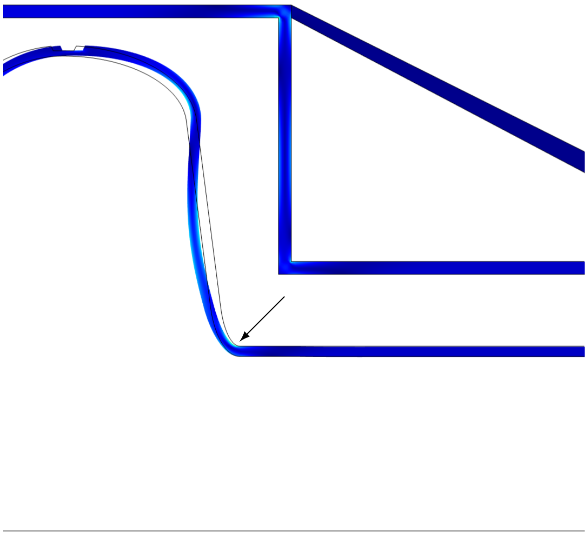

Figure 7: Position of the maximum of the Von Mises Stress on the external surface.

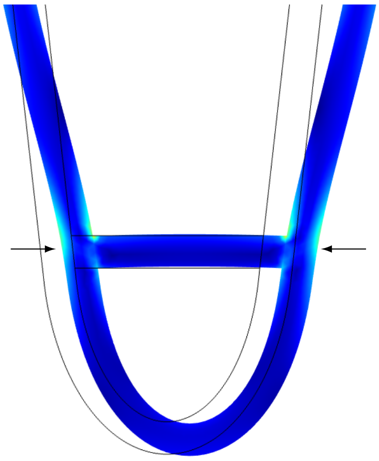

Figure 8: Position of the maximum of the Von Mises Stress on the internal surface at the stiffening ring position.

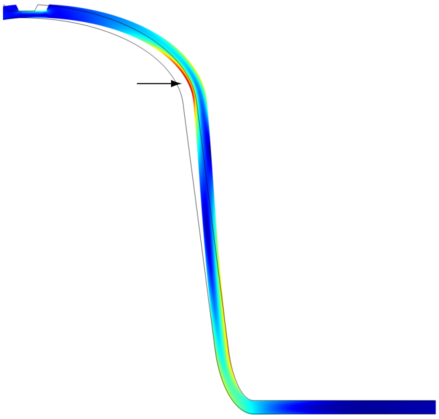

Figure 9: Position of the maximum of the Von Mises Stress on the internal surface on the dome.

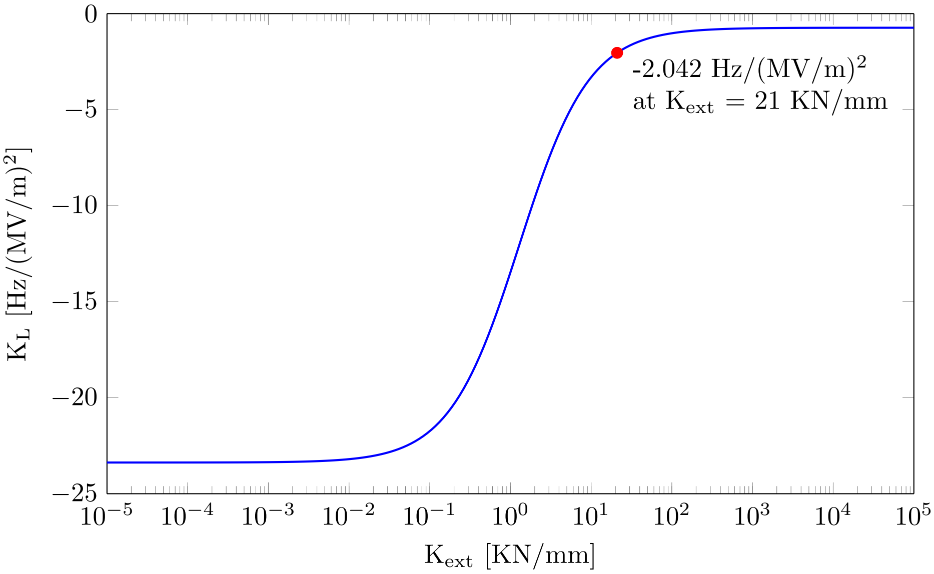

Figure 10: Variation of the LFD coefficient with respect to the external stiffness.

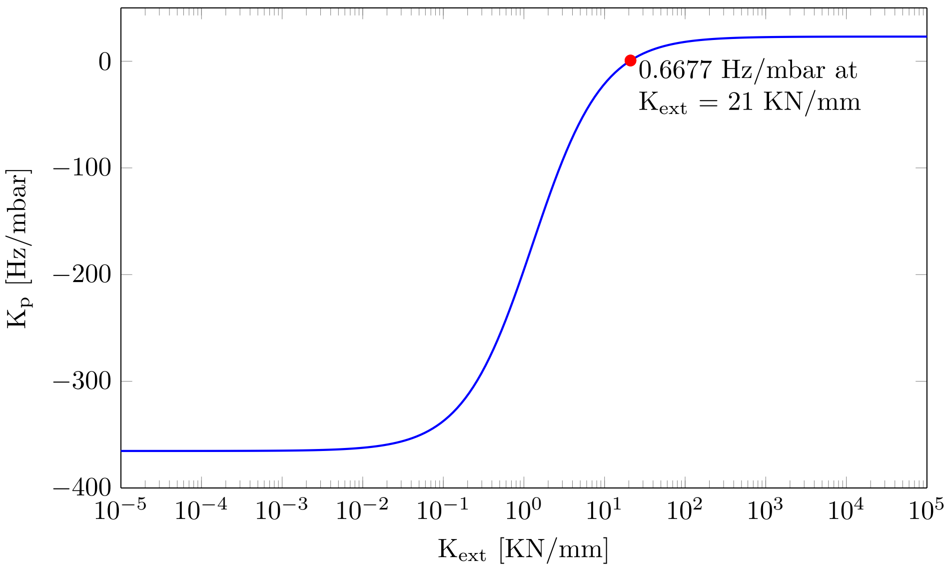

Figure 11: Variation of the pressure sensitivity coefficient with respect to the external stiffness.

Mechanical Quantity	Stiffening Rings Radius [mm]			
	68	70	72	74
Tuning Sensitivity, $\Delta f/\Delta z$ [KHz/mm]	213.98	214.83	215.53	216.1
Cavity Stiffness, $\mathrm{K_{cav}}$ [KN/mm]	1.25	1.286	1.32	1.36
LFD @ $\beta = 0.67$, fixed ends, $\mathrm{K_L}$ [Hz/(MV/m)^2]	-0.734	-0.735	-0.745	-0.756
LFD @ $\beta = 0.67$, fixed ends, $\mathrm{K_L}$ [Hz/(MV/m)^2]	-23.69	-23.35	-22.87	-22.34
LFD @ $\beta = 0.67$, fixed ends @ $\mathrm{K_{ext}}$=21 KN/mm [Hz/(MV/m)^2]	-2.03	-2.04	-2.06	-2.07
Pressure Sensitivity, fixed ends, $\mathrm{K_p}$ [Hz/mbar]	21.77	23.08	24.00	24.54
Pressure Sensitivity, free end, $\mathrm{K_p}$ [Hz/mbar]	-365.05	364.94	-364.31	262.15
Max. Von Mises Stress @ 1 bar, fixed ends [MPa]	19.8b/20i	20.5b/19i	21b/18.2i	21.6b/17.1i
Max. Von Mises Stress @ 1 bar, free end, pressure on flange [MPa]	35d/24.7b	35.1d/24.6b	35d/24.8b	35d/24.8b
Max. Von Mises Stress @ 1 bar, free ends [MPa]	33.6d/23.2b	33.6d/23.4b	33.6d/23.2b	33.6d/23.2b
Max. Von Mises Stress @ 1.5 bar, free ends [MPa]	52.6d/37.2b	52.6d/37.3b	52.6d/37.2b	52.6d/37.1b
Max. Von Mises Stress @ 1.5 bar, fixed ends, helium vessel $\mathrm{K_{ext}}$ 75 KN/mm [MPa]	30.1i/29.7b	28.8i/30.6b	27.3i/31.4b	26i/32.4b
Max. Von Mises Stress @ 1.5 bar, free ends, helium vessel $\mathrm{K_{ext}}$ 75 KN/mm [MPa]	30i/29.7b	29.4i/31.4b	27.3i/31.4b	26i/32.4b

Table 1: Results of the mechanical simulations.

References

[1] J. C. Slater, “Microwave Electronics”, D. Van Nostrand (1959).

[2] S. Peggs et al., “ESS Techincal Design Report”, 2013.

[3] M. Eshraqi, “Beam Physics Design of the Optimus+ SC Linac”, ESS AD Technical Note ESS/AD/0050, Nov 2013.

[4] M. Eshraqi and I. Bustinduy and L. Celona and M. Comunian and H. Danared and R. De Prisco and F. Grespan and M. Lindroos and D. McGinnis and R. Miyamoto and S. P. Møller and M. Munoz and A. Ponton and E. Sargsyan and H. D. Thomsen, “The ESS Linac”, IPAC2014 Proc., Dresden, Germany 2014.

[5] G. Devanz, J. Plouin, “Conceptual Design of the Beta = 0.86 Cavities for the Superconducting Linac of ESS”.

[6] S. Posen, M. Liepe, “Mechanical Optimization of Superconducting Cavities in Continuous Wave Operation”, Phys. Rev. ST, 15, 2012.

[7] B. Aune et al, “Superconducting TESLA Cavities”, Phys. Rev. ST, Acc. and Beams., Vol **3**, 092001 (2000).

[8] D. A. Edwards ed. “TESLA Test Facility Linac Design Report”, DESY, Ch. 4, 1995.

[9] A. Bosotti et al., “Characterization of an Elliptical Low Beta multicell Structure for Pulsed Operation”.

Paper III

Remarks on the Mathematical Solution of the Hollow Cavity Eigenvalue Problem

Abstract

We discuss the eigenvalue problem for a perfectly conducting hollow cavity under a strict functional analytic point of view. We make use of a variant of the classical spectral theorem for compact selfadjoint operators and we pay extra attention on the null space of the Maxwell operator. We also discuss the corresponding inhomogeneous problem, where currents are present, even when they may depend on the fields.

Remarks on the Mathematical Solution of the Hollow Cavity Eigenvalue Problem

G. Costanza[1] **and A. D. Ioannidis**[2]

[1]Lund University, Sweden
[2]Linnæus University, Sweden

Abstract— We discuss the eigenvalue problem for a perfectly conducting hollow cavity under a strict functional analytic point of view. We make use of a variant of the classical spectral theorem for compact selfadjoint operators and we pay extra attention on the null space of the Maxwell operator. We also discuss the corresponding inhomogeneous problem, where currents are present, even when they may depend on the fields.

1. NOTATION AND PRELIMINARIES

The purpose of this paper is to provide an efficient mathematical framework for the classical eigenvalue problem for a hollow, perfectly conducting cavity. Our motivation emerged from the recent research concerning the ESS accelerator project [3, 7]. The study of the cavity problem has been started as early as the 40's [10] and reconsidered many times then, even since our days, see [1, 4, 6, 11]. Nevertheless, there are still some dark points concerning mainly existence issues and the so-called completeness of the modes. Our aim is to give a clear and concise picture of the relevant mathematical problem and suggest the appropriate tools for its solution, in the spirit of [2].

The notation we use in this paper is as follows. Let $(X, \langle\cdot,\cdot\rangle)$ be an infinite dimensional separable Hilbert space. For a set $U \subset X$, we denote by $\bar{U}$ the closure, by $U^\perp$ the orthogonal complement and by $[U]$ the linear span of U; the closed linear span is then $\overline{[U]}$. $B(X)$ stands for the Banach algebra of bounded operators in X and $K(X)$ for the ideal of compact operators. Given a linear operator $A : X \supset \mathfrak{D}(A) \to X$, we denote by $\mathfrak{R}(A)$ the range and by $\ker A$ the null space (kernel) of A. The graph norm on $\mathfrak{D}(A)$ is defined as

$$\|x\|_A := \sqrt{\|x\|^2 + \|Ax\|^2}.$$

When equipped with the graph norm, $\mathfrak{D}(A)$ will be denoted as $[\mathfrak{D}(A)]$ (not to be confused with the linear span notation). A^* stands for the adjoint operator. A is called selfadjoint if $A^* = A$, skew-adjoint if $A^* = -A$.

The resolvent set $\rho(A)$ consists of all $\lambda \in \mathbb{C}$ for which $R(\lambda; A) := (\lambda I - A)^{-1} \in B(X)$ (resolvent operator). If $\rho(A) \neq \emptyset$ then A is closed. The spectrum of A is defined as $\sigma(A) := \mathbb{C} \backslash \rho(A)$. $\lambda \in \sigma(A)$ is called an eigenvalue if $\lambda I - A$ is not injective and non-zero vectors of $\ker(\lambda I - A)$ are called the coresponding eigenvectors. The set of eigenvalues is denoted by $\sigma_p(A)$ (point spectrum).

Proposition 1. *The following are equivalent:*
a) $R(\lambda; A) \in K(X)$ *for some* $\lambda \in \rho(A)$.
b) $R(\lambda; A) \in K(X)$ *for all* $\lambda \in \rho(A)$.
c) $\rho(A) \neq \emptyset$ *and* $[\mathfrak{D}(A)] \hookrightarrow X$ *with a compact injection.*

Definition 1. If A satisfies one of the equivalent conditions of Prop. 1, then it is called a discrete operator.

The following theorem provides the main tool for our exposition.

Proposition 2 (Spectral Theorem)**.** *Let* A *be a discrete selfadjoint operator. Then* $\sigma(A) = \sigma_p(A)$ *and* $\sigma_p(A)$ *is a finite or unbounded countable set without accumulation point. The corresponding eigenspaces are finite dimensional and mutually orthogonal. Eigenvalues of* A *can be set as an increasing sequence* (λ_n)*, diverging at infinity if countable. Each non-zero eigenvalue is counted according to its multlipicity and the sequence* (e_n) *of the corresponding eigenvectors can be chosen as an orthonormal sequence. Moreover,*
a) (e_n) *is an orthonormal basis for* $\overline{\mathfrak{R}(A)}$ *and* $X = \ker A \oplus \overline{[(e_n)]}$.
b) $Ax = \sum_n \lambda_n \langle x, e_n\rangle e_n$, $x \in \mathfrak{D}(A)$.

2. THE MAXWELL SYSTEM

As it is well known, every electromagnetic phenomenon is specified by four vector quantities: the electric field $\mathbf{E}$, the magnetic field $\mathbf{H}$, the electric flux density $\mathbf{D}$ and the magnetic flux density $\mathbf{B}$, in the presence of electric and magnetic currents $\mathbf{J}_e$, $\mathbf{J}_m$, respectively. These quantities are considered as time–dependent vector fields on a domain $\Omega \subset \mathbb{R}^3$, so they are functions of the spatial variable $\mathbf{r} \in \Omega$ and the time variable $t \in \mathbb{R}$. All these fields are connected via the Maxwell system

$$\frac{\partial \mathbf{D}}{\partial t} = \mathrm{curl}\mathbf{H} - \mathbf{J}_e, \;\; \frac{\partial \mathbf{B}}{\partial t} = -\mathrm{curl}\mathbf{E} + \mathbf{J}_m. \tag{1}$$

We have allowed existence of magnetic currents here because apertures in a cavity can be modeled this way [9]. The above are supplemented with the two Gauss laws

$$\mathrm{div}\,\mathbf{D} = \rho_e\,, \;\; \mathrm{div}\,\mathbf{B} = \rho_m. \tag{2}$$

where ρ_e, ρ_m are the densities of the electric and magnetic charge, respectively. Currents and charges are not independent and obey equation of continuity

$$\frac{\partial \rho_e}{\partial t} + \mathrm{div}\,\mathbf{J}_e = 0\,, \;\; \frac{\partial \rho_m}{\partial t} + \mathrm{div}\,\mathbf{J}_m = 0. \tag{3}$$

If one accepts (3) as part of the modeling, (2) become redundant and can be absorbed in the initial conditions.

We now assume that the domain Ω is a hollow cavity, *i.e.*, a vacuous bounded domain:

$$\mathbf{D} = \varepsilon_0 \mathbf{E}\,, \;\; \mathbf{B} = \mu_0 \mathbf{H}. \tag{4}$$

Without loss of generality, we assume $\varepsilon_0 = \mu_0 = 1$. We further assume that the boundary Γ of Ω is Lipschitz and therefore an exterior normal $\hat{\mathbf{n}}$ is almost everywhere defined on it and the perfect electric conductor boundary condition applies

$$\hat{\mathbf{n}} \times \mathbf{E} = \mathbf{0}, \text{ on } \Gamma. \tag{5}$$

The above implies that $\hat{\mathbf{n}} \cdot \mathbf{H} = 0$ on Γ. In the six vector notation, (1) are read as follows:

$$\frac{\partial}{\partial t}\begin{pmatrix}\mathbf{E}\\ \mathbf{H}\end{pmatrix} = \begin{bmatrix}0 & \mathrm{curl}\\ -\mathrm{curl} & 0\end{bmatrix}\begin{pmatrix}\mathbf{E}\\ \mathbf{H}\end{pmatrix} + \begin{pmatrix}-\mathbf{J}_e\\ \mathbf{J}_m\end{pmatrix}. \tag{6}$$

To make things more precise, let us denote by $\mathbf{e} := (\mathbf{E}, \mathbf{H})^{\mathbf{T}}$ the electromagnetic (EM) field, by $\mathbf{j} := (-\mathbf{J}_e, \mathbf{J}_m)^T$ the EM current and by

$$\mathcal{M} := \begin{bmatrix}0 & \mathrm{curl}\\ -\mathrm{curl} & 0\end{bmatrix} \tag{7}$$

the formal Maxwell operator. Then (6) is written

$$\frac{\partial \mathbf{e}}{\partial t} = \mathcal{M}\mathbf{e} + \mathbf{j}. \tag{8}$$

We now assume $\mathbf{j} = \mathbf{0}$ (homogeneous problem) and apply a separation-of-variables technique, that is, we ask for a solution of (8) of the form $\mathbf{e}(\mathbf{r}, t) := \mathsf{e}(\mathbf{r})T(t)$ and thus

$$\mathcal{M}\mathsf{e} = \frac{T'(t)}{T(t)}\mathsf{e}.$$

Since the left hand side depends only on $\mathbf{r}$, the ratio $T'(t)/T(t)$ has to be a constant, say λ, and we conclude to the formal eigenvalue problem

$$\mathcal{M}\mathsf{e} = \lambda\mathsf{e}, \tag{9}$$

with $\mathsf{e} := (\mathbf{E}, \mathbf{H})^T$. Note that although we use the same notation, $\mathbf{E}$, $\mathbf{H}$ now do not depend on time. We also have apparently $T(t) = \mathrm{e}^{\lambda t}$.

3. REALIZATION OF THE EIGENVALUE PROBLEM

The exposition and notation in this section follows [2, 8]. Due to energy considerations, the fields $\mathbf{E}$, $\mathbf{H}$ are taken to be square integrable, *i.e.*, they are vectors of the Hilbert space $L^2(\Omega;\mathbb{C}^3)$ with inner product

$$\langle \mathbf{U},\mathbf{V}\rangle_0 := \int_\Omega \mathbf{U}(\mathbf{r})\cdot\mathbf{V}(\mathbf{r})\,d\mathbf{r}.$$

The *curl* operator is naturally realized in its weak sense in $L^2(\Omega;\mathbb{C}^3)$. More precisely, let $\mathbf{U}\in L^2(\Omega;\mathbb{C}^3)$. We say that $\mathbf{V}$ is the (weak) rotation of $\mathbf{U}$, and we write $\mathbf{V} = \mathrm{curl}\mathbf{U}$, if

$$\langle \mathbf{V},\boldsymbol{\phi}\rangle_0 = \langle \mathbf{U},\mathrm{curl}\boldsymbol{\phi}\rangle_0$$

for every test function $\boldsymbol{\phi}\in C_0^\infty(\Omega;\mathbb{C}^3)$. The maximal domain of definition of *curl* in $\mathcal{X}$ is then the Sobolev space $H(\mathrm{curl};\Omega)$ and is a densely defined closed operator. Moreover, *curl* can be realized as a maximal selfadjoint operator in the subspace $H_0(\mathrm{curl};\Omega)$, which contains exactly the fields that satisfy (5) in a weak sense. The null spaces of these operators are denoted by $H(\mathrm{curl}0;\Omega)$, $H_0(\mathit{curl};\Omega)$ respectively. Analogous definitions apply for the weak divergence operator *div*, see the aforementioned references for details.

Consequently, the EM field e is a vector of the product Hilbert space $\mathcal{X} := L^2(\Omega;\mathbb{C}^3)\times L^2(\Omega;\mathbb{C}^3)$ with inner product, for $\mathsf{u} := (\mathbf{U}_1,\mathbf{U}_2)^T$, $\mathsf{v} := (\mathbf{V}_1,\mathbf{V}_2)^T$,

$$\langle \mathsf{u},\mathsf{v}\rangle := \langle \mathbf{U}_1,\mathbf{V}_1\rangle_0 + \langle \mathbf{U}_2,\mathbf{V}_2\rangle_0 .$$

The Maxwell operator is realized in a weak sense in $\mathcal{X}$ as follows: $\mathsf{e}\in\mathcal{X}$ is in the domain $\mathfrak{D}(\mathcal{M})$ of $\mathcal{M}$ if there exists a (unique) vector $\mathsf{u}\in\mathcal{X}$ such that

$$\left\langle \mathsf{u},(\boldsymbol{\phi}_1,\boldsymbol{\phi}_2)^T\right\rangle = \left\langle \mathsf{e},(-\mathrm{curl}\boldsymbol{\phi}_2,\ \mathrm{curl}\boldsymbol{\phi}_1)^T\right\rangle, \tag{10}$$

for every choice of test functions $\boldsymbol{\phi}_1$, $\boldsymbol{\phi}_2\in C_0^\infty(\Omega;\mathbb{C}^3)$. In this case, we set $\mathsf{u} := \mathcal{M}\mathsf{e}$. After this, problem (3) can be realized as an eigenvalue problem for such defined operator $\mathcal{M}$.

Proposition 3. *$\mathfrak{D}(\mathcal{M}) = H_0(\mathrm{curl};\Omega)\times H(\mathrm{curl};\Omega)$ and $\mathcal{M}$ is a densely defined, closed linear operator, represented by the operator matrix (7). Moreover, $\mathcal{M}$ is skew-adjoint, i.e., $\mathcal{M}^* = -\mathcal{M}$. Consequently, the spectrum of $\mathcal{M}$ is purely imaginary.*

That is to say, (3) has imaginary eigenvalues, if any. Following the usual practice, we let $\lambda := -\mathrm{i}\omega$, $\omega\in\mathbb{R}$, and the problem is rewritten as

$$\mathcal{Q}\mathsf{e} = \omega\mathsf{e}, \tag{$\star$}$$

where $\mathcal{Q} := \mathrm{i}\mathcal{M}$ is the selfadjoint Maxwell operator. So we are mainly interested in properties of operator $\mathcal{Q}$; in view of the above proposition, $\mathfrak{D}(\mathcal{Q}) = \mathfrak{D}(\mathcal{M})$ and $\mathcal{Q}$ is a selfadjoint operator with real spectrum.

Definition 2. Let (ω,e) be a non-trivial solution of ($\star$), *i.e.*, $\omega\in\mathbb{R}$ is an eigenvalue of $\mathcal{Q}$ with corresponding eigenvector e. ω is called an eigenfrequency of the cavity and e the corresponding mode.

Proposition 4. *The null space of $\mathcal{Q}$ is $\ker\mathcal{Q} = H_0(\mathrm{curl}\,0;\Omega)\times H(\mathrm{curl}\,0;\Omega)$. For the range $\mathfrak{R}(\mathcal{Q})$ of $\mathcal{Q}$, we have $\mathfrak{R}(\mathcal{Q})\subset H(\mathrm{div}\,0;\Omega)\times H_0(\mathrm{div}\,0;\Omega) := \mathcal{H}$.*

We now consider the restriction $\mathcal{Q}_\mathcal{H}$ of $\mathcal{Q}$ on $\mathcal{H}$, defined by $\mathfrak{D}(\mathcal{Q}_\mathcal{H}) = \mathfrak{D}(\mathcal{Q})\cap\mathcal{H}$ and $\mathcal{Q}_\mathcal{H}\mathsf{e} = \mathcal{Q}\mathsf{e}$. Incidentally, $\mathcal{Q}_\mathcal{H}$ coincides with the part of $\mathcal{Q}$ on $\mathcal{H}$.

Proposition 5. *$\mathcal{Q}_\mathcal{H}$ is selfadjoint and $[\mathfrak{D}(\mathcal{Q}_\mathcal{H})]$ is compactly injected into $\mathcal{H}$. Consequently, $\mathcal{Q}_\mathcal{H}$ is discrete and its spectrum is an unbounded sequence of real eigenvalues with no accumulation point. The corresponding eigenspaces are finite dimensional and mutually orthogonal.*

4. PROPERTIES OF EIGENFREQUENCIES AND MODES

Proposition 6. *Let* $\omega \neq 0$ *be an eigenvalue of* $\mathcal{Q}_{\mathcal{H}}$ *with corresponding eigenvector* $(\mathbf{E}, \mathbf{H})^{\mathbf{T}}$. *Then*
a) $\mathbf{E}$, $\mathbf{H}$ *satisfy the system*

$$\begin{cases} -\operatorname{curl}\mathbf{H} = i\omega\mathbf{E} \\ \quad \operatorname{curl}\mathbf{E} = i\omega\mathbf{H} \end{cases} \tag{11}$$

b) $\|\mathbf{E}\|_0 = \|\mathbf{H}\|_0$.
c) $-\omega$ *is an eigenvalue as well, with corresponding eigenvector* $(\mathbf{E}, -\mathbf{H})^{\mathbf{T}}$.

That is, the eigenvalues of $\mathcal{Q}_{\mathcal{H}}$ can be ordered as a bilateral sequence $(\omega_n)_{n\in\mathbb{Z}}$, with $\omega_n > 0$ for $n > 0$, $\omega_n < 0$ for $n < 0$, $\omega_0 = 0$ and $\omega_{-n} = -\omega_n$. For $n \neq 0$, we count each eigenvalue ω_n as many times as its multiplicity, so we can assume that to each ω_n there corresponds exactly one normalized eigenvector $\mathsf{e}_n^p := (\mathbf{E}_n^p, \mathbf{H}_n^p)^T$. The zero eigenvalue is counted once and we will discuss about it later. Namely, the eigenvalues are ordered as follows:

$$-\infty \leftarrow \ldots \leqslant \omega_{-n} \leqslant \ldots \leqslant \omega_{-1} < \omega_0 = 0 < \omega_1 \leqslant \ldots \leqslant \omega_n \leqslant \ldots \to \infty.$$

The sequence of eigenvectors (e_n) is assumed to be orthonormal.

Proposition 7. *Let* n, $m \in \mathbb{N}^*$, $\omega_n \neq \omega_m$. *Then* $\langle \mathbf{E}_n^p, \mathbf{E}_m^p \rangle_0 = \langle \mathbf{H}_n^p, \mathbf{H}_m^p \rangle_0 = 0$, i.e., *both* $(\mathbf{E}_n^p)_{\mathbf{n}\in\mathbb{N}^*}$, $(\mathbf{H}_n^p)_{\mathbf{n}\in\mathbb{N}^*}$ *define orthogonal sequences in* $L^2(\Omega;\mathbb{C}^3)$.

Proposition 8. $(\mathsf{e}_n^p)_{n\in\mathbb{Z}^*}$ *is an orthonormal basis for* $\overline{\mathfrak{R}(\mathcal{Q}_{\mathcal{H}})}$ *and we have the decomposition*

$$\mathcal{H} = \ker \mathcal{Q}_{\mathcal{H}} \oplus \overline{[\ldots, \mathsf{e}_{-n}^p, \ldots, \mathsf{e}_{-1}^p, \mathsf{e}_1^p, \ldots, \mathsf{e}_n^p, \ldots]}$$

The closed subspace $\ker \mathcal{Q}_{\mathcal{H}}$ *is finite dimensional. Moreover, for* $\mathsf{e} \in \mathfrak{D}(\mathcal{Q}_{\mathcal{H}})$,

$$\mathcal{Q}_{\mathcal{H}}\mathsf{e} = \sum_{n\in\mathbb{Z}^*} \omega_n \left\langle \mathsf{e}, \mathsf{e}_n^p \right\rangle \mathsf{e}_n^p.$$

For a detailed description of $\ker \mathcal{Q}_{\mathcal{H}}$ we refer to [2, 8]. Let N_0 be the dimension of $\ker \mathcal{Q}_{\mathcal{H}}$ (a number depending on the geometry of Ω) and consider an orthonormal basis $\{\mathsf{e}_1^0, \ldots, \mathsf{e}_{N_0}^0\}$ for $\ker \mathcal{Q}_{\mathcal{H}}$. Note that $\ker \mathcal{Q}_{\mathcal{H}}$ describes the source-free, static electromagnetism on Ω.

Proposition 9. $\{\mathsf{e}_1^0, \ldots, \mathsf{e}_{N_0}^0\} \cup (\mathsf{e}_n^p)_{n\in\mathbb{Z}^*}$ *is an orthonormal basis for* $\mathcal{H}$. $\{\mathsf{e}_1^0, \ldots, \mathsf{e}_{N_0}^0\}$ *can be completed to an orthonormal basis for* $\ker \mathcal{Q}$, *that is, there exist an orthonormal sequence* $(\mathsf{e}_n^s)_{n\in\mathbb{A}_s} \subset \mathcal{X}$ *such that* $\{\mathsf{e}_1^0, \ldots, \mathsf{e}_{N_0}^0\} \cup (\mathsf{e}_n^s)_{n\in\mathbb{A}_s}$ *is an orthonormal basis for* $\ker \mathcal{Q}$. *Moreover,* $\{\mathsf{e}_1^0, \ldots, \mathsf{e}_{N_0}^0\} \cup (\mathsf{e}_n^p)_{n\in\mathbb{Z}^*} \cup (\mathsf{e}_n^s)_{n\in\mathbb{A}_s}$ *is an orthonormal basis for* $\mathcal{X}$.

Note that $\mathbb{A}_s$ is an infinite countable set, serving as the index set for (e_n^s). This analysis suggests the following classification for the cavity modes, see also [4]:

- Primary modes $(\mathsf{e}_n^p)_{n\in\mathbb{Z}^*}$ (solenoidal, non-irrotational).
- Static modes $\{\mathsf{e}_1^0, \ldots, \mathsf{e}_{N_0}^0\}$ (solenoidal, irrotational).
- Secondary modes $(\mathsf{e}_n^s)_{n\in\mathbb{A}_s}$ (non-solenoidal, irrotational).

We also have that an arbitrary field $\mathsf{e} \in \mathcal{X}$ can be represented as

$$\mathsf{e} = \sum_{i=s,0,p} \sum_{n\in\mathbb{A}_i} \left\langle \mathsf{e}, \mathsf{e}_n^i \right\rangle \mathsf{e}_n^i, \tag{12}$$

where $\mathbb{A}_0 := \{1, 2, \ldots, N_0\}$, $\mathbb{A}_p := \mathbb{Z}^*$. If, in addition, $\mathsf{e} \in \mathfrak{D}(\mathcal{Q})$, then

$$\mathcal{Q}\mathsf{e} = \sum_{n\in\mathbb{A}_p} \omega_n \left\langle \mathsf{e}, \mathsf{e}_n^p \right\rangle \mathsf{e}_n^p. \tag{13}$$

5. THE INHOMOGENEOUS PROBLEM

We now allow the presence of EM currents. In the frequency domain, this is modeled with the equation

$$\mathcal{Q}\mathsf{e} = \omega\mathsf{e} + \mathsf{j}, \tag{14}$$

where $\mathsf{j} = \mathsf{j}(\omega, \mathbf{r}) \in \mathcal{X}$. In the view of representations (4), (13), (14) reads

$$\sum_{n\in\mathbb{A}_p} \omega_n \left\langle \mathsf{e}, \mathsf{e}_n^p \right\rangle \mathsf{e}_n^p = \omega \sum_{i=s,0,p} \sum_{n\in\mathbb{A}_i} \left\langle \mathsf{e}, \mathsf{e}_n^i \right\rangle \mathsf{e}_n^i + \sum_{i=s,0,p} \sum_{n\in\mathbb{A}_i} \left\langle \mathsf{j}, \mathsf{e}_n^i \right\rangle \mathsf{e}_n^i,$$

which lead to the equations

$$(\omega_n - \omega) \left\langle \mathsf{e}, \mathsf{e}_n^p \right\rangle = \left\langle \mathsf{j}, \mathsf{e}_n^p \right\rangle, \; n \in \mathbb{A}_p, \tag{15}$$

$$\omega \left\langle \mathsf{e}, \mathsf{e}_n^i \right\rangle = -\left\langle \mathsf{j}, \mathsf{e}_n^i \right\rangle, \; i = s, 0, \; n \in \mathbb{A}_i. \tag{16}$$

Equations (15), (16) lead to the following result, a variant of the Fredholm Alternative:

Proposition 10. *a) Let* $\omega \neq \omega_n$, $n \in \mathbb{Z}$. *Then* (14) *has a unique solution given by*

$$\mathsf{e} = -\frac{1}{\omega} \sum_{i=s,0} \sum_{n\in\mathbb{A}_i} \left\langle \mathsf{j}, \mathsf{e}_n^i \right\rangle \mathsf{e}_n^i + \sum_{n\in\mathbb{A}_p} \frac{1}{\omega_n - \omega} \left\langle \mathsf{j}, \mathsf{e}_n^p \right\rangle \mathsf{e}_n^p. \tag{17}$$

b) Let $\omega = \omega_m$ *for some* $m \in \mathbb{Z}^*$. *Then* (14) *has a solution if and only if* j *is orthogonal to eigenspace* $\ker(\omega_m I - \mathcal{Q}_{\mathcal{H}})$. *In this case, a solution of* (14) *is of the form*

$$\mathsf{e} = -\frac{1}{\omega_m} \sum_{i=s,0} \sum_{n\in\mathbb{A}_i} \left\langle \mathsf{j}, \mathsf{e}_n^i \right\rangle \mathsf{e}_n^i + \sum_{\substack{n\in\mathbb{A}_p \\ \omega_n \neq \omega_m}} \frac{1}{\omega_n - \omega_m} \left\langle \mathsf{j}, \mathsf{e}_n^p \right\rangle \mathsf{e}_n^p + \mathsf{u} \tag{18}$$

for some $\mathsf{u} \in \ker(\omega_m I - \mathcal{Q}_{\mathcal{H}})$.
c) Let $\omega = 0$. *Then* (14) *has a solution if and only if* j *is orthogonal to the kernel* $\ker \mathcal{Q}$. *In this case, a solution of* (14) *is of the form*

$$\mathsf{e} = \mathsf{u} + \sum_{n\in\mathbb{A}_p} \frac{1}{\omega_n} \left\langle \mathsf{j}, \mathsf{e}_n^p \right\rangle \mathsf{e}_n^p \tag{19}$$

for some $\mathsf{u} \in \ker \mathcal{Q}$.

REFERENCES

1. Aksoy, S. and O. A. Tretyakov, "The evolution equations in study of the cavity oscillations excited by a digital signal," *IEEE Trans. Antennas Prop.*, Vol. 52, No. 1, 2004.
2. Dautray, R. and J. L. Lions, *Mathematical Analysis and Numerical Methods for Science and Technology, Vol. 3: Spectral Theory*, Springer, Berlin, 1990.
3. Devanz, G. and J. Plouin, "Conceptual design of the beta = 0.86 cavities for the superconducting Linac of the ESS," *Proceedings of SRF*, Chicago, Illinois, USA, July 2011.
4. Geyi, W., "Time-domain theory of metal cavity resonator," *Progress In Electromagnetics Research*, Vol. 78, 219–253, 2008.
5. Helmberg, G., *Introduction to Spectral Theory in Hilbert Spaces*, North Holland, Amsterdam, 1969.
6. Kurokawa, K., "The expansions of electromagnetic fields in cavities," *IRE Trans. Microwave Theory Techniques*, Vol. 6, No. 2, 178–187, 1957.
7. Lindroos, M., S. Molloy, D. McGinnis, C. Darve, and H. Danared, "The ESS Linac design," *Proceedings of LINAC*, Tel-Aviv, Israel, December 2012.
8. Monk, P., *Finite Elements Method for Maxwell's Equations*, Clarendon Press, Oxford, 2003.
9. Omar, A., *Electromagnetic Scattering and Material Characterization*, Artech House, Boston, 2011.
10. Slater, J. C., "Microwave electronics," *Review Modern Physics*, Vol. 18, 441–512, 1946.
11. Teichmann, T. and E. P. Winger, "Electromagnetic field expansions in loss free cavities excited through holes," *J. Applied Physics*, Vol. 24, 262–267, 1953.

Paper IV

Time Domain Analysis of Higher Order Modes Induced Power Dissipation in Accelerating Cavities

Gabriele Costanza and Anders Karlsson.

Abstract

We give a semi-analytical method for the calculation of the transient power and energy dissipatedin the cavity walls of an accelerating structure, due to the excitation of the higher order modes (HOMs) by a sequence of accelerating bunches. We treat the case where more than one bunch is present in the structure at the same time. The dissipated power is evaluated by using the Lagrangian formalism and the dissipation function. Both the dissipated power from the transient fields, present when the bunch is inside the cavity, and from the time harmonic fields, present, when the bunch has left the cavity, are included in the evaluations. This method is applied to the six cell elliptic medium beta cavities for the LINAC of the European Spallation Source (ESS). The simulations constitute a thorough test of the dissipated power of the design.

1 Introduction

Microwave cavities are ubiquitous in the microwave engineering world, in particular they are the workhorses of particle accelerators such as the European Spallation Source (ESS) [1,2]. The interaction between the beam and the cavity fields can be detrimental for the dissipation in the structure and for the stability of the beam [3–5]. Thus, an evaluation of the power dissipated and of the induced electric and magnetic field strengths, is necessary to validate the cavity design.

We propose a semi-analythical method for the calculation of the power and energy dissipated in the cavity walls induced by multiple accelerating bunches, with more than one bunch present in the cavity at the same time. The problem is interpreted in the framework of the Lagrangian formalism and, in particular, it makes use of the dissipation function. The main advantage of using the Lagrangian dissipation function compared to the customary approaches like [6–8] is that it is enables the evaluation, not only the average, but also the transient power and energy dissipated in the walls of the cavity due to the HOM excited by a sequence of bunches. Well established methods like [10–13] calculate wake potentials and the energy deposited in the HOMs, but do not include the evaluation of energy dissipated in the cavity walls in the case here treated.

A customary approach to the evaluation of the dissipated power is to determine the complex voltage excited by a charge (or a point bunch) passing through the cavity, see for example [6–8]. That method allows to determine the envelope of the R/Q-normalized HOM induced voltage and power in the steady state. The R/Q is then only evaluated at the mode frequencies and not at neighbouring frequencies. Our approach differs in that we in addition to the average dissipated power at the fixed resonance frequencies also evaluate the transient power that is dissipated while the bunch is inside the cavity. By that we include the dissipated power at all frequencies.

The characteristics of the pulsed beam in our model are depicted in figure 1. The pulse length is σ_p and each pulse is made of N point-like bunches, at the arrows in figure 1, separated a time T_b in time. The bunches travel along the symmetry axis of the cavity and are accelerated by the electric field in the cavity. Part of the energy delivered by the bunches is stored in the cavity and interacts with succeeding bunches, while part of it is dissipated. In our numerical examples we study a worst-case scenario where we omit the power loss through couplers. It is from such evaluations one can decide if the design of the cavity needs to be adjusted or if an HOM coupler is needed for dampening the HOM. Our simulations are made for six cell medium beta elliptic cavities for proton accelerators. The specific cavity used in the simulations operates at the frequency 704.42 MHz and is intended for the ESS LINAC [9]. We consider the interaction between the beam and the axially symmetric (monopolar) modes with resonant frequency less than 3 GHz (see figure 2). The average electromagnetic power dissipation of the modes above 3 GHz is negligible (see fig 3). The 3 GHz limit is in accordance with the study [5] of the SPL cavities [14]. Multipolar modes are not considered since their influence on the beam and their dissipated power are negligible in axially symmetric cavities for proton accelerators, see [5, 15]. The power coupler causes a perturbation of the fundamental mode. In appendix 6 we present a 3D calculation that shows that this perturbation is small and confined to a narrow region close to the coupler. The conclusion is that the perturbation has a negligible influence on the dissipated power.. The problem of determining the HOM and their power in the six cell elliptic cavities is complicated by the fact that there is more than one bunch in the cavity at the same time. The excited fields of the HOM are much weaker than the accelerating field and their influence on the acceleration of the bunch can be neglected. The excitation of the accelerating mode is in general not small compared to the RF-field fed to the cavity and it will affect the amplitude and phase of the accelerating mode. Such effects are handled by the control system and are not in the scope of this paper.

In section 2 we formulate the problem, give the basic equations for the time evolution of the HOM and introduce the Lagrangian formalism and dissipation function. Section 3 presents the numerical simulations. All of these are relevant for the medium beta elliptic cavities of the linear accelerator of ESS. A derivation of the expressions for the amplitudes and phases of the HOM is given in the Appendix 5. We consider this derivation to be somewhat shorter and easier to follow than the derivations found in other papers. Throughout the paper we use the time dependence $e^{i\omega t}$ when necessary.

2 The Time Domain Cavity Problem

For convenience we devote subsections 2.1 and 2.2 for the basic theory of the beam excitation of the monopolar HOM of a microwave cavity. The theory is well known but comes in a number of different shapes in the literature, see [10–13, 16]. Our analysis is general and holds for most types of cavities and pulsed beams. Subsection 2.3 contains a non-standard analysis of the dissipated power based upon the dissipation function in a Lagrangian formalism. Together with the numerical examples in subsection 3, section 2.3 constitutes our main contribution to the community of accelerator technology.

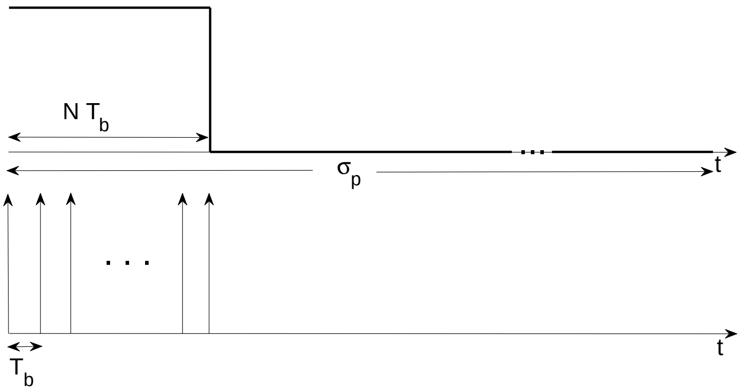

Figure 1: Time Structure of the bunched beam. The bunches are distant T_b seconds and one pulse is σ_p seconds long.

2.1 Basic equations

The cavity is a linear, causal and time invariant system, defined by the domain $\Omega \subset \mathbb{R}^3$ enclosed by a surface, $S \subset \mathbb{R}^3$, and filled with vacuum. The conductivity of the walls at $S \subset \mathbb{R}^3$ is very high and we use the approximation that the walls are perfectly conducting (PEC) in the evaluation of the eigenfields. We then take a finite conductivity into account in the evaluation of the dissipation. By comparing evaluations of the dissipated power using fields obtained with impedance boundary conditions we have confirmed that this approximation does not jeopardise the accuracy of the dissipated power.

The subjects of the time-domain analysis are the electric field $\boldsymbol{\mathcal{E}}(\boldsymbol{r}, t)$, with units $\frac{V}{m}$, the magnetic field $\boldsymbol{\mathcal{H}}(\boldsymbol{r}, t)$, with units $\frac{A}{m}$ and the electric current density, $\boldsymbol{\mathcal{J}}_e(\boldsymbol{r}, t)$, with units $\frac{A}{m^2}$. These vector fields are functions of the space variable $\boldsymbol{r} \in \Omega$ of the time variable $t \in \mathbb{R}$ and they satisfy Maxwell's equations:

$$\begin{cases} \nabla \times \boldsymbol{\mathcal{E}} = -\mu_0 \dfrac{\partial \boldsymbol{\mathcal{H}}}{\partial t} & \text{(1a)} \\ \nabla \times \boldsymbol{\mathcal{H}} = \epsilon_0 \dfrac{\partial \boldsymbol{\mathcal{E}}}{\partial t} + \boldsymbol{\mathcal{J}}_e & \text{(1b)} \end{cases}$$

for $\boldsymbol{r} \in \Omega$. with the PEC boundary condition:

$$\hat{\boldsymbol{n}} \times \boldsymbol{\mathcal{E}}(\boldsymbol{r}, t) = \boldsymbol{0}, \qquad \text{for} \quad \boldsymbol{r} \in S,\ t \in \mathbb{R}_+. \tag{2}$$

At $t = 0$ the first bunch arrives at the cavity and the electromagnetic fields in the cavity are identically zero for $t \leq 0$, in accordance with the *principle of causality*. We further require that all the vector fields in (1a) and (1b) belong to the real space of functions that for every time are square integrable in space, that is, all the fields in the cavity have finite energy.

The *first step* in the solution of the problem is to obtain the set of eigenvalues and eigenfields of the cavity eigenvalue problem. In [19] it was shown that the cavity eigenfields can be classified in primary, secondary and static eigenfields (see also [17]) and the decomposition is valid also in the time domain, see for example [18]. In this paper we follow [19] and classify the modes in only two groups, primary and secondary modes, but since we restrict the analysis to simply connected cavities the secondary modes can be ignored (see [20, 21]).

In *the second step* the excited fields are expanded in series of the eigenfields with time dependent amplitudes:

$$\boldsymbol{\mathcal{E}} = \sum_n \mathbf{E}_n \int_\Omega \boldsymbol{\mathcal{E}} \cdot \mathbf{E}_n \, \mathrm{d}\Omega = \sum_n e_n(t)\mathbf{E}_n(\mathbf{r}), \tag{3}$$

$$\boldsymbol{\mathcal{H}} = \sum_n \mathbf{H}_n \int_\Omega \boldsymbol{\mathcal{H}} \cdot \mathbf{H}_n \, \mathrm{d}\Omega = \sum_n h_n(t)\mathbf{H}_n(\mathbf{r}), \tag{4}$$

The eigenfields are normalized according to:

$$\int\limits_\Omega |\boldsymbol{E}_n(\boldsymbol{r})|^2 \, \mathrm{d}\Omega = 1,$$

$$\int\limits_\Omega |\boldsymbol{H}_n(\boldsymbol{r})|^2 \, \mathrm{d}\Omega = 1,$$

By introducing the wavenumber $\kappa_n = \omega_n\sqrt{\mu_0\epsilon_0}$ and the wave impedance $\eta_0 = \sqrt{\mu_0/\epsilon_0}$, we find that the primary modes satisfy [16, 21]:

$$\begin{cases} \nabla \times \mathbf{E}_n = \kappa_n \mathbf{H}_n & (5) \\ \nabla \times \mathbf{H}_n = \kappa_n \mathbf{E}_n & (6) \end{cases}$$

We also use the following notation:

$$(\mathbf{A}, \mathbf{B}) = \int_\Omega \mathbf{A} \cdot \mathbf{B}^* \, \mathrm{d}\Omega,$$

$$\langle \mathbf{A}, \mathbf{B} \rangle = \int_S \mathbf{A} \cdot \mathbf{B}^* \, \mathrm{d}S,$$

for $\mathbf{A}$, $\mathbf{B} \in L^2\left(\Omega; \mathbb{C}^3\right)$ and where the asterisk denotes the complex conjugate.

The induction law and the orthogonality of the primary modes give:

$$(\nabla \times \boldsymbol{\mathcal{E}}, \mathbf{H}_m) = -\mu_0 \frac{dh_n}{dt} \tag{7}$$

We rewrite the left hand side of (7) using (5), the expansion (4) and the orthogonality of the modes:

$$(\nabla \times \boldsymbol{\mathcal{E}}, \mathbf{H}_n) = \sum_{n,m} e_n(t)\left(\nabla \times \mathbf{E}_m, \mathbf{H}_n\right) = \sum_{n,m} \kappa_n\, e_n(t)\left(\mathbf{H}_m, \mathbf{H}_n\right) = \kappa_n\, e_n(t). \tag{8}$$

Substituting (8) in the left hand side of (7), leads to:

$$\kappa_n\, e_n = -\mu_0 \frac{dh_n}{dt} \tag{9}$$

Applying the same arguments to the Ampère law (1b) gives

$$\kappa_n\, h_n = \epsilon_0 \frac{de_n}{dt} + (\boldsymbol{\mathcal{J}}_e, \mathbf{E}_n) \tag{10}$$

We see that (10) and (10) form a system of equations that can be solved for the mode amplitudes. We rewrite the system of equations as:

$$\begin{cases} \dfrac{de_n}{dt} - \omega_n \eta_0 h_n = -\dfrac{1}{\epsilon_0}\left(\boldsymbol{\mathcal{J}}_e, \mathbf{E}_n\right) & \text{(11a)} \\ \dfrac{dh_n}{dt} + \dfrac{\omega_n}{\eta_0} e_n = 0 & \text{(11b)} \\ e_n(0) = h_n(0) = 0 & \text{(11c)} \\ t \in \mathbb{R}^+ & \text{(11d)} \end{cases}$$

where n is the mode index. The dissipation now needs to be added to these equations. The standard way of doing this is to use the $Q-$factor. It is seen that a finite, but high, intrinsic quality factor for the mode n, $Q_{0,n}$, gives rise to a mode dependent dissipation term in the equations, with a loss coefficient $2\gamma_n = \omega_n / Q_{0,n}$. The system of equations (11a)-(11b) in matrix form is:

$$\frac{d}{dt}\begin{pmatrix} e_n(t) \\ h_n(t) \end{pmatrix} + \begin{pmatrix} 2\gamma_n & -\omega_n \eta_0 \\ \omega_n/\eta_0 & 0 \end{pmatrix}\begin{pmatrix} e_n(t) \\ h_n(t) \end{pmatrix} = -\begin{pmatrix} \dfrac{1}{\epsilon_0}\left(\boldsymbol{\mathcal{J}}_e, \mathbf{E}_n\right) \\ 0 \end{pmatrix},$$

If we only consider ohmic losses in the walls, the intrinsic quality factor for the mode n is defined as

$$Q_{0,n} = \frac{\omega_n W_n}{P_{d,n}} = \frac{\omega_n \mu_0 \int\limits_{\Omega} |\boldsymbol{H}_n|^2\, \mathrm{d}\Omega}{R_s \int\limits_{S} |\boldsymbol{H}_n|^2\, \mathrm{d}s} \tag{12}$$

Here R_s is the surface resistance of the cavity, see for example [8]. Equations (11) or (12) describe the state of the system, that is, the amplitudes of the electric and magnetic fields, at every instant t.

With this procedure the problem is divided into an eigenvalue problem, which can be solved with great accuracy (see [22]) and an evolution problem that can be solved semi-analytically, for example, with the procedure outlined in the following. Modern commercial electromagnetic simulation programs such as Comsol [23] allow efficient calculations of both monopolar and multipolar eigenfields with a 2D simulator.

In the *third step*, treated in 2.2, an explicit solution to (11) is given. A formal treatment of the problem can be found for example in [24, 25]. In section 2.3 we apply the Lagrangian formalism for the calculation of the power dissipated in the cavity walls.

2.2 Cavity Driven by a Beam

Equation (12) allows us to calculate the electric and magnetic fields excited by electric current distributions located in Ω. In particular, we are interested in evaluating the mode excitations due to a beam made of N bunches traveling along the symmetry axis of an axially symmetric cavity. Due to the linearity of Maxwell's equations it is possible to evaluate the electric and magnetic field excited by a single bunch for $0 \leq t < \infty$, and then superimpose these fields to take into account the effect of N bunches.

A bunch of charged particles corresponds to an electric current density. We assume that the spread in both the longitudinal and radial directions is negligible and that the bunch can be treated as a point charge. In cylindrical coordinates (r, ϕ, z) we have:

$$\boldsymbol{\mathcal{J}}_e(r, z, t) = q_0 \beta(t) c \frac{\delta(r)}{2\pi r} \delta\left(z - z(t)\right) \hat{\mathbf{z}}, \tag{13}$$

where $z(t) = \beta(t)ct$ is the position of the particle at the instant t, $\beta(t) = v(t)/c$ is the speed of the bunches normalized with the speed of light in vacuum c and q_0 is the bunch charge.

We now proceed with the solution of (12) for the cavity mode n. We use the assumption that before the bunch enters the cavity there are no fields or charges in Ω:

$$e_n(t) = 0, \qquad t < 0. \tag{14}$$

For convenience we introduce

$$\boldsymbol{x}(t) = \begin{pmatrix} e_n(t) \\ h_n(t) \end{pmatrix}, \quad A_n = \begin{pmatrix} 2\gamma_n & -\omega_n \eta_0 \\ \omega_n/\eta_0 & 0 \end{pmatrix}, \tag{15}$$

and

$$\boldsymbol{f} = -\begin{pmatrix} \frac{1}{\epsilon_0}\left(\boldsymbol{\mathcal{J}}_e, \mathbf{E}_n\right) \\ 0 \end{pmatrix}. \tag{16}$$

For $0 \leq t < T_0$ we have $\boldsymbol{f} \neq 0$. Problem (12), with homogeneous initial conditions, has a solution $\boldsymbol{x}(t)$ given by [26]:

$$\begin{cases} \boldsymbol{x}_n(t) = \displaystyle\int_0^t e^{(t-\tau)A_n}\, \boldsymbol{f}_n(\tau)\, \mathrm{d}\tau \\ \boldsymbol{f}_n(t) = -\left(\dfrac{q_0}{\epsilon_0}\beta(t)c\, E_{z,n}(0,0,\beta ct),\ \ 0\right)^T \end{cases} \tag{17}$$

where T denotes transpose.

The matrix operator A_n can be diagonalized by $A_n = P_n \Lambda_n P_n^{-1}$, where the diagonal elements of Λ are the eigenvalues:

$$\Lambda_n = \begin{pmatrix} -\gamma_n - \mathrm{i}\omega_n\sqrt{1-\dfrac{1}{4Q_{0,n}^2}} & 0 \\ 0 & -\gamma_n + \mathrm{i}\omega_n\sqrt{1-\dfrac{1}{4Q_{0,n}^2}} \end{pmatrix},$$

If we define $\theta_n = \omega_n\sqrt{1-\frac{1}{4Q_{0,n}^2}}$, we have:

$$P_n = \begin{pmatrix} 1 & 1 \\ -\dfrac{-\gamma_n + \mathrm{i}\theta_n - \frac{\mathrm{i}\omega_n}{\eta_0^2}}{-\mathrm{i}\omega_n\eta_0^2 + \gamma_n - \mathrm{i}\theta_n} & -\dfrac{-\gamma_n - \mathrm{i}\theta_n - \mathrm{i}\frac{\omega_n}{\eta_o^2}}{-\mathrm{i}\omega\eta_0^2 + \gamma_n - \mathrm{i}\theta_n} \end{pmatrix}.$$

and $e^{-A_n t} = P_n e^{-\Lambda_n t} P_n^{-1}$ (see Lemma 2.6 in [25]).

When the bunch has left the cavity, that is, for $t \geq L/v$, the modes evolve according to:

$$\begin{aligned} &\boldsymbol{x}_n(t) = \boldsymbol{x}_n(L/v)\, e^{-At} = \\ &\begin{pmatrix} |A_{e,n}|\, e^{-\gamma_n(t-L/v)} \cos\left[\theta_n(t-L/v) + \phi_{e,n}\right] \\ |A_{h,n}|\, e^{-\gamma_n(t-L/v)} \sin\left[\theta_n(t-L/v) + \phi_{h,n}\right] \end{pmatrix}, \end{aligned} \tag{18}$$

With the preceding equation it is possible to calculate the free oscillations, either numerically with the matrix exponential (second member), or explicitly (last member). The derivation of $A_{e,n}$ and $\phi_{e,n}$ (see appendix A), gives:

$$
\begin{aligned}
&|A_{e,n}| = \frac{q_0}{\epsilon_0} \left| \int\limits_0^L e^{\gamma_n z/v} \, e^{-\mathrm{i}\omega_n z/v} E_{z,n}(0,0,z) \, \mathrm{d}z \right|, \\
&|A_{h,n}| = \eta_0 |A_{e,n}|, && \text{(19a)} \\
&\phi_{e,n} = \arg \left(\int\limits_0^L e^{\gamma_n z/v} e^{-\mathrm{i}\omega_n z/v} E_{z,n}(0,0,z) \, \mathrm{d}z \right) + \\
&+ \pi + \arctan\left(\frac{\gamma_n}{\omega_n}\right) && \text{(19b)} \\
&\phi_{h,n} = \phi_{e,n}. && \text{(19c)}
\end{aligned}
$$

A second order equation for $e_n(t)$ can be obtained from (11). By using (13), the right hand side of (11a) becomes

$$
\frac{\partial}{\partial t} \left(\boldsymbol{\mathcal{J}}_e, \; \mathbf{E}_n \right) = \omega_n^2 F_n(t) \tag{20}
$$

where

$$
F_n(t) = \frac{q_0}{\omega_n^2} (\beta(t) c)^2 \frac{\partial E_{z,n}(0,0,z)}{\partial z} + \frac{q_0}{\omega_n^2} \beta(t) c^2 \frac{d\beta(t)}{dz} E_{z,n}(0,0,z), \tag{21}
$$

and, $z = t\beta(t)c$. By substituting (11b) into (11a) differentiated with respect to time, and using (20), we obtain:

$$
\frac{d^2 e_n(t)}{dt^2} + 2\gamma_n \frac{de_n(t)}{dt} + \omega_n^2 e_n(t) = -\frac{\omega_n^2}{\epsilon_0} F_n(t) \tag{22}
$$

where the electric field $E_{n,z}$ is evaluated at the position of the particle

$$
z(t) = c \int_0^t \beta(t') \, \mathrm{d}t'
$$

The increase in speed in each cavity is often small enough such that β can be considered to be constant and then $z = \beta ct$.

2.3 Lagrangian formalism and the dissipation function

Equation (22) is the driven-damped harmonic oscillator equation, which can be studied in a simple way by using the Lagrangian formalism. Such formalism allows us to define, in a simple and compact way, a dissipation function. The function gives the power dissipated due to a frictional force proportional to the velocity of the generalized coordinate (see [27, 28]), and an equation for the energy balance of the whole system. We introduce the generalized coordinates Q (column vector) as

$$Q = (q_1, \ldots, q_N)^T = (e(t)_1, \ldots, e(t)_N)^T ,$$

and the generalized velocities

$$\dot{Q} = (\dot{q}_1, \ldots, \dot{q}_N)^T,$$

In our case the *Lagrangian* that describes the eigenmode dynamic has the form:

$$\mathcal{L}(t, q, \dot{q}) = \frac{1}{2}\,\dot{Q}^T \boldsymbol{\varpi}\,\dot{Q} - \frac{\epsilon}{2}\,Q^T Q + \mathcal{F}^T \cdot Q,$$

where, $\mathcal{F} = (F_1(t), \ldots, F_N(t))^T$ and $\boldsymbol{\varpi}$ is the diagonal matrix

$$\boldsymbol{\varpi} = \begin{bmatrix} \epsilon_0/\omega_1^2 & \cdots & 0 \\ \vdots & \ddots & \vdots \\ 0 & \cdots & \epsilon_0/\omega_N^2 \end{bmatrix}.$$

The first term on the right hand side

$$\mathcal{T} = \frac{1}{2}\,\dot{Q}^T\,\boldsymbol{\varpi}\,\dot{Q},$$

is the kinetic energy, while

$$\mathcal{V} = \frac{\epsilon_0}{2}\,Q^T Q - \mathcal{F}^T \cdot Q$$

is the (generalized) potential energy. With the previous definitions, $\mathcal{T}$ and $\mathcal{V}$ are measured in Joules and they represent the magnetic and the electric energy, respectively, while $\mathcal{F}$, represents the driving force. The picture is completed by the introduction of dissipative forces, which are not conservative and cannnot be derived from a potential. To see how these forces come into play we introduce the Rayleigh's dissipation function, $\mathcal{R}$, and write the Euler - Lagrange equations for the mode n as:

$$\begin{aligned} \frac{d}{dt}\left(\frac{\partial \mathcal{L}}{\partial \dot{q_n}}\right) - \frac{\partial \mathcal{L}}{\partial q_n} + \frac{\partial \mathcal{R}}{\partial \dot{q}_n} &= \frac{\epsilon_0}{\omega_n^2}\left(\ddot{q}_n + 2\gamma_n \dot{q}_n + \omega_n^2 q_n\right) \\ &= -F_n(t) \end{aligned}$$

which is identical to (22). $\mathcal{R}$ is the quadratic function of the velocity

$$\mathcal{R} = \frac{1}{2}\,\dot{Q}^T \boldsymbol{d}\,\dot{Q}. \tag{23}$$

where

$$\boldsymbol{d} = 2\begin{bmatrix} \gamma_1\epsilon_0/\omega_1^2 & \cdots & 0 \\ \vdots & \ddots & \vdots \\ 0 & \cdots & \gamma_N\epsilon_0/\omega_N^2 \end{bmatrix}.$$

We can show that the generalized dissipative forces $\mathcal{D}$ that cause the dissipation, are obtained from the dissipation function by means of the formulas:

$$\mathcal{D} = -\nabla_{\dot{Q}}\mathcal{R}.$$

We also underline that other choices for the Lagrangian function are possible. The physical interpretation of the dissipation function is the following: $2\mathcal{R}$ is the rate of energy (power) dissipated by the dissipative, non-potential forces, see [28, 29].

The Hamiltonian $\mathcal{H}$, is associated with the Lagrangian by the transform:

$$\mathcal{H}(t, Q, Q) = \dot{Q}\cdot\nabla_{\dot{Q}}\mathcal{L} - \mathcal{L}, \qquad \text{where} \qquad \nabla_{\dot{Q}}\mathcal{L} = \boldsymbol{\varpi}\,\dot{Q} + \mathcal{F},$$

so that

$$\mathcal{H}(t, Q, \dot{Q}) = \frac{1}{2}\,\dot{Q}^T\,\boldsymbol{\varpi}\,\dot{Q} + \frac{\epsilon_0}{2}\,Q^T Q = \mathcal{T} + \mathcal{V}$$

The energy balance equation is:

$$-\mathcal{F}^T\cdot\dot{Q} = \frac{\partial\mathcal{H}}{\partial t} + 2\mathcal{R}, \tag{24}$$

which means that the power given by the source (left hand side) is partially converted into electric and magnetic power of the fields confined in the cavity (first term of the right hand side) and partially dissipated (second term of the right hand side). The Hamiltonian can be interpreted as the electromagnetic energy stored in the cavity at time t. This interpretation is in agreement with Poynting's theorem [30].

3 Results and Discussion

In this section we apply (17) and (23) to calculate the power dissipated in a specific cavity due to the excitation of the higher order modes. The cavity is a six cell elliptic medium beta cavity that was designed for the ESS LINAC.

Our intention is to present simulations that give a comprehensive picture of the dissipation of power in accelerator cavities. The results indicate which HOM are the main contributers to the dissipated power and if the design of the cavity needs to be adjusted in order to shift the frequency of modes that dissipate too much power. In the case of the specific cavities for ESS the conclusion is that the dissipated power is under control and the frequency gap between the frequencies of the HOM and harmonics of the fundamental mode is large enough such that no HOM will grow very strong and affect the beam or dissipate large powers. No HOM couplers are needed and a redesign is not needed for the sake of dissipated power.

A sequence of point bunches passes through a six cell elliptical cavity (presented in [9], see fig. 19) with a bunch frequency $f_b = 352.21$ MHz (bunch period $T_b = 2.83$ ns) and with an initial velocity of $0.67c$. The bunches are accelerated by the accelerating (π) mode resonating at 704.42 MHz. The list of the monopolar modes used in the simulation is in figure 2. The red bars indicate the modes within ±20 MHz from an harmonic of the bunch frequency. We expect these modes to be strongly excited. A total of 66 monopolar modes have been used, which are sufficient to reconstruct causal fields $\mathcal{E}$ and $\mathcal{H}$ since the interaction with modes beyond 3 GHz is negligible (see for example [5]). This is emphasized by the negligible average electromagnetic energy and power dissipation of the modes after the 25th mode resonating at 1771.5 MHz, see figure 3. An animation of $\mathcal{E}_z(z,t)$ that clearly shows the causality of the field, can be visualized by visiting [31]. For the calculation of stored electromagnetic energies and of the dissipated power it is not necessary to use a very large number of bunches, in fact a few hundred bunches are sufficient to reach a state of equilibrium between the power supplied by the beam and the dissipated power (see figure 11). The results refer to a simulation with 1000 bunches of 1 nC of charge each and a surface resistivity of 40 $n\Omega$, but it has been verified that 300 bunches are sufficient to obtain the same results.

First, evolutions of the amplitudes $e_n(t)$ and $h_n(t)$ of the eigenfields are presented. Some examples are in figures 4, 5 and 6. Figure 4 represents the evolution of the electric field amplitude of the accelerating cavity mode, while figures 5 and 6 depict the electric (red) and magnetic (blue) fields evolutions for the mode 24 (resonating at 1749.556 MHz) for one and 1000 bunches respectively. In figure 5, the curve ca be explained as follows: First the bunch is in the beam pipe where the fields are evanescent and the interaction with the bunch is weak. The beam then passes through the cells, where the interaction between the mode and the bunch is strong due to the strong electric field of the mode along the symmetry axis. When the bunch leaves the cavity the mode continue to oscillate with its resonance frequency and with an amplitude that decays very slowly due to the high Q-factor of the mode. It is interesting to compare figures 4, for the accelerating mode (pi-mode), and 6, for mode 24. Mode 24 is a candidate of being dangerous since its frequency is close to the 5th harmonic. The π-mode continues to grow to very large amplitudes since its frequency is exactly twice the frequency of the bunch train. First it grows linearly with time, but as the amplitude increases the dissipation increases. Eventually an equilibrium will be reached where the amplitude is constant and the power delivered by the bunches equals the dissipated power. Mode 24 also grows strong to begin with. However, due to the frequency difference between the 5th harmonic and mode 24, the evolution of the fields accumulates a phase shift that results in the periodic pattern of figure 6. The high frequency oscillations are due to the ringing of the mode at 1749.556 MHz. If the gap in frequency between the 5th harmonic and mode 24 decreases, the period and amplitude of the envelope increases. If the frequency gap is small, the field becomes so strong that it can affect the beam. This is why it is important to design the cavity such that the frequency gaps to the harmonics are not too small. Notice that when the RF source is present, the accelerating mode is the sum of the field generated by the source and the beam.

Figures 7 and 8 show the electromagnetic energy of the mode resonating at 1749.556 MHz and its zoomed in version. The transient, anharmonic character of the response $e_n(t)$, is evident in the energy evolution as well as in the evolution of the dissipation function (figure 9).

Figure 10 represents the integral of the dissipation function for the three most dangerous modes for a single bunch passing through the cavity. Such integral represents the evolution of the dissipated energy $D_e(t)$, in the cavity walls and is defined as:

$$D_e(t) = \int_0^t 2\mathfrak{R}(\tau)\,\mathrm{d}\tau \qquad 0 \le t \le T_{tot} \qquad [J], \tag{25}$$

where T_{tot} is the total simulation time. The dissipated energy is a monotonically increasing function of time. Figure 11 represents the time average dissipated power for 1000 bunches, defined as:

$$P_{diss}(t) = \frac{1}{t} D_e(t) \qquad 0 \le t \le T_{tot} \qquad [W]. \tag{26}$$

Figures 10 - 15 represent the average power dissipated for all the monopolar modes up to 3 GHz in dBW, obtained by taking the time average of $2\mathfrak{R}$. The modes not close to a bunch frequency harmonic, are just slightly excited and contribute very little to the dissipation. The three most dangerous modes (see table 1) modes dissipate 93% of the total power dissipated (see figure 18).

Notice also that the mode resonating at 1743.759 MHz (mode 19) has the highest R/Q (linac definition).

4 Conclusions

A method for the calculation of the dissipated power in the cavity walls due to the excitation of the higher order modes by a bunched beam has been presented. This method takes into account the acceleration of the bunches and the transient fields excited by the beam itself. The method allows to calculate average and transient power and energies dissipated in the HOMs. An example involving the medium-β elliptical cavity for the ESS has been presented. The example is an evaluation of the dissipated power in the cavity. It concludes that five monopolar modes below 3 GHz dissipate 93% of the total power dissipated due to the HOMs excitation. The dissipated powers of the HOM are small enough to be handled without an HOM-coupler.

5 Appendix A

We here derive the expressions for the amplitude $A_{e,n}$ and phase $\phi_{h,n}$ for the mode n. We differentiate (11a), substitute it in (11b) to obtain:

$$\frac{d^2 e_n}{dt^2} + \frac{\omega_n}{Q_{n,0}} \frac{de_n}{dt} + \omega_n^2 e_n = -\frac{1}{\epsilon_0} \frac{\partial}{\partial t} (\boldsymbol{\mathcal{J}}_e, \boldsymbol{E}_n), \tag{27}$$

where the right hand side of (11a) has been evaluated using (13). We now rewrite (27) in the frequency domain:

$$\begin{aligned} &\left(\omega^2 - \omega_n^2 - 2i\omega\gamma_n\right) e_n(\omega) \\ &\qquad = i\omega \frac{q}{\epsilon_0} \int_0^L e^{-i\omega z/v} \, E_{z,n}(0,0,z) \, \mathrm{d}z. \end{aligned} \tag{28}$$

This gives:

$$\begin{aligned} e_n(\omega) = i\omega \frac{q}{\epsilon_0} & \frac{1}{(\omega^2 - \omega_n^2 - 2i\omega\gamma_n)} \\ & \times \int_0^L e^{-i\omega z/v} \, E_{z,n}(0,0,z) \, \mathrm{d}z. \end{aligned} \tag{29}$$

The time domain expression for $e_n(t)$ is obtained by the inverse Fourier transform:

$$e_n(t) = \frac{1}{2\pi} \int_{-\infty}^{+\infty} e_p(\omega) e^{i\omega t} \mathrm{d}\omega, \tag{30}$$

Table 1: Average Power Dissipated.

Mode Frequency [MHz] Mode number	1684.423 14	1735.532 18	1743.759 19	1749.556 24	1771.481 25	other
R/Q @β =0.67 [Ohm]	1.73	3.53	3.64	0.22	0.076	
Q_0	9.3e9	8.72e9	8.66e9	8.61e9	1.1e10	
Avg. Power Dissipated [nW]	0.63	13.1	31.44	5.71	1.39	1.82
Total [nW]	54.1					

where $e_n(\omega)$ is given by (29). A straightforward way to calculate the inverse Fourier Transform of (29) is by using Cauchy's integral formula: we first decompose the term depending on ω in partial fractions to obtain:

$$\begin{aligned} e_n(t) = \frac{1}{2\pi} i \frac{q}{\epsilon_0} \int_{-\infty}^{+\infty} \frac{\omega}{\omega_1 - \omega_2} \left(\frac{1}{\omega - \omega_1} - \frac{1}{\omega - \omega_2} \right) \\ \times \int_0^L e^{-i\omega z/v} \; E_{z,p}(0,z) \; \mathrm{d}z \;\; e^{i\omega t} \; dt, \end{aligned} \tag{31}$$

where $\omega_1 = i\gamma_n + \sqrt{\omega_n^2 - \gamma_n^2}$ and $\omega_2 = i\gamma_n - \sqrt{\omega_n^2 - \gamma_n^2}$. We use the integral formula

$$\oint_C \frac{f(\omega)}{\omega - \omega_0} \; dz = 2i\pi f(\omega_0). \tag{32}$$

For $t \geq L/v$ we close the curve C by a half circle witn infinite radius and circles with infinitesimal radius around the poles in the upper half of the complex plane. To simplify the notation we use

$$g(\omega) = \int_0^L e^{-i\omega z/v} \; E_{z,p}(0,z) \; \mathrm{d}z, \tag{33}$$

so that

$$f(\omega) = \omega \; g(\omega) \; e^{i\omega t}. \tag{34}$$

The result is:

$$e_n(t) = \frac{q}{\epsilon_0} \frac{1}{\omega_1 - \omega_2} \left(\omega_2 \; g(\omega_2) e^{i\omega_2 t} - \omega_1 \; g(\omega_1) e^{i\omega_1 t} \right). \tag{35}$$

for $t \geq L/v$. To simplify the calculation we now make the approximation:

$$\omega_n \gg \gamma_n \Rightarrow \begin{cases} \omega_1 \simeq i\gamma_n + \omega_n \\ \omega_2 \simeq i\gamma_n - \omega_n \end{cases} \tag{36}$$

then also $\omega_1 - \omega_2 = 2\omega_n$. We rewrite the term in the parentheses at the right hand side of (35) as:

$$\begin{aligned} &\omega_2 \int_0^L e^{-\mathrm{i}\omega_2 z/v} E_{z,n}(0,0,z) \; \mathrm{d}z \; e^{\mathrm{i}\omega_2 t} - \omega_1 \int_0^L e^{-\mathrm{i}\omega_1 z/v} E_{z,n}(0,0,z) \; \mathrm{d}z \; e^{\mathrm{i}\omega_1 t} \\ &= (\mathrm{i}\gamma_n - \omega_n) \int_0^L e^{\gamma_n z/v} e^{\mathrm{i}\omega_n z/v} E_{z,n}(0,0,z) \; \mathrm{d}z \; e^{-\gamma_n t} e^{-\mathrm{i}\omega_n t} \\ &- (\mathrm{i}\gamma_n + \omega_n) \int_0^L e^{\gamma_n z/v} e^{-\mathrm{i}\omega_n z/v} E_{z,n}(0,0,z) \; \mathrm{d}z \; e^{-\gamma_n t} e^{\mathrm{i}\omega_n t} \\ &= -2\Re \left\{ (\mathrm{i}\gamma_n + \omega_n) \int_0^L e^{\gamma_n z/v} e^{-\mathrm{i}\omega_n z/v} E_{z,n}(0,0,z) \; \mathrm{d}z \; e^{-\gamma_n t} e^{\mathrm{i}\omega_n t} \right\}, \end{aligned}$$

where $\Re$ denotes the real part and having recognized that the two terms in the second member of the last equation are complex conjugates. Thus

$$e_n(t) = -\frac{q}{\epsilon_0 \omega_n} \Re \left\{ (\mathrm{i}\gamma_n + \omega_n) \int_0^L e^{\gamma_n z/v} e^{-\mathrm{i}\omega_n z/v} E_{z,n}(0,0,z)\, \mathrm{d}z\, e^{-\gamma_n t} e^{\mathrm{i}\omega_n t} \right\} \tag{37}$$

$$= \Re \left\{ -|A_{e,n}|\, e^{\mathrm{i}\phi_{e,n}}\, e^{-\gamma_n t}\, e^{\mathrm{i}\omega_n t} \right\}. \tag{38}$$

Using the approximation (36) and (38) we have the formulas (19).

6 Appendix B

All of the evaluations of the cavity modes in this paper are done with an axisymmetric model of the cavity. The power coupler is not present. This gives reliable and fast simulations of the HOMs evolution. To justify the axisymmetric model we now analyse the perturbations of the modes, caused by the power coupler, and show that these have a negligible effect on the dissipated power. Figure 19 shows the end cell of the cavity with the coupler. The coupler is penetrating the beam pipe by 20 mm, positioning the tip of the antenna at the same distance from the cavity axis as the cell iris. We use a scattering boundary condition at the coaxial waveguide aperture (in blue in figure 19). Inside the cells the cavity fields are not affected by the coupler. It is only in the vicinity of the coupler where the cavity modes of the 3D and axisymmetric models differ. In figure 20 we show the transverse electric and magnetic fields of the fundamental mode from the 3D calculation taken along the black line that goes from the end of the beam pipe, to the end of the first cell. In contrast to the axisymmetric model the coupler intoduces local transverse fields in the fundamental mode, which are absent in the axisymmetric model. The transverse fields are normalized with the maximum electric field along the symmetry axis. As seen in the figure, the fields are very small and exist only in the close vicinity of the coupler. The perturbation of the longitudinal fields are of the same order as the perturbation of the transverse fields. The conclusion from these simulations is that the perturbation in the dissipated power caused by the coupler is negligible. The influence the perturbed modes have on the dynamics of the beam is out of the scope of this paper.

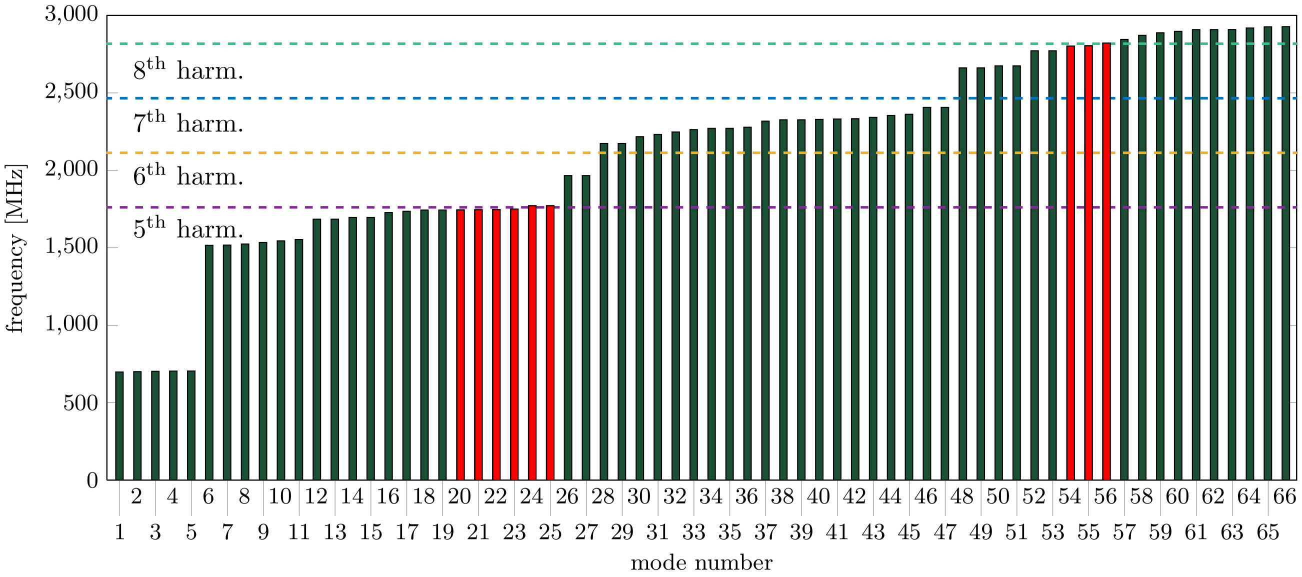

Figure 2: Frequencies of the monopolar modes up to 3 GHz. The red bars indicate the modes close to the respective harmonic of the bunch frequency (352.21 MHz).

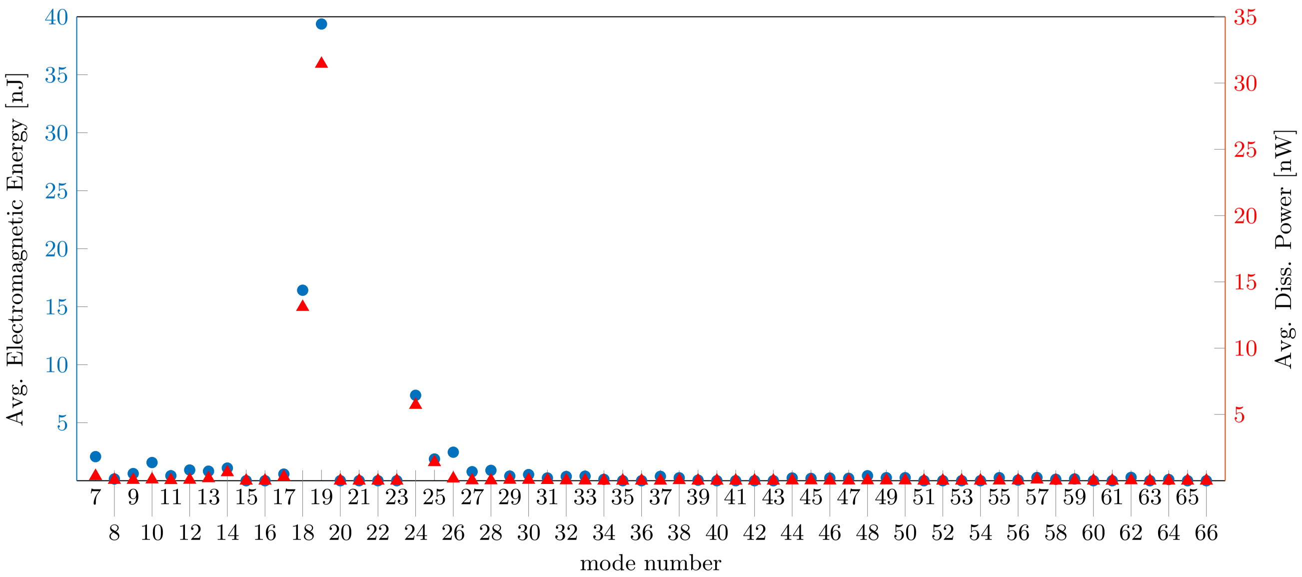

Figure 3: Maximum of the electric field excitation $e(t)$ (blue) and corresponding average power dissipation for the higher order modes (red). The modes 18, 19 and 24 are the most dangerous and dissipate 93% of the total power dissipated in the higher order modes, see also figure (18)

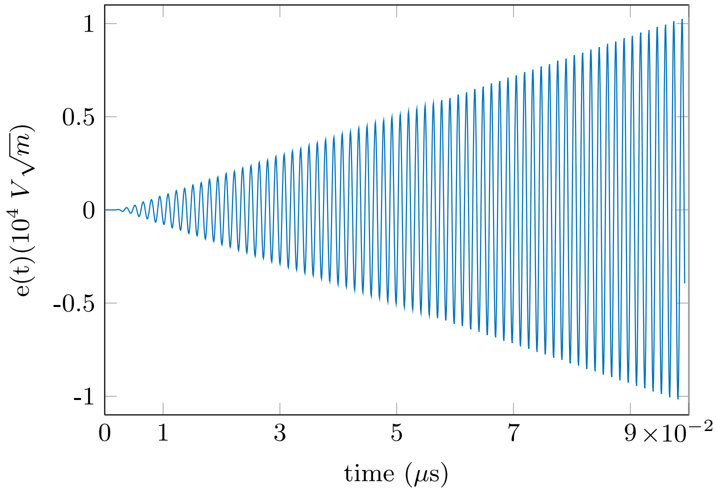

Figure 4: Evolution of the electric field excited by 32 bunches for the accelerating mode resonating at 704.42 MHz. The curve is taken from a simulation done with 1000 bunches, but only the first part of the evolution is shown.

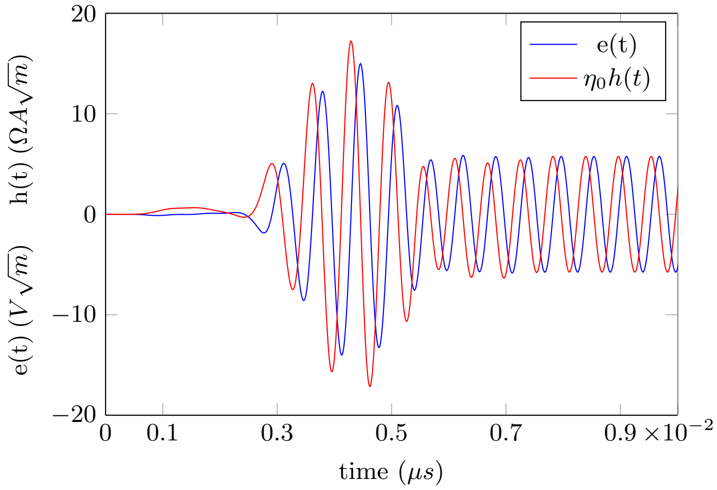

Figure 5: Evolution of electric and magnetic field of the mode resonating at 1749.556 MHz excitated by one bunch. The transient is visible and characterizes the field excitation as well as the behavior of the stored energy.

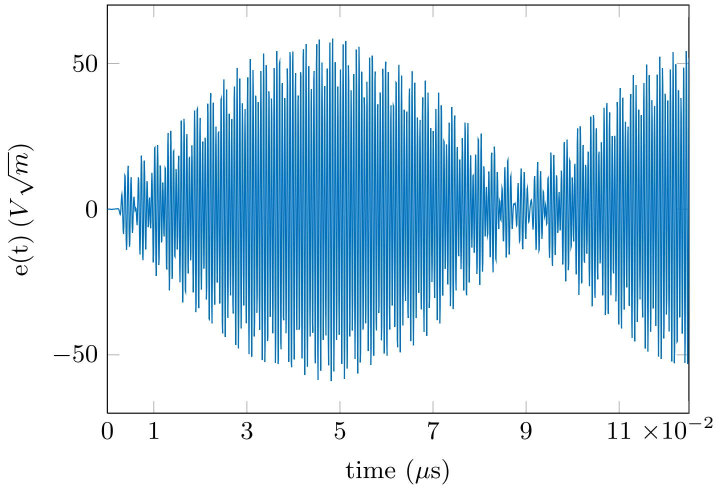

Figure 6: Evolution of the electric field excited by 40 bunches for the mode resonating at 1749.556 MHz. The curve is the first part of a simulation with 1000 bunches. The pattern repeats itself as long as there are bunches in the cavity.

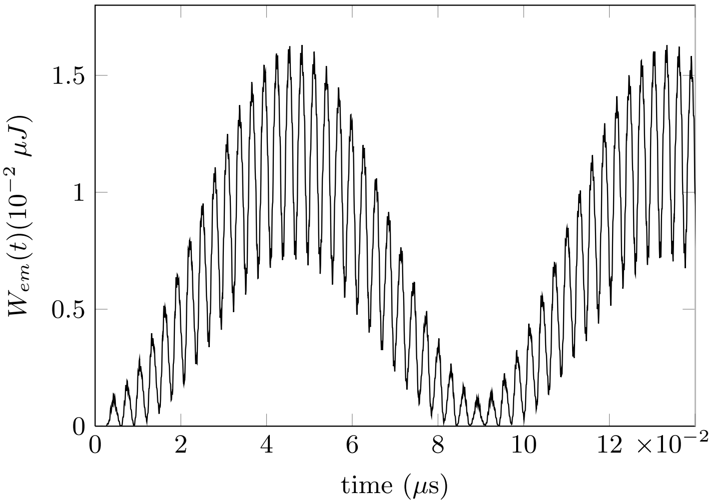

Figure 7: Total electromagnetic energy of the mode number 24 resonating at 1749.556 MHz excited by 40 bunches. The pattern repeats itself as long as there are bunches in the cavity.

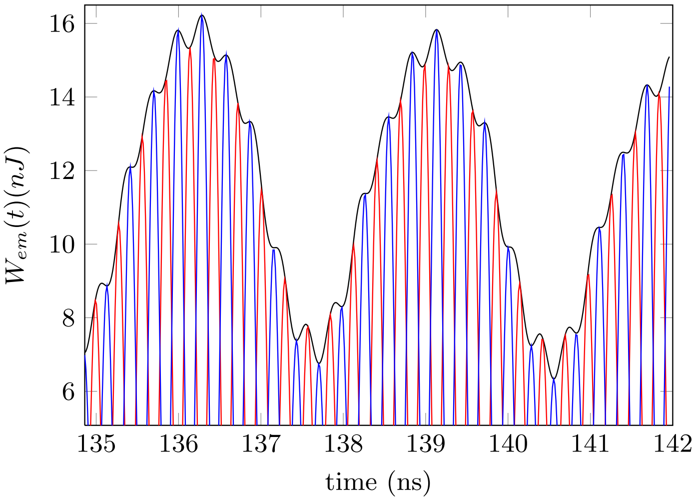

Figure 8: Electromagnetic Energy (zoom in) of the mode number 24 resonating at 1749.556 MHz. Total electromagnetic energy (black), electric energy (red) and magnetic energy (blue).

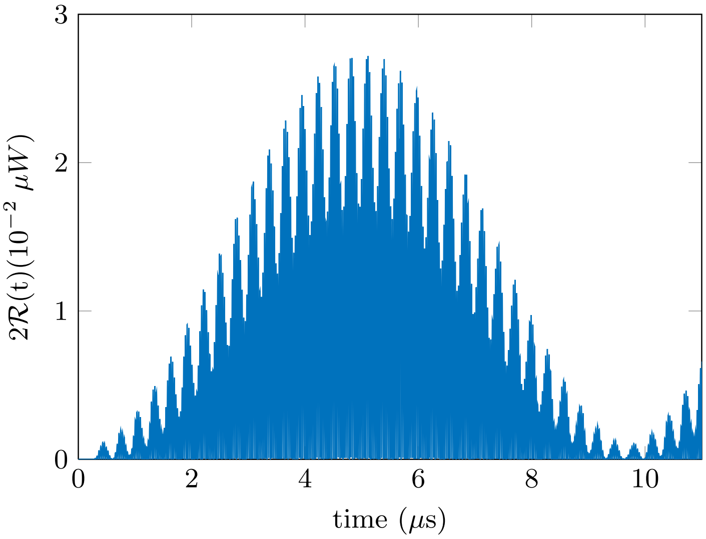

Figure 9: Evolution of the dissipation function for the mode number 24 resonating at 1749.556 MHz.

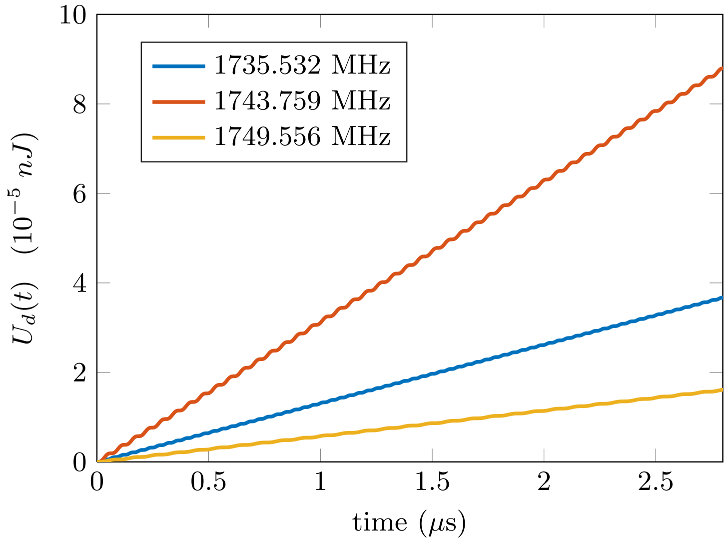

Figure 10: Evolution of the dissipated energy for the modes 18 (blue), 19 (red) and 24 (yellow) for a single bunch.

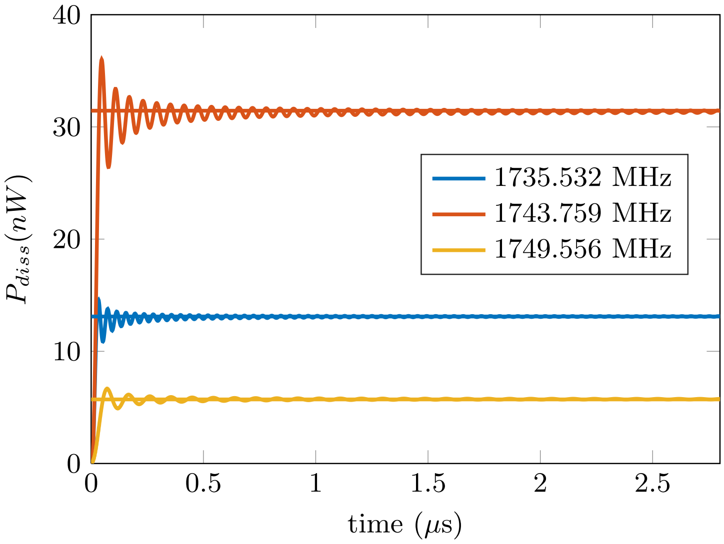

Figure 11: Dissipated power $D_p(t)$ in the cavity walls for the modes 18 (blue), 19 (red) and 24 (yellow) for 1000 bunches. The straight lines represent the average disspated power.

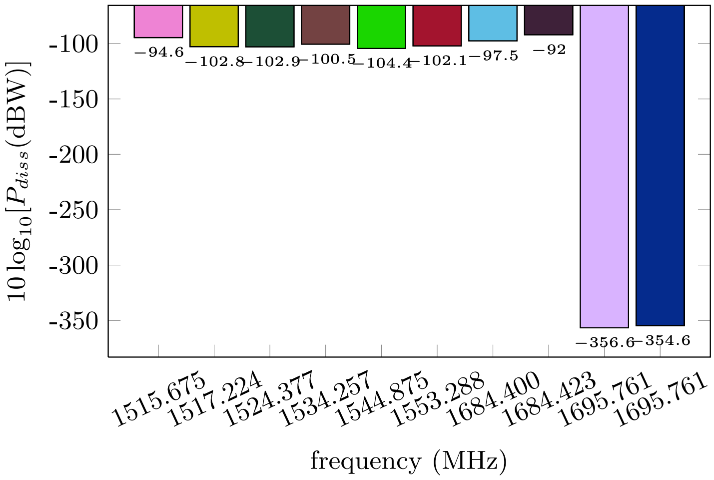

Figure 12: Average Power Dissipated for the modes 7 - 16 in dBW.

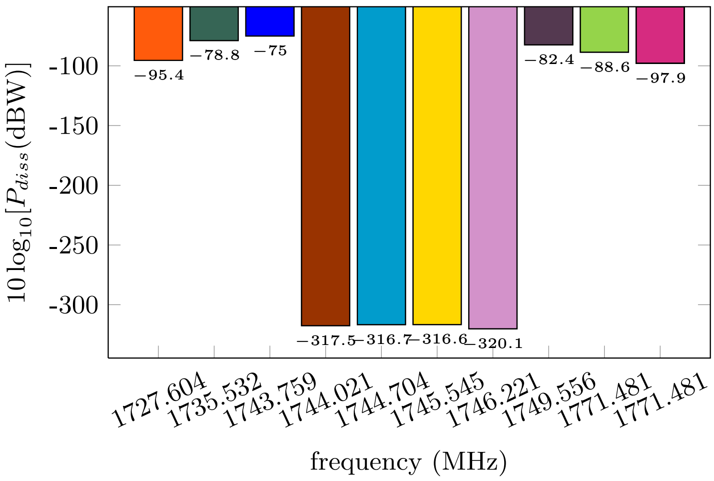

Figure 13: Average Power Dissipated for the modes 17 - 26 in dBW.

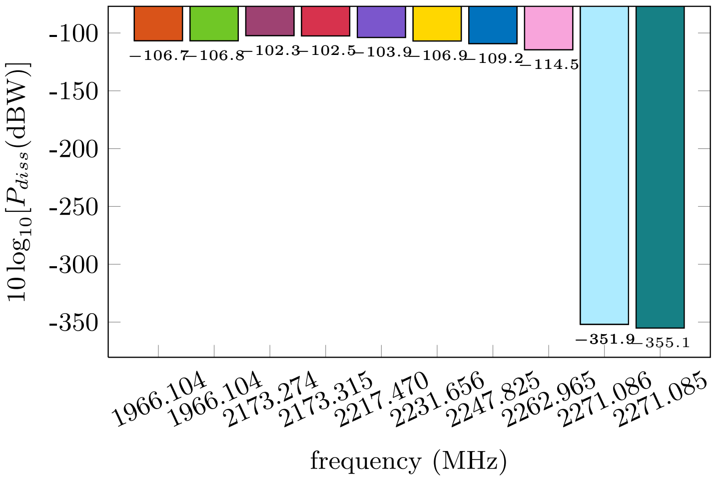

Figure 14: Average Power Dissipated for the modes 27 - 36 in dBW.

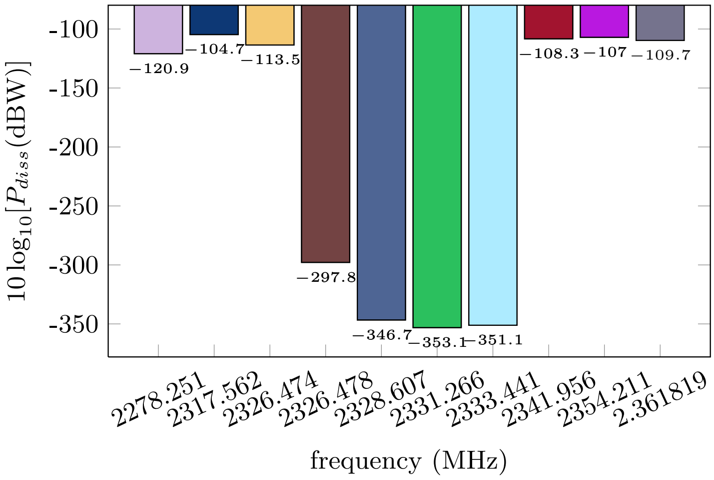

Figure 15: Average Power Dissipated for the modes 37 - 46 in dBW.

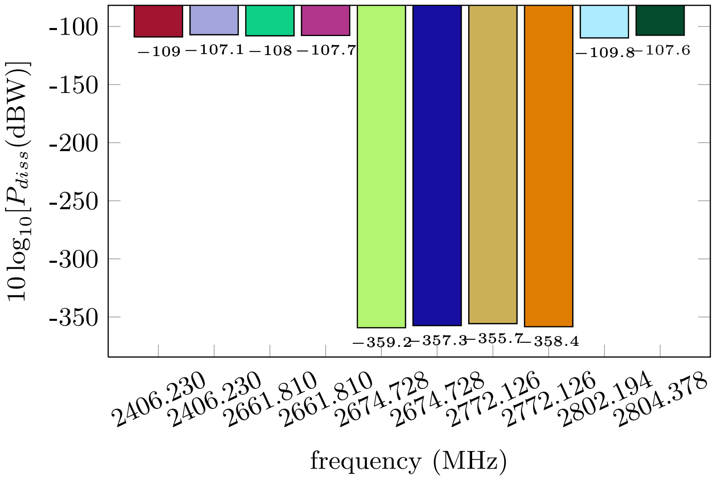

Figure 16: Average Power Dissipated for the modes 47 - 56 in dBW.

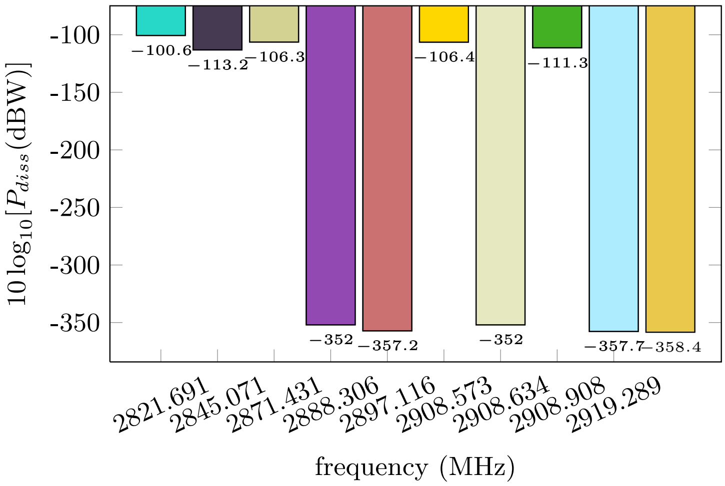

Figure 17: Average Power Dissipated for the modes 57 - 66 in dBW.

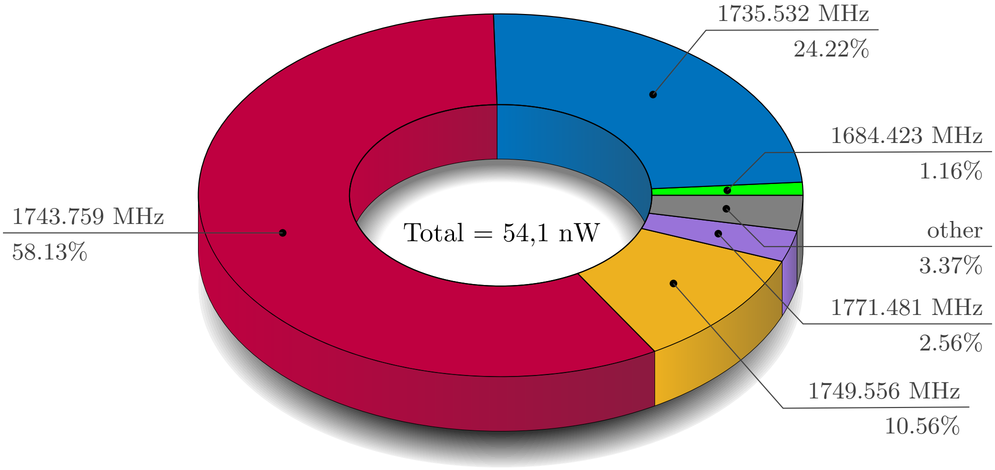

Figure 18: Distribution of the average dissipated powers. 3 modes, 18 (blue), 19 (red) and 24 (yellow), contribute to 93% of the total dissipated power

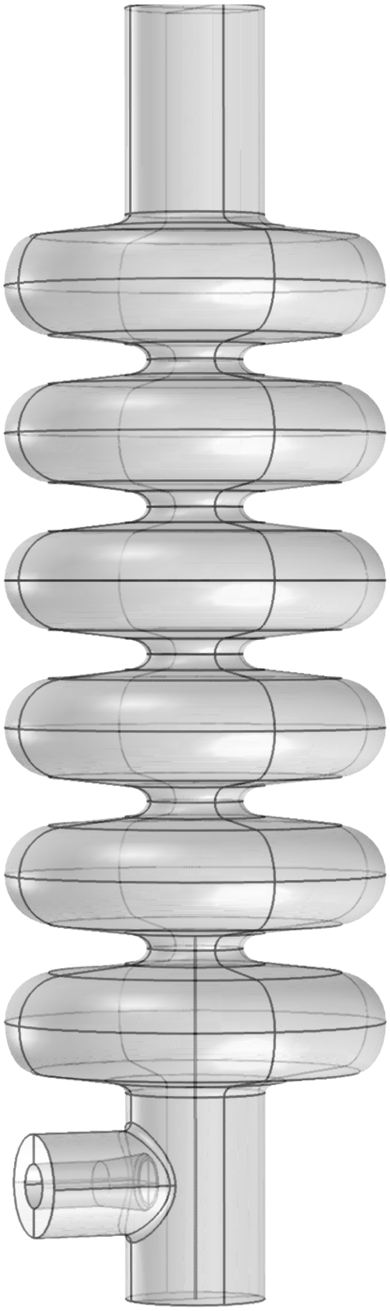

Figure 19: The model of the six-cell elliptical cavity used to make the 3D simulations. The transverse fields have been sampled on the black line extending from the beginning of the beam pipe to the end of the first cell. The perturbation though is negligible as shown in figure 20

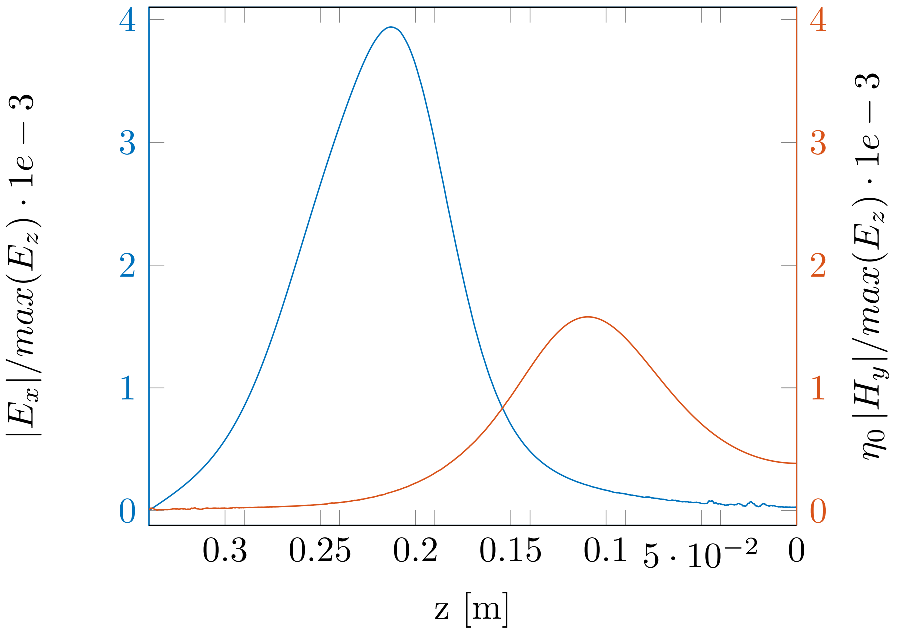

Figure 20: Transverse electric (curve with higher amplitude) and magnetic fields on the axis of the cavity normalized with respect to the maximum of the longitudinal electric field. The transverse fields are $\approx 1e3$ times weaker than the accelerating field.

References

[1] M. Lindroos, in SRF2011 Conference Proceedings (2011).

[2] H. Danared (ESS/AD and ESS/ADU), in IPAC2012 Conference Proceedings (2012).

[3] R. Ainsworth and S. Molloy, Nucl. Instrm. & Methods, 734, 95 (2012).

[4] J. Tückmantel, Phys. Rev. ST Accel. Beams 13 (2010).

[5] M. Schuh, F. Gerigk, J. Tckmantel, and C. P. Welsch, Phys. Rev. ST Accel. Beams 14 (2011).

[6] S. Ho Kim, M. Doleans, D. o Jeon, and R. Sundelin, Nucl. Instrm. & Methods 492, 1 (2002).

[7] H. J. Zheng, J. Gao, C. Pagani, J. F. Chen, *HOM Calculations for Different Cavities and Beam Induced HOM Power Analysis of ESS*, Proc. SRF2015, Whistler, BC, Canada, 2015.

[8] H. Padamsee, J. Knobloch, and T. Hays, RF Super-conductivity for Accelerators, 2nd ed. (Wiley-VCH, 2008) Chap. 15.4.

[9] G. Devanz, N. Bazin, M. Desmons, P. Bosland, P. Hardy, F. Leseigneur, M. Luong, F. Peauger, J. Plouin, D. Roudier, G. Olivier, and G.Costanza, in *SRF2013 Conference Proceedings* (2013).

[10] A. W. Chao, *Phisics of Collective Beam Instabilities in High Energy Accelerators*, (John Wiley & Sons, Inc, 1993)

[11] P. B. Wilson, *Introduction to Wakefields and Wake Potentials*, SLAC-PUB-4547, SLAC/AP-66, January 1989.

[12] K. L. F. Bane, Z. Li, *Obtaining the Wakefield due to Cell-to-Cell misalignment in a Linear Accelerator Structure*, SLAC-AP-128, July 2000.

[13] K. L. F. Bane, P. B. Wilson, T. Weiland, *Wake Fields and Wake Field Acceleration*, SLAC-PUB-3528, December 1984.

[14] F. Gerigk, L. Arnaudon, P. Baudrenghien, M. Baylac, G. Bellodi, Y. Body, J. Borburgh, P. Bourquin, J. Broere, O. Brunner, L. Bruno, C. Carli, F. Caspers, S.M. Cousineau, Y. Cuvet, C. De Almeida Martins, T. Dobers, T. Fowler, R. Garoby, B. Goddard, K. Hanke, M. Hori, M. Jones, K. Kahle, W. Kalbreier, T. Kroyer, D. Kchler, A.M. Lombardi, L.A. Lopez-Hernandez, M. Magistris, M. Martini, S. Maury, E. Page, M. Paoluzzi,

M. Pasini, U. Raich, C. Rossi, J.P. Royer, E. Sargsyan, J. Serrano, R. Scrivens, M. Silari, M. Timmins, W. Venturini-Delsolaro, M. Vretenar, R. Wegner, W. Weterings, and T. Zickler, *Linac4 Technical Design Report, Technical Design Report*, CERN Report No. CERN-AB-2006-084, 2006.

[15] L. Wen, S. Zhang, Y. Li, R. Wang, H. Guo, C. Zhang, H. Jia, T. Jiang, C. Li, Y. He, *Study of Medium Beta Elliptical Cavities for CADS*, Chinese Physics C, Vol. 40, No 2 (2016).

[16] J. C. Slater, *Microwave Electronics*, Van Nostrand, 1950.

[17] W. Geyi, in PIER (2008) pp. 219 253.

[18] S. Aksoy and O. A. Tretyakov, Journal of Electromagnetic Waves and Applications 16:11, 219 (2002).

[19] G. Costanza and A. D. Ioannidis, in PIER (2013) pp. 79 83.

[20] K. Kurokawa, IRE Trans. on Microwave Theory and Tech. MTT-6 (1958).

[21] A. Omar, *Electromagnetic Scattering and Material Characterization* (Artech House, 2011).

[22] J. Helsing and A. Karlsson, IEEE Trans. Microwave Theory & Tech. MTT-63 (2015).

[23] "https://www.comsol.se"

[24] D. Robert and J. louis Lions, *Mathematical Analysis and Numerical Methods for Science and Technology* (Springer, 2000).

[25] K. jochen Engel and R. Nagel, *One-Parameter Semigroups for Linear Evolution Equations* (Springer, 2000).

[26] J.-L. L. Robert Dautray,*Mathematical Analysis and Numerical Methods for Science and Technology. Volume 5, Evolution Problems* (Springer, 2000).

[27] F. Gantmacher, *Lectures in Analytical Mechanics* (MIR Publications, Moscow, 1975).

[28] L. A. Pars, *A Treatise on Analytical Mechanics* (Heinemann, 1965).

[29] J. L. S. Herbert Goldstein, Charles P. Poole, *Classical Mechanics* (Addison Wesley, 2002)

[30] C. A. Balanis, *Advanced Engineering Electromagnetics* (John Wiley & sons, 1989).

[31] ”http://www.eit.lth.se/index.php?uhpuid=dhs.gec&hpuid=1013&L=1”.

Paper V

The Coupled Cavity in the Time Domain

Gabriele Costanza.

Abstract

The problem of finding the transfer function between two couplers attached to a microwave cavity is proposed in the time domain. An example involving an elliptical cavity is presented and solved. This includes the calculation of the evolution of the modes of the cavity and the voltage waves in the waveguides of the copulers.

1 The Coupled Cavity in the Time Domain

The coupled cavity, constituted by the cavity itself, the couplers, waveguides and waveguide terminations, is a complex system, but it can be simplified if separated in several parts. A convenient way to separate such systems, is to consider the cavity and the short sections of the waveguides connected to it as being one unit, called the coupled-cavity, and the external circuits as another unit (see figure 1 for a sketch of the coupled-cavity).

The analysis is carried out starting from Maxwell's equations in the time domain and imposing as an excitation a wave going from the generator towards the cavity. The model is completed considering that the reflected wave going from the cavity back to the generator has to be absorbed by the matched load after a circulator and thus is not reflected back into the cavity. This is embodied in the formulation of the boundary condition at the port surface. The problem is simplified by considering two special cases, where the *open circuit* and the *short circuit* port terminations are used.

1.1 Description of the Problem

Consider a cavity coupled to a generator and a pickup port. Both the generator and the pickup port are connected to the cavity through a waveguide.

The coupled-cavity is defined by the cavity itself plus a small section of the waveguides up to the surface S_g. Its domain is the open and bounded domain Ω which is a subset of $\mathbb{R}^3$. Ω is entirely inside its regular boundary $S = S_c \cup S_g$ which is at least Lipschitz and with external normal $\hat{\boldsymbol{n}}$. S_c denotes the surface of the metal and S_g and S_{pk} are the cross sections of the generator and pickup waveguides respectively. We let Ω' be the complement of Ω.

In this section we propose a derivation of the equations that model the electric and magnetic evolutions of the fields $\boldsymbol{\mathcal{E}}$ and $\boldsymbol{\mathcal{H}}$ in the cavity, for $t \in [0, T]$, that satisfy

$$\begin{cases} \nabla \times \boldsymbol{\mathcal{E}} = -\mu_0 \dfrac{\partial \boldsymbol{\mathcal{H}}}{\partial t} \\ \nabla \times \boldsymbol{\mathcal{H}} = \epsilon_0 \dfrac{\partial \boldsymbol{\mathcal{E}}}{\partial t} \end{cases} \quad \text{in } \Omega, t \in [0, T]. \tag{1}$$

with homogeneous initial conditions,

$$\boldsymbol{\mathcal{E}}(\boldsymbol{r}, t = 0) = 0; \qquad \boldsymbol{\mathcal{H}}(\boldsymbol{r}, t = 0) = 0 \quad \text{in } \Omega. \tag{2}$$

The cavity fields are expanded in terms of cavity orthogonal modes [1]:

$$\boldsymbol{\mathcal{E}} = \sum_{n=0}^{\infty} e_n(t) \boldsymbol{E}_n(\boldsymbol{r}) = \sum_n \boldsymbol{\mathcal{E}}_n, \qquad \boldsymbol{\mathcal{H}} = \sum_{n=0}^{\infty} h_n(t) \boldsymbol{H}_n(\boldsymbol{r}) = \sum_n \boldsymbol{\mathcal{H}}_n. \tag{3}$$

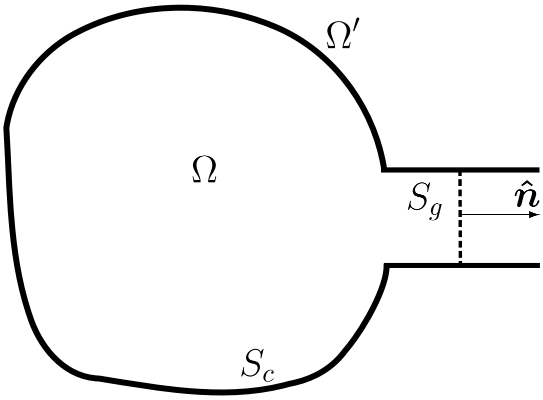

Figure 1: Schematic representation of the coupled-cavity. It features the resonator and a short section of waveguide that couples the generator to the cavity itself.

Moreover the cavity modes satisfy the equations

$$\begin{cases} \nabla \times \boldsymbol{E}_n = -\mathrm{i}\,\omega_n \mu_0\, \boldsymbol{H}_n \\ \nabla \times \boldsymbol{H}_n = \mathrm{i}\,\omega_n \epsilon_0\, \boldsymbol{E}_n \end{cases} \quad \text{in } \Omega \tag{4}$$

with either *perfect electric conductor* (PEC) boundary condition

$$\hat{\boldsymbol{n}} \times \boldsymbol{E}_n = 0, \qquad \text{on } S \tag{5}$$

or PEC boundary condition on S_c and *perfect magnetic conductor* boundary condition on S_g:

$$\hat{\boldsymbol{n}} \times \boldsymbol{H}_n = 0, \qquad \text{on } S_g. \tag{6}$$

Substituting the expansions (3) in the first of (1) and taking the scalar product with $\boldsymbol{H}_m^*(\boldsymbol{r})$ we obtain:

$$\sum_m e_m(t)\,(\nabla \times \boldsymbol{E}_m, \boldsymbol{H}_n^*) = -\mu_0 \sum_n \frac{dh_n}{dt}\,(\boldsymbol{H}_n, \boldsymbol{H}_m^*)\,. \tag{7}$$

By integration by parts we have

$$(\nabla \times \boldsymbol{u}, \boldsymbol{v}) \coloneqq (\boldsymbol{u}, \nabla \times \boldsymbol{v}) + \langle \hat{\boldsymbol{n}} \times \boldsymbol{u}, \boldsymbol{v} \rangle_S, \tag{8}$$

so that we can rewrite the left hand side of (7) as:

$$\begin{aligned}\sum_m e_m(t)\,(\nabla\times\boldsymbol{E}_m,\boldsymbol{H}_n^*) &= \sum_m e_m(t)\,(\boldsymbol{E}_m,\nabla\times\boldsymbol{H}_n^*)_\Omega+\sum_n\langle\hat{\boldsymbol{n}}\times\boldsymbol{\mathcal{E}}_m\,\boldsymbol{H}_n^*\rangle_S\\ &= \sum_n \mathrm{i}\,\omega_n\,\epsilon_0\,e_n(t)+\sum_m\langle\hat{\boldsymbol{n}}\times\boldsymbol{\mathcal{E}}_m,\boldsymbol{H}_n^*\rangle_S.\end{aligned}\tag{9}$$

where $\langle\cdot,\cdot\rangle$ indicates the flux integral. Equation (7) then becomes

$$-\mu_0\frac{dh_n}{dt}=\mathrm{i}\,\omega_n\,\epsilon_0\,e_n+\sum_m\langle\hat{\boldsymbol{n}}\times\boldsymbol{\mathcal{E}}_m,\boldsymbol{H}_n^*\rangle_S.\tag{10}$$

We proceed with the derivation of the second independent equation. Proceeding in a similar way as for the derivation of (10), we take the inner product of the second of (1) with the cavity mode $\boldsymbol{E}_n^*$ and obtain

$$\begin{aligned}\sum_m h_m(t)\,(\nabla\times\boldsymbol{H}_m,\boldsymbol{E}_n^*) &= \sum_m h_m(t)\,(\boldsymbol{H}_m,\nabla\times\boldsymbol{E}_n^*)_\Omega+\sum_m\langle\hat{\boldsymbol{n}}\times\boldsymbol{\mathcal{H}}_m,\boldsymbol{E}_n^*\rangle_S\\ &= -\mathrm{i}\,\omega_n\,\mu_0\,h_n(t)+\sum_m\langle\hat{\boldsymbol{n}}\times\boldsymbol{\mathcal{H}}_m,\boldsymbol{E}_n^*\rangle_S.\end{aligned}\tag{11}$$

With (11), the second of (1) becomes

$$\epsilon_0\frac{de_n}{dt}=-\mathrm{i}\,\omega_n\,\mu_0\,h_n+\sum_m\langle\hat{\boldsymbol{n}}\times\boldsymbol{\mathcal{H}}_m,\boldsymbol{E}_n^*\rangle_S,\tag{12}$$

From (10) and (12), introducing $\eta_0=\sqrt{\mu_0/\epsilon_0}$, we obtain:

$$\frac{de_n(t)}{dt}=-\mathrm{i}\omega_n\eta_0^2h_n(t)+\frac{1}{\epsilon_0}\sum_m\langle\hat{\boldsymbol{n}}\times\boldsymbol{\mathcal{H}}_m,\boldsymbol{E}_n^*\rangle_S\tag{13}$$

$$\frac{dh_n(t)}{dt}=-\mathrm{i}\frac{\omega_n}{\eta_0^2}e_n(t)-\frac{1}{\mu_0}\sum_m\langle\hat{\boldsymbol{n}}\times\boldsymbol{\mathcal{E}}_m,\boldsymbol{H}_n^*\rangle_S\tag{14}$$

which allow to calculate the evolution of the electric and magnetic fields in a cavity coupled to the generator waveguide and the pickup waveguide. The generalization to an arbitrary number of couplers is immediate and amounts to adding the terms corresponding to every aperture in the cavity, to the surface integrals in (10) and (12). We also underline that the boundary conditions are embedded in the surface integrals in equations (13) and (14).

We now turn to the study of the boundary condition by transforming the mentioned surface integrals into quantities that typically characterize the performance of a cavity, such as the quality factors. Thanks to the field equivalence principle [2] we define equivalent electric and magnetic sources $\boldsymbol{\mathcal{J}}_s$ and

$\boldsymbol{\mathcal{M}}_s$ in terms of which we expand the tangential component of the electric and magnetic field on S_g. These surface currents radiate into the coupled-cavity producing the same fields that would be produced by the generator. The fields in Ω' are not of interest at this step of the analysis, and the volume Ω' can be replaced with a perfect electric conductor (short circuit case), or with a perfect magnetic conductor (open circuit case).

Open circuit case. We examine first the case in which we impose the open circuit condition $\hat{\boldsymbol{n}} \times \boldsymbol{H} = 0$ on S_g.

First, if the cavity walls are not a perfect conductor, we have that the power flowing in the walls of the cavity is

$$\sum_m \langle \hat{\boldsymbol{n}} \times \boldsymbol{\mathcal{H}}_m, \boldsymbol{E}_n^* \rangle_{S_c} = \mathrm{i}\frac{2\omega_n U_{e,n}}{Q_{0,n}} h_n(t). \tag{15}$$

where $U_{e,n}$ is the electric energy of mode n stored in the cavity defined as

$$U_{e,n} = \frac{1}{4}\epsilon_0 \int\limits_\Omega |\boldsymbol{E}_n|^2 \, d\Omega \tag{16}$$

and $Q_{0,n}$ is the intrinsic quality factor of mode n. We also define the magnetic energy

$$U_{h,n} = \frac{1}{4}\mu_0 \int\limits_\Omega |\boldsymbol{H}_n|^2 \, d\Omega = U_{e,n}. \tag{17}$$

The eigenfields are normalized so that

$$\int\limits_\Omega |\boldsymbol{E}_n|^2 \, d\Omega = \eta_0^2 \int\limits_\Omega |\boldsymbol{H}_n|^2 \, d\Omega = \frac{4U_{e,n}}{\epsilon_0} = \frac{4U_{h,n}}{\epsilon_0} = 1. \tag{18}$$

Second, we examine the surface integral in (14) which can be rewritten as:

$$\sum_m \langle \hat{\boldsymbol{n}} \times \boldsymbol{\mathcal{E}}_m, \boldsymbol{H}_n^* \rangle_S = \sum_m \langle \boldsymbol{\mathcal{M}}_m, \boldsymbol{H}_n^{*+} \rangle_{S_g} + \sum_m \langle \boldsymbol{\mathcal{M}}_m, \boldsymbol{H}_n^{*-} \rangle_{S_g} \tag{19}$$

The last expression represents the modal energy flowing through the generator port. That energy can be divided in two parts. The first part represents the power leaking from the coupled-cavity towards the generator and the second represents the energy entering the cavity from the generator. The second contribution represents the known term that drives the mode evolution equations. In our case we only consider the interaction of the coupled-cavity modes with the fundamental mode of the waveguide, characterized by the field $\{\boldsymbol{E}_g, \boldsymbol{H}_g\}$. Concerning the first contribution, we can write

$$\sum_m \langle \boldsymbol{\mathcal{M}}_m, \boldsymbol{H}_n^{*+} \rangle_{S_g} = \sum_m e_m(t) \langle \boldsymbol{M}_m, \boldsymbol{H}_n^{*+} \rangle_{S_g} = \mathrm{i}\frac{2\omega_n U_{e,n}}{Q_{ext,n}} e_n(t), \qquad \forall n. \tag{20}$$

Concerning the second contribution we have

$$\sum_m \langle \boldsymbol{\mathcal{M}}_m, \boldsymbol{H}_n^{*-} \rangle_{S_g} = \langle \boldsymbol{\mathcal{M}}_g, \boldsymbol{H}_n^{*-} \rangle_{S_g} = \mathrm{i} \langle \boldsymbol{M}_g, \boldsymbol{H}_n^{*-} \rangle_{S_g} V^{(g)}(t) \qquad \forall n \tag{21}$$

where $\boldsymbol{\mathcal{M}}_g = V^{(g)}(t) \boldsymbol{M}_g$ is the impressed magnetic current. The surface integrals (19) then become:

$$\sum_m \langle \hat{\boldsymbol{n}} \times \boldsymbol{\mathcal{E}}_m, \boldsymbol{H}_n^{*} \rangle_S = \frac{2\omega_n U_{e,n}}{Q_{ext,n}} e_n(t) + \mathrm{i} \langle \boldsymbol{M}_g, \boldsymbol{H}_n^{*-} \rangle_{S_g} \frac{1}{N_g} V^{(cav)}(t), \qquad \forall n, \tag{22}$$

where $Q_{ext,n}$ is the external quality factor of the mode n, which will be defined in the following. In (22) we have used the fact that $V^{(g)} = V^{(cav)} \frac{1}{N_g}$ where $V^{(g)}$ is the equivalent voltage at the waveguide side and $V^{(cav)}$ is the equivalent cavity voltage at the cavity side. With (15), (18) and (22), equations (13) and (14) become

$$\begin{cases} \dfrac{de_n(t)}{dt} = -\mathrm{i}\omega_n \eta_0^2 h_n(t) + \mathrm{i} \dfrac{\omega_n}{2Q_{0,n}} h_n(t) \\ \dfrac{dh_n(t)}{dt} = -\mathrm{i} \dfrac{\omega_n}{\eta_0^2} e_n(t) - \dfrac{\mathrm{i}}{\eta_0^2} \dfrac{\omega_n}{2Q_{ext,n}} e_n(t) - \dfrac{\mathrm{i}}{\mu_0} \langle \boldsymbol{M}_g, \boldsymbol{H}_n^{*-} \rangle_{S_g} \dfrac{1}{N_g} V^{(cav)}(t) \end{cases} \tag{23}$$

or

$$\frac{d}{dt} \begin{pmatrix} e_n(t) \\ h_n(t) \end{pmatrix} = \begin{pmatrix} 0 & \mathrm{i} \dfrac{\omega_n}{2Q_{0,n}} - \mathrm{i}\omega_n \eta_0^2 \\ -\dfrac{\mathrm{i}\omega_n}{\eta_0^2} - \dfrac{\mathrm{i}}{\eta_0^2} \dfrac{\omega_n}{2Q_{ext,n}} & 0 \end{pmatrix} \begin{pmatrix} e_n(t) \\ h_n(t) \end{pmatrix} \tag{24}$$

$$- \begin{pmatrix} 0 \\ \dfrac{\mathrm{i}}{\mu_0} \langle \boldsymbol{M}_g, \boldsymbol{H}_n^{*-} \rangle_{S_g} \dfrac{1}{N_g} V(t)^{(cav)} \end{pmatrix}. \tag{25}$$

In the open circuit case, the external Q is calculated with

$$Q_{ext,n}^{open} = \frac{\omega_n \epsilon_0 \int\limits_{\Omega} |\boldsymbol{E}|^2 \, d\Omega}{\eta_0^{-1} \int\limits_{S_g} |\boldsymbol{E}|^2 \, dS} = \frac{4\omega_n U_{e,n}}{P_{ext,n}}, \tag{26}$$

where U_n is the electromagnetic energy stored in the cavity and $P_{ext,n}$ is the power leaving through the coupler and $\eta_0 = \sqrt{\mu_0/\epsilon_0}$.

Short Circuit case. We impose the condition $\hat{\boldsymbol{n}} \times \boldsymbol{E} = 0$ on S_g. Concerning the surface integral in (12) we have:

$$\langle \hat{\boldsymbol{n}} \times \boldsymbol{\mathcal{H}}_n, \boldsymbol{E}_m^* \rangle_S = \langle \hat{\boldsymbol{n}} \times \boldsymbol{\mathcal{H}}_n, \boldsymbol{E}_m^* \rangle_{S_g} + \langle \hat{\boldsymbol{n}} \times \boldsymbol{\mathcal{H}}_n, \boldsymbol{E}_m^* \rangle_{S_c}. \tag{27}$$

As in the open circuit case, the integral over S_c represents the modal resistive losses. Using the same arguments as in the open circuit case, we can rewrite the surface integral over S_g of (27) as:

$$\langle \hat{\boldsymbol{n}} \times \boldsymbol{\mathcal{H}}_m, \boldsymbol{E}_n^* \rangle_{S_g} = \langle \boldsymbol{\mathcal{J}}_n, \boldsymbol{E}_m^{*+} \rangle_{S_g} + \langle \boldsymbol{\mathcal{J}}_n, \boldsymbol{E}_m^{*-} \rangle_{S_g} \tag{28}$$

where the first integral at the right hand side of (28) represents the power leaving the coupled-cavity, while the second contribution represents the energy entering the cavity coming from the power generator. With $\hat{\boldsymbol{n}} \times \boldsymbol{\mathcal{H}}_n = \boldsymbol{\mathcal{J}}_n$ the first integral of (28) becomes

$$\langle \boldsymbol{\mathcal{J}}_m, \boldsymbol{E}_n^{*+} \rangle_{S_g} = \frac{2\omega_n U_{h,n}}{Q_{ext,n}} h_n(t). \tag{29}$$

while the second integral can be rewritten as

$$\langle \boldsymbol{\mathcal{J}}_m, \boldsymbol{E}_n^{*-} \rangle_{S_g} = \langle \boldsymbol{J}_g, \boldsymbol{E}_m^{*-} \rangle I^{(g)}(t). \tag{30}$$

where we have made the approximation that the power entering the cavity is entirely delivered by the fundamental waveguide mode. This implies that the driving term be rewritten as $\boldsymbol{\mathcal{J}}_m = \boldsymbol{J}_g \, I^{(g)}(t)$. Using (29), (30) we rewrite (28) as:

$$\sum_m \langle \hat{\boldsymbol{n}} \times \boldsymbol{\mathcal{H}}_m, \boldsymbol{E}_n^* \rangle_{S_g} = \frac{2\omega_n U_{h,n}}{Q_{ext}} h_n(t) + \langle \boldsymbol{J}_g, \boldsymbol{E}_n^{*-} \rangle N_g I^{(cav)}(t) + \frac{2\omega_n U_{e,n}}{Q_0} e_n(t), \tag{31}$$

where we have used the fact that $I^{(g)} = N_g I^{(cav)}$. We can rewrite (13) and (14) as

$$\frac{d}{dt} \begin{pmatrix} e_n(t) \\ h_n(t) \end{pmatrix} = \tag{32}$$

$$\begin{pmatrix} \dfrac{\omega_n}{2Q_{0,n}} & -\mathrm{i}\omega_n \eta_0^2 + \dfrac{\omega_n}{2Q_{ext,n}} \\ -\dfrac{\mathrm{i}\omega_n}{\eta_0^2} & 0 \end{pmatrix} \begin{pmatrix} e_n(t) \\ h_n(t) \end{pmatrix} + \begin{pmatrix} \langle \boldsymbol{J}_g, \boldsymbol{E}_n^{*-} \rangle N_g I^{(cav)}(t) \\ 0 \end{pmatrix}. \tag{33}$$

In the short circuit case, the external Q is calculated with

$$Q_{ext,n}^{short} = \frac{\omega_n \epsilon_0 \int\limits_{\Omega} |\boldsymbol{H}|^2 \, d\Omega}{\eta_0 \int\limits_{S_g} |\boldsymbol{H}|^2 \, dS} = \frac{4\omega_n U_{h,n}}{P_{ext,n}}. \tag{34}$$

Transformer Ratio. The transformer ratio N_g can be calculated as follows. The power flowing in the waveguide, is equal to the power that leaves the cavity, moreover, the oscillations in the cavity are N_g times stronger than the voltage wave in the waveguides, that is

$$e_n(t) = N_g \, V^{(g)}(t), \tag{35}$$

where N_g is the transformer ratio. In a similar way we put

$$h_n(t) = \frac{1}{N_g} I^{(g)}(t). \tag{36}$$

The average forward power in the waveguide and the average power leaving the cavity are

$$P_n = \frac{|V_n|^2}{2Z_c} = \frac{|e_n|^2}{2 \, N_g^2 \, Z_c}, \tag{37}$$

$$P_{ext,n} = \frac{\epsilon_0 \omega_n}{Q_{ext,n}}. \tag{38}$$

where Z_c is the characteristic impedance of the waveguide and we have used the normalization (18). Equating the last two equations we have

$$N_g^2 = \frac{|e_n|^2 Q_{ext,n}}{2\omega_n Z_c} = \frac{R}{Q} \frac{Q_{ext,n}}{Z_c} = \frac{R}{Z_c} \frac{1}{\beta}, \tag{39}$$

where we have introduced the coupling factor β^1, which is in general defined as

$$\beta = \frac{Q_0}{Q_{ext}} = \frac{R}{Z_c} \frac{1}{N^2} = \frac{R}{Z_t}, \tag{40}$$

with $Z_t = N_g^2 Z_c$ being the impedance of the external circuit connected to the cavity, transformed to the cavity side.

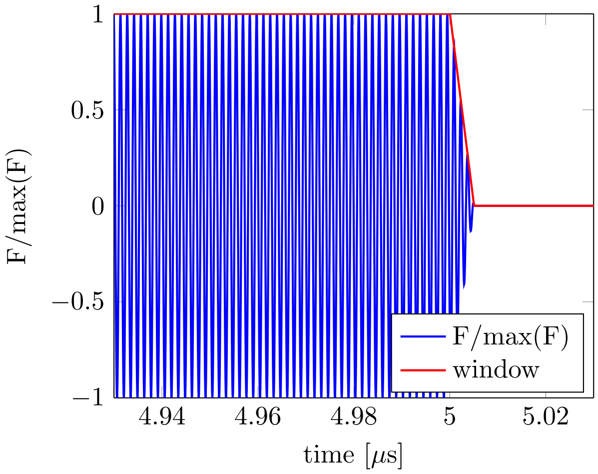

Figure 2: The input signal chosen for the simulations is a sinusoid oscillating at the π mode frequency (blue) modulated by a square window (red)

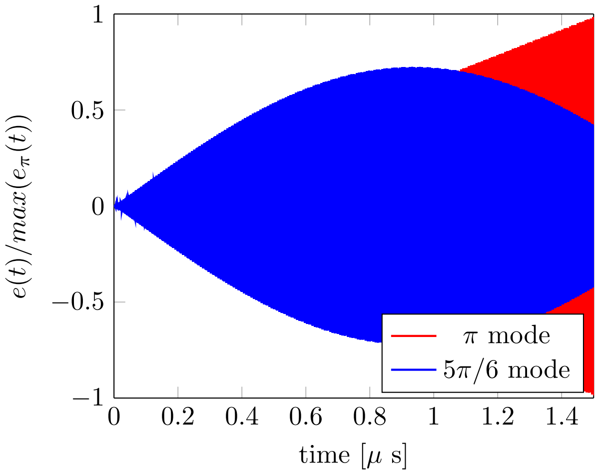

Figure 3: Evolution of the electric field amplitude of the accelerating mode (red) and of the $5\pi/6$ mode (blue). The accelerating mode keeps growing while the $5\pi/6$ mode reaches a maximum before decaying.

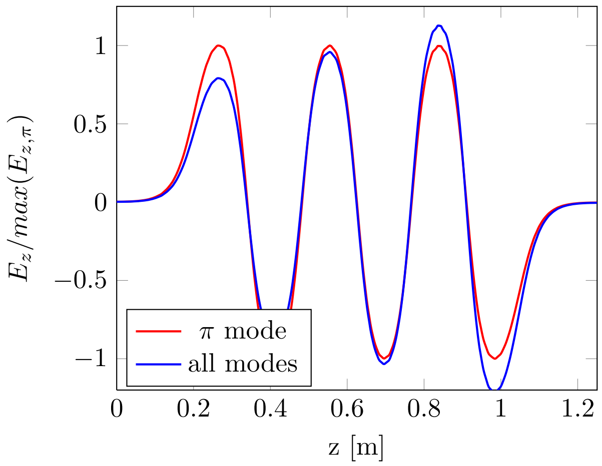

Figure 4: Comparison between the accelerating (π) mode (red) and all the modes excited in the cavity (blue) after 5 μs from the beginning of the input signal. The π mode is starting to emerge above the other modes but it's still significantly corrupted.

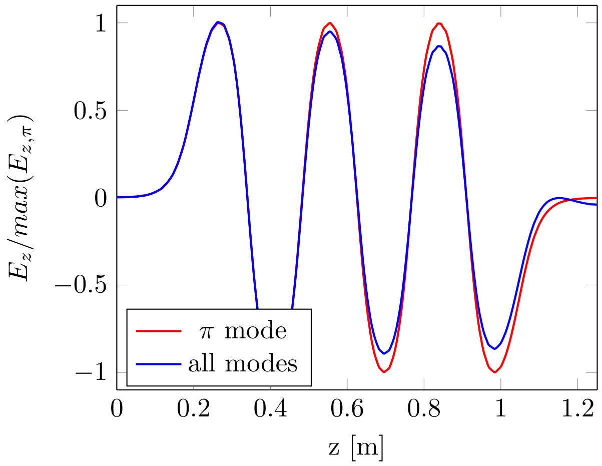

Figure 5: After 8 μ s the accelerating mode is much stronger than all the other modes and the mode corruption is almost absent.

2 Results

2.1 Open Circuit Model

In this section we use the model (25) to calculate the evolution of the modes in a six-cell superconducting elliptical cavity. First the eigenmodes of the cavity are calculated performing an eigenvalue simulation with the *perfect magnetic conductor* (PMC) boundary condition applied to the port surface (in light blue in fig. 6) and a *perfect electric conductor* (PEC) applied to the rest of the surface of the cavity. The Joule losses are considered to be a small perturbation so that the fields obtained using a PEC cavity surface are still valid. A surface resistance (R_s) of 40 nΩ is used to calculate the intrinsic quality factor using the formula

$$Q_{0,n} = \frac{G_n}{R_s}, \tag{41}$$

where G_n is the geometric factor of the mode n defined as

$$G_n = \frac{\omega_n \mu_0 \int\limits_{\Omega} |\boldsymbol{H}_n|^2 \, d\Omega}{\int\limits_{S} |\boldsymbol{H}_n|^2 \, dS} = \frac{2\omega_n U_n}{\int\limits_{S} |\boldsymbol{H}_n|^2 \, dS}. \tag{42}$$

These boundary conditions constitute an approximation and some of the modes thus calculated are “fictitious” in the sense that they exist only thanks to the approximate boundary condition.

The modes with very low external quality factor, that is, the modes with $Q_{ext} < 1e3$, are modes whose energy is confined in the waveguide coupler itself. Those modes are strongly dependent on the boundary conditions and disappear when the boundary condition at the waveguide port is changed. To distinguish waveguide modes from the cavity modes it is possible to perform a simulation of the cavity with the *port* boundary condition.

The input signal chosen to excite the cavity, is a sine oscillating at the frequency of the accelerating mode, modulated by a square window:

$$V^{(cav)}(t) = \sin(w_g t)\,\mathrm{rect}_{\mathrm{T}}(t), \tag{43}$$

where w_g is the angular frequency of the accelerating mode and $\mathrm{rect}_{\mathrm{T}}(t)$ is a square pulse of width $\mathrm{T} = 5\ \mu$s that starts at zero. To make the input signal more realistic the rectangular window is ramped up and down, the ramp being 5 ns long. Figure 2 represents the signal at the end of the rectangular window.

Once the waveguide modes have been excluded, the evolution of the $e_n(t)$ and $h_n(t)$ is calculated with (25) and the time domain electric and magnetic

---

[1] not to be confused with the normalized velocity $\beta = v/c$, where c is the speed of light.

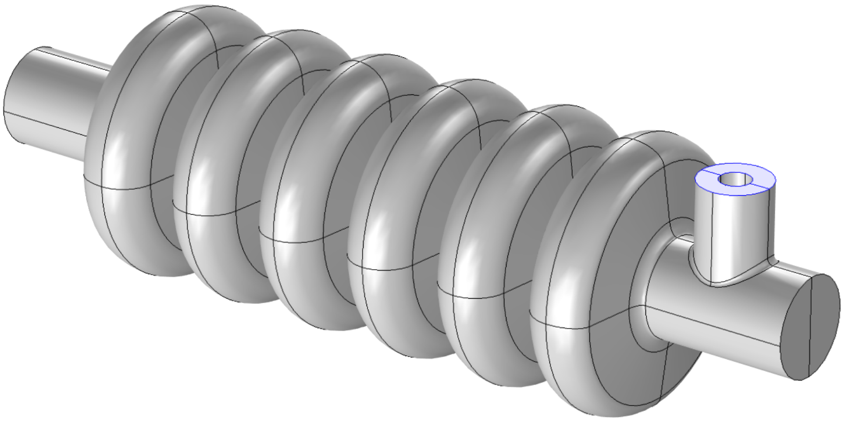

Figure 6: six-cell elliptical cavity used for the simulations.

fields (3) can be calculated. Figure 3 represents the evolution of the amplitude of the accelerating mode and of the $5\pi/6$ mode. The $5\pi/6$ mode reaches a maximum before decaying, this is because the input signal is at the frequency of the accelerating π mode. Figure 4 shows the comparison between the normalized longitudinal electric field of the π mode only and when all the modes are present. After $\approx 10\mu s$ the accelerating mode is much stronger than the other modes and the mode corruption disappears, see fig. 5.

3 Conclusions

A model for the cavity coupled to a coupler has been presented. The model allows to calculate the time-domain evolution of the electric and magnetic field in the cavity. The model is easily extended to accomodate any number of ports and it is useful in the development of the control loop of the cavity.

References

[1] A. Omar, "Electromagnetic Scattering and Material Characterization". Number 5, 1966.

[2] C. A. Balanis, "Advanced Engineering Electromagnetics".